THE SEABED AS AN ACOUSTIC MIRROR FOR SUSPENDED SEDIMENT

CRAIG A. HAMM

National Library of Canada
Acquisitions and Bibliographic Services Branch
395 Wellington Street
Ottawa, Ontario
K1A 0N4

Bibliothèque nationale du Canada
Direction des acquisitions et des services bibliographiques
395, rue Wellington
Ottawa (Ontario)
K1A 0N4

Your file Votre référence

Our file Notre référence

NOTICE

The quality of this microform is heavily dependent upon the quality of the original thesis submitted for microfilming. Every effort has been made to ensure the highest quality of reproduction possible.

If pages are missing, contact the university which granted the degree.

Some pages may have indistinct print especially if the original pages were typed with a poor typewriter ribbon or if the university sent us an inferior photocopy.

AVIS

La qualité de cette microforme dépend grandement de la qualité de la thèse soumise au microfilmage. Nous avons tout fait pour assurer une qualité supérieure de reproduction.

S'il manque des pages, veuillez communiquer avec l'université qui a conféré le grade.

La qualité d'impression de certaines pages peut laisser à désirer, surtout si les pages originales ont été dactylographiées à l'aide d'un ruban usé ou si l'université nous a fait parvenir une photocopie de qualité inférieure.

Canada

The Seabed as an Acoustic Mirror for Suspended Sediment

©Craig A. Hamm, B.Sc. (Hon.)

A thesis submitted to the School of Graduate Studies in partial fulfillment of the requirements for the degree of Master of Science

Department of Physics

Memorial University of Newfoundland

May 1993

St. John's Newfoundland Canada

ISBN 0-315-96042-6

ABSTRACT

Acoustic backscatter signals from suspended sediment, obtained at Queensland Beach N.S. in 1987, and Stanhope Lane Beach P.E.I. in 1989, are *mirrored* below the main bottom echo. The aim of this study is to test the hypothesis that the mirrored backscatter signals are the result of the bottom reflected wave scattering from sediment suspended above the seabed, and subsequently re-reflecting from the bottom back to the transceiver. This hypothesis is tested by devising an inversion algorithm based on the re-reflection idea, to determine suspended sediment concentration and comparing to results from multifrequency and optical backscatter results. A theoretical analysis of the problem and the outcome of subsequent data inversion are presented. Unlike currently used methods, factors such as beam directivity, system constant, and the sediment backscattering form factor are absent from the equation used to determine suspended sediment concentrations. It is concluded that the bottom reflection plays a key role in the formation of the acoustic mirror image.

Contents

List of Tables

List of Figures

List of Symbols

A	system sensitivity constant
a	scattering particle radius
$\overline{a}$	mean particle radius
a_g	geometric mean radius of size distribution
a_o	radius of transducer face
b	bottom bin number
c	sound speed in fluid
c_s	compressional sound speed in sediment
D	transducer directivity
D_{zy}	mean relative difference
F^2	Equation 2.11
$\|f_\infty(a,\pi)\|$	far-field backscattering form factor
G	acoustic source term
g	roughness parameter

H	height of transducer above seabed
I_o	source intensity at range r_*
h_r	mean ripple height
K_α	$= (\gamma_k^2 + \gamma_\rho^2/3)/6$
k_c	compressional wave number in ambient fluid
$L(r_0)$	Equation 2.42
M	mass density of scatterers
N	number density of scatterers
$n(a)$	particle size spectral distribution
p_i	incident pressure at scatterer
p_s	backscattered pressure
p_s'	scattered pressure from mirror signal
$\tilde{p}_s$	TVG corrected backscattered pressure
$\tilde{p}_s'$	TVG corrected scattered pressure from mirror signal
p_*	on-axis pressure amplitude at r_*
Q	number of averaged sets
R	reflection coefficient
R_a	Rayleigh parameter
R_{zy}	linear regression coefficient
r	range from center of transducer

r_0	$= (r_1 + r_2)$
r_1	range to bottom from transducer
r_2	range to particle from bottom
r_*	reference distance along acoustic axis
r_c	far-field critical range
S	system calibration factor
s	Equation 2.30
T	rough surface correlation length
t_1	arrival time of backscatter echo
t_2	arrival time of mirror signal echo
t_{bottom}	arrival time of bottom echo
V_N	raw voltage from backscatter signal
V'_N	raw voltage from mirror signal
v_N	background corrected voltage from backscatter signal
v'_N	background corrected voltage from mirror signal
$v_{B,N}$	background voltage from backscatter signal
$v'_{B,N}$	background voltage from mirror signal
v_T	threshold voltage on v_N
$V(r)$	detected volume at distance r from transducer
W	half-beamwidth at range H

x	$= k_c a$, non-dimensional radius of scatterer
z	height above bottom
z_0	some fixed height above bottom
z_N	height to center of Nth range bin above bottom
α	combined attenuation due to water and scatterers
α_o	attenuation due to ambient fluid
α_s	attenuation due to scatterers
β	angle from acoustic axis
β_o	3-dB beamwidth for transducer beam pattern
δ	acoustic e-folding distance in sediment
Δ	one-quarter of pulse length ($c\tau/4$)
Δh	difference in surface heights
Δz	thickness of range bin
ϵ	particle volume concentration
ε_N	standard deviation of Γ_N
Γ_N	Equation 3.10
$\Delta\Gamma_N$	Equation 3.13
γ_k, γ_ρ	compressibility and density contrasts
κ	Equation 2.10
Λ	Equation 2.29

λ	wavelength of sound in fluid
λ_r	mean ripple wavelength
ϕ	$\log_2$(particle diameter in mm)
φ	phase difference between two rays upon reflection
ρ_o	density of ambient fluid
ρ_o'	density of scatterers
ρ_s	mean bulk density of sediment
σ	rms surface height
σ_g	width of log-normal size distribution for sand size
Σ_s	single particle total scattering cross section
τ	acoustic pulse duration
θ_1	angle from normal of incident ray upon a rough surface
θ_2	angle from normal of scattered ray from a rough surface
ζ	$= c\tau[\ \alpha_o + \alpha_s\ ]$
$\langle \cdots \rangle$	time average
overbars	spatial averages applied to bin boundaries
OBS	**O**ptical **B**ackscatter
TVG	**T**i : **V**ariable **G**ain

ACKNOWLEDGEMENTS

Many thanks are due my supervisor Dr. Alex Hay for continuing guidance and sharing his expertise with me on an interesting, and often challenging, topic. Science involves an exchange of ideas, and some of the other people I have had the pleasure to do this with include: Dr. Len Zedel, Douglas Wilson, Cheng He, Halmar Halide, Anna Crawford, and those who I may have forgotten, for which I apologise. Computer support was expertly provided by gurus Rod Campbell and Alan Goulding, with further support by Todd Wareham and Paul Fardy. Roger Guest drafted some of the figures. I also wish to express my sincerest thanks to the many wonderful people of Newfoundland I have met since arriving who have made my stay here feel so much like home. I wish to acknowledge Dr. John Stockhausen[1] without whom I may have never entered the subject of underwater acoustics. Financial support was provided by Dr. Hay's NSERC Operating Grant and the Ocean Production Enhancement Network, and the Memorial University Physics Department in the form of Teaching Assistantships.

Finally, for their continual encouragement and support this thesis is dedicated to my parents.

[1] Deceased, Nov. 1990

Chapter 1

Introduction

1.1 Historical Background

Over the last 10 to 15 years the use of pulsed acoustic systems has begun to play a key role in providing measurements in the field of sediment transport. Early contributions were made by Urick [1948] on sound absorption in suspensions of clay-sized particles, and by Flammer [1962] in suspensions of sand. The recent field measurements have been carried out in several different environments, for the most part at MHz frequencies. Experiments to detect sediment suspension in the deep ocean have been carried out by Libicki *et al.* [1989], and Lynch *et al.* [1991] as a part of HEBBLE (High Energy Benthic Boundary Layer Experiment). Measurements on the continental shelf and slope include those by Orr and Hess [1978], Vincent *et al.* [1982], Orr and Grant [1982]. Hay [1983] has measured acoustic backscatter from mine-tailing

discharge in a fjord environment. Many efforts have been made in the nearshore zone [Young *et al.*, 1982; Hanes *et al.*, 1988; Vincent and Green, 1990; Thorne *et al.*, 1991; Vincent *et al.*, 1991]. Recently Hay and Sheng [1992] employed a multifrequency backscatter system to overcome the size/frequency ambiguity, encountered with single frequency methods, which enabled simultaneous determination of particle size and concentration profiles in an active nearshore environment.

The use of acoustics in this application is motivated by the non-intrusive nature of the measurement and the lack of interaction with the flow field near the bed. Moreover, the soundspeed in water (of order 1500 m/s) provides excellent temporal resolution and allows range-gated measurements for profiling of suspended sediment at centimetre scales. The problem, however, is inverting the backscattered signals to determine suspended sediment concentration.

1.2 Thesis Objective

Illustrated in Figure 1.1 is a representative false colour plot of acoustic data acquired during the October 1987 deployment of RASTRAN (Remote Acoustic Sediment TRANSport) System 1 at Queensland Beach, Nova Scotia. The vertical axis on the acoustic data represents range in metres from a downward-looking acoustic sounder, and the horizontal axis is time, in minutes. Colour variations in these plots represent variations in received signal. The colour palette at the base of Figure 1.1

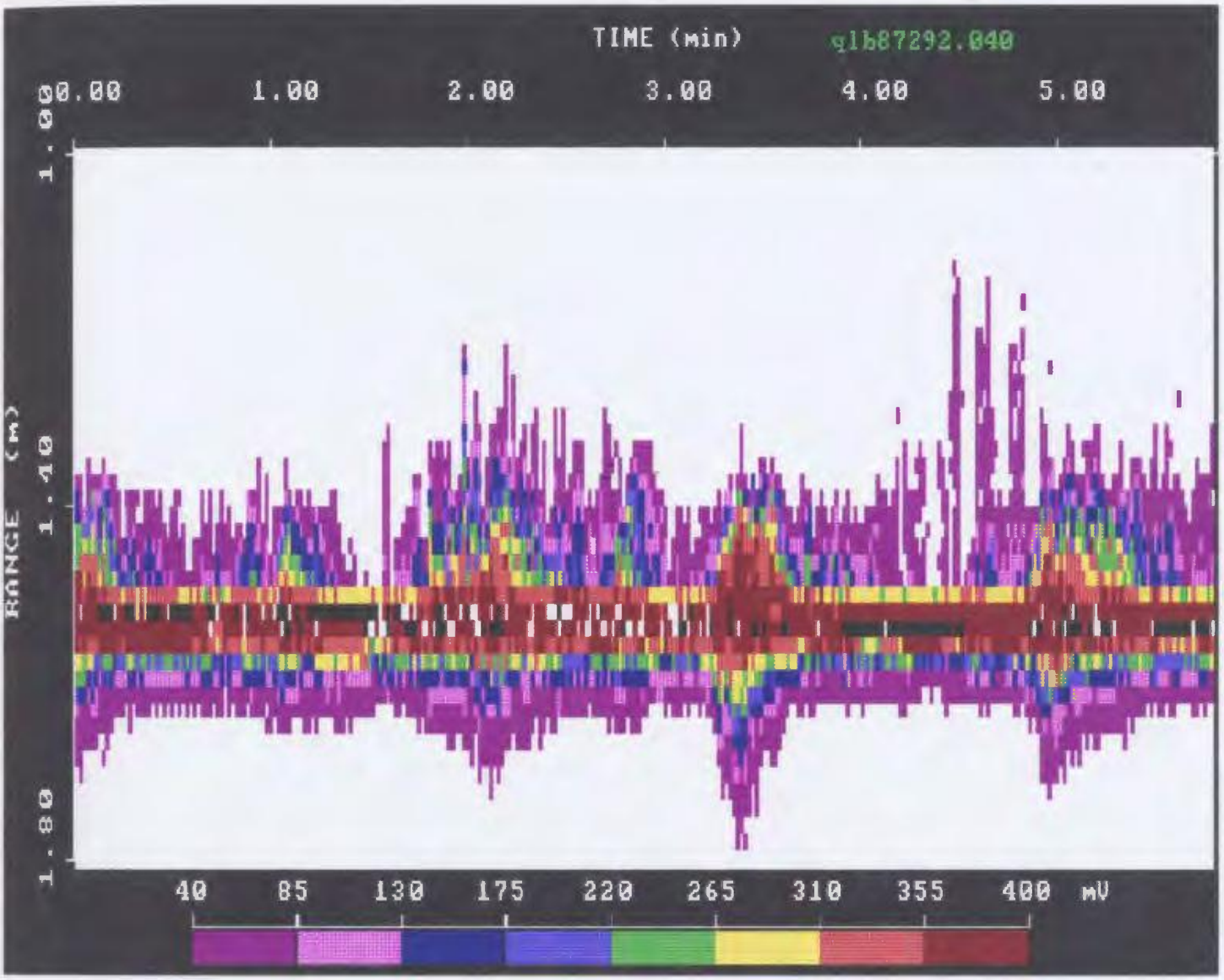

Figure 1.1: False colour plot of acoustic data obtained during the October 1987 RASTRAN deployment at Queensland Beach, Nova Scotia, illustrating the presence of mirrored acoustic backscatter data. Significant suspension events and acoustic mirroring occur near 2, 3.3, and 5 minutes into the run.

maps the recorded output signals of the acoustic sounder to ranges in millivolts. The strongest signal is the main echo from the seabed at approximately 1.55 m range. Above the bottom echo are backscatter signals due to particles in suspension. Significant suspension events occur near 2.0, 3.3, and 5.0 minutes. At ranges beyond the bottom echo are signals which mirror the backscatter signals during these events. One might argue that the mirror images are an artifact of backscatter from suspended sediments detected by the transducer sidelobes. This seems quite unlikely. The strongest sidelobe signals would presumably be from the bottom reflection. If important, they would result in a much lengthened bottom return which would then completely mask the mirror signals in the Figure. Some other explanation is required.

The objective of this thesis is to understand the origin and nature of these acoustic mirror images. The mirror images are hypothesised to be the result of multiple interaction of the incident acoustic wave with the seabed and the suspended sediment. Specifically, it is supposed that the bottom reflected wave is backscattered from suspended sediment near the bottom, and this backscattered wave is subsequently re-reflected from the bottom to the transceiver. To check the validity of this hypothesis an inversion algorithm based on this idea is devised to convert raw acoustic data into suspended sediment concentration, and these results are compared to estimates obtained using multifrequency backscatter and optical backscatter methods.

1.3 Thesis Outline

The thesis is organised as follows: Chapter 2 presents the theory required for scattering of acoustic waves from particles in suspension, acoustic reflection from an irregular surface, and the model used for determining the attenuation due to scattering. Chapter 3 describes the field site, the data acquisition system, and the scheme for inverting acoustic data to sediment concentration based on the hypothesis of section 1.2. Chapter 4 describes data analysis procedures, and provides the basis for an error estimation of the final concentration results. Results from the inversion scheme on two data runs collected during autumn storms at Stanhope Lane Beach, Prince Edward Island, are provided in Chapter 5. Chapter 6 supplements the discussion in Chapter 2 on the bottom reflection coefficient. Conclusions are in Chapter 7.

Chapter 2

Theory

In this chapter an expression is obtained for the scattered re-reflected bottom wave, which is later used to obtain estimates of the suspended sediment concentration within 5 cm above the seabed. The two major components of the theory involve acoustic scattering from particles suspended in water, and acoustic reflection from the seabed.

Section 2.1 briefly presents the acoustic pressure scattered by a single particle and from an ensemble of particles in suspension. Discussion of the monostatic geometry used to interpret the post-bottom echo, or *mirror signal*, follows in Section 2.2. Section 2.3 presents the nature of acoustic reflection from a sandy seabed, and whether it can be treated as specular or diffuse in the megahertz frequency range. Derivation of the mirror signal pressure, follows in Section 2.4. Section 2.5 presents the derivation of the equation which forms the basis of this thesis. The discussion concludes with a

brief summary of the estimation of the attenuation coefficient due to scattering.

2.1 Scattering from an Ensemble of Particles

Illustrated in Figure 2.1 is the geometry for a pulsed monostatic acoustic system, which is to be used in the analysis. Monostatic simply means that the same transducer is used to transmit and receive acoustic energy. The analysis is conducted for ranges r greater than the critical range, r_c, which defines the beginning of the farfield region of the transducer, given by $r_c = \pi a_0^2/\lambda$ [Clay and Medwin, 1977, p155] where a_0 is the radius of the transducer and λ is the wavelength. The transmitted incident wave may then be considered spherical and is expressed as,

$$p_i = AD(\beta)\frac{p_* r_*}{r}e^{-\alpha_0 r} \tag{2.1}$$

In Equation 2.1 the harmonic space and time dependence $e^{i(k_c r - \omega t)}$ is understood. A is a system sensitivity constant, $D(\beta)$ is the transducer's directivity (a measure of its ability to transmit and receive acoustic energy as a function of the angle β from the acoustic axis), p_* is the pressure at reference distance r_* (both are constants), α_0 is the attenuation coefficient due to viscous absorption by pure water and due to chemical relaxation, assumed to be uniform along all paths, and r is the distance from the transducer's centre. The α_0 is calculated using the expressions given by Fisher and Simmons [1977].

For an ideal circular piston transducer of radius a_0, the farfield directivity $D(\beta)$

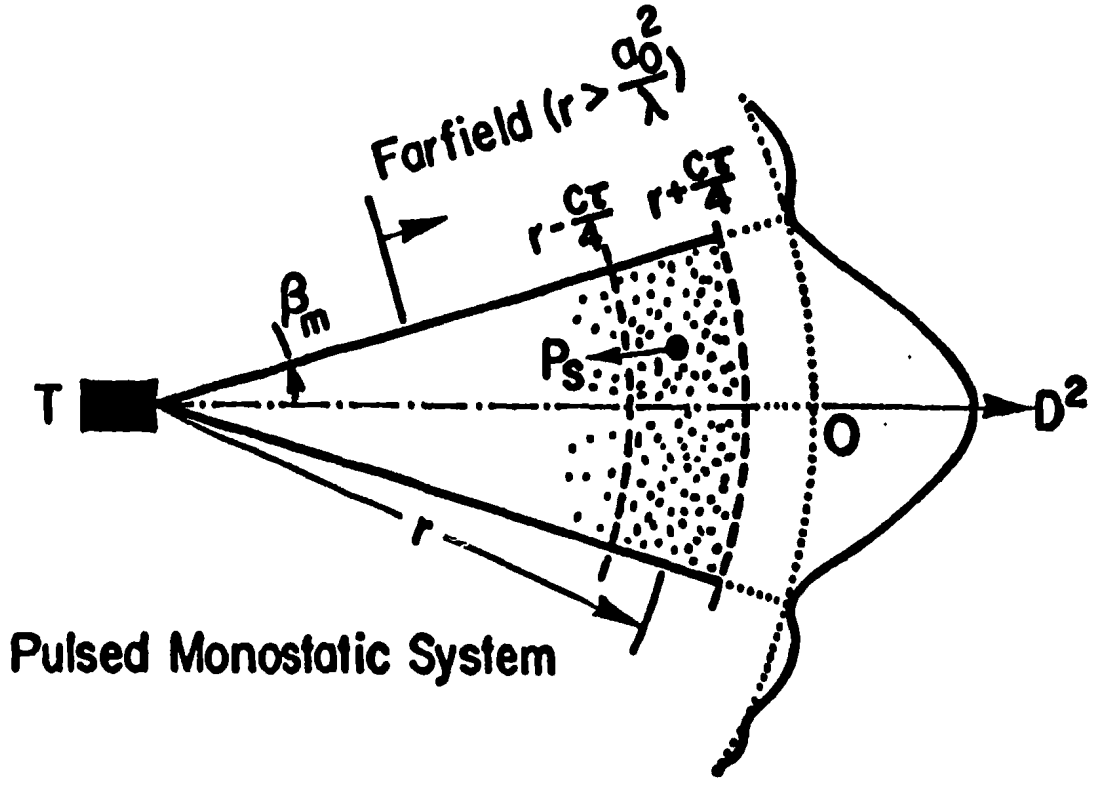

Figure 2.1: Backscattering geometry for a monostatic system (From Hay and Sheng, 1992).

is [Clay and Medwin, 1977, p144],

$$D(\beta) = 2\frac{J_1(k_c a_0 \sin\beta)}{(k_c a_0 \sin\beta)} \tag{2.2}$$

where J_1 is the cylindrical Bessel function of order 1, and $k_c = 2\pi/\lambda$ is the compression wavenumber of the propagation medium.

Consider now the backscattered pressure, p_s, received from a spherical scatterer at distance r' from the transducer and angle β' from the acoustic axis. This pressure is given by,

$$p_s(r') = p_i D(\beta') \left[\frac{a f_\infty(a,\pi)}{2r'}\right] e^{-\alpha_0 r'} \tag{2.3}$$

where a is the radius of the particle, and $f_\infty(a,\pi)$ is the backscattering form factor of that particle [Neubauer *et al.*, 1974]. For a monostatic geometry $r = r'$ and $\beta = \beta'$, thus, substituting p_i into Equation 2.3 the backscattered pressure becomes,

$$p_s(r) = AD^2(\beta)\frac{p_* r_*}{r^2}\left[\frac{a f_\infty(a,\pi)}{2}\right] e^{-2\alpha_0 r}. \tag{2.4}$$

The scattering of acoustic waves by an ensemble of scatterers is discussed in Morse and Ingard [1968, Sect. 8.2]. Backscattering measurements using ultrasonic pulsed acoustic systems in volumes containing randomly distributed scatterers have been made by Sigelmann and Reid [1973], and Shung *et al.* [1976]. For an ensemble of suspended particles insonified by a transmitted pulse, the ensemble mean-square scattered pressure in the absence of multiple scattering can be written as

$$\hat{p}_s^2(r) = \int\int_V \int \left[\int_0^\infty N p_{sj} p_{sj}^* n(a)\, da\right] dV \tag{2.5}$$

where N is the particle number density, $n(a)$ is the size spectral density, V the detected volume, p_{sj} is the pressure scattered by the j^{th} particle, and the asterisk denotes the complex conjugate. The particle number density is related to the mass concentration, M, via the relation,

$$M = N\rho_0' \frac{4}{3}\pi \int_0^\infty a^3 n(a) da \tag{2.6}$$

where ρ_0' is the particle's density. In spherical coordinates,

$$dV = r'^2 \sin\beta \; dr' d\beta d\theta. \tag{2.7}$$

For a transmitted pulse of duration τ, the detected volume at range r is a spherical shell segment of thickness $c\tau/2$ and angular extent $2\beta_0$ and is given by,

$$V(r) = 2\pi \int_{r-\frac{c\tau}{4}}^{r+\frac{c\tau}{4}} \int_0^{\beta_0} r'^2 \sin\beta d\beta dr' \tag{2.8}$$

where $r \pm \frac{c\tau}{4}$ are the far and near boundaries of the pulse as illustrated in Figure 2.1. The angle β_0 is chosen to be the angle at which the contribution to the received scattered pressure becomes negligible. Typically, β_0 is the angle at which the directivity falls 3 dB below the peak value of the main lobe. For the RASTRAN system β_0 is nominally 2° [Hay, 1991].

Substituting Equations 2.4, 2.6, and 2.7 into 2.5, $\hat{p}_s^2$ becomes,

$$\hat{p}_s^2(r) = \frac{3}{8}\epsilon A^2 p_*^2 r_*^2 \kappa F^2 \left\{ \int_{r-\frac{c\tau}{4}}^{r+\frac{c\tau}{4}} \frac{\exp\left\{-4\int_0^{r'} \alpha \, dr''\right\}}{r'^2} dr' \right\} \tag{2.9}$$

where α is the total linear attenuation coefficient,

$$\kappa = \int_0^{\beta_0} D^4(\beta') \sin\beta' d\beta' \tag{2.10}$$

$$F^2 = \left\{ \frac{\int_0^\infty a^2 \mid f_\infty(\pi, a) \mid^2 n(a) da}{\int_0^\infty a^3 n(a) da} \right\}, \tag{2.11}$$

and

$$\epsilon = \frac{M}{\rho_0'} \tag{2.12}$$

is the volume concentration. Performing the necessary integration over r' in Equation 2.9,

$$\hat{p}_s^2(r) = \frac{3}{8} \epsilon \kappa A^2 p_*^2 r_*^2 F^2 \frac{c\tau}{2} \left(\frac{\sinh \zeta}{\zeta} \right) \frac{e^{-4\alpha_0 r - 4\int_0^r \alpha_s \, dr'}}{r^2} \tag{2.13}$$

where

$$\zeta = c\tau(\alpha_0 + \alpha_s). \tag{2.14}$$

The total attenuation coefficient has been split into two components: α_0 is as described earlier; α_s is the attenuation coefficient due to scattering from suspended particles along the acoustic path and depends on the acoustic frequency and the size and concentration of the suspended sediment. More is said about α_s later. The term

$$\left(\frac{\sinh \zeta}{\zeta} \right) \tag{2.15}$$

accounts for attenuation across the transmitted pulse, as discussed in Sigelmann and Reid [1973] and Hay [1991].

2.2 The Acoustic Mirror Image

Consider the two paths to a particle at height z_0 above the seabed illustrated in Figure 2.2. The first path directed along r is the direct arrival from the transducer located at height H above the bottom. Assume for now that the second path directed along r_1 and r_2 is from a specular reflection from the seabed, where specular refers to the angle of incidence equaling the angle of reflection. The assumption of specular reflection is addressed in the next section. It is important to note that the angles β and β' are greatly exaggerated in Figure 2.2, as neither of these angles ever exceed β_0 (2° in the RASTRAN system). Arrival times of transmitted pulses to the particle along these paths are calculated below relative to the time of transmission.

The first detected arrival is from the direct backscatter, whose raypath lies directly between the transducer and the particle. The arrival time of this echo is therefore,

$$t_1 = 2\left(\frac{r}{c}\right) = \frac{2}{c}\left(\frac{H - z_0}{\cos\beta'}\right) \tag{2.16}$$

The second arrival is from the direct bottom echo, at vertical distance H from the transducer face. The arrival time of this echo is,

$$t_{bottom} = 2\left(\frac{H}{c}\right). \tag{2.17}$$

In practice the bottom echo is often strong enough to saturate the receiving electronics and yields the strongest signal visible in the RASTRAN colour plots (typically bottom signals are in excess of 400 mV). The direct bottom echo is utilised only to define

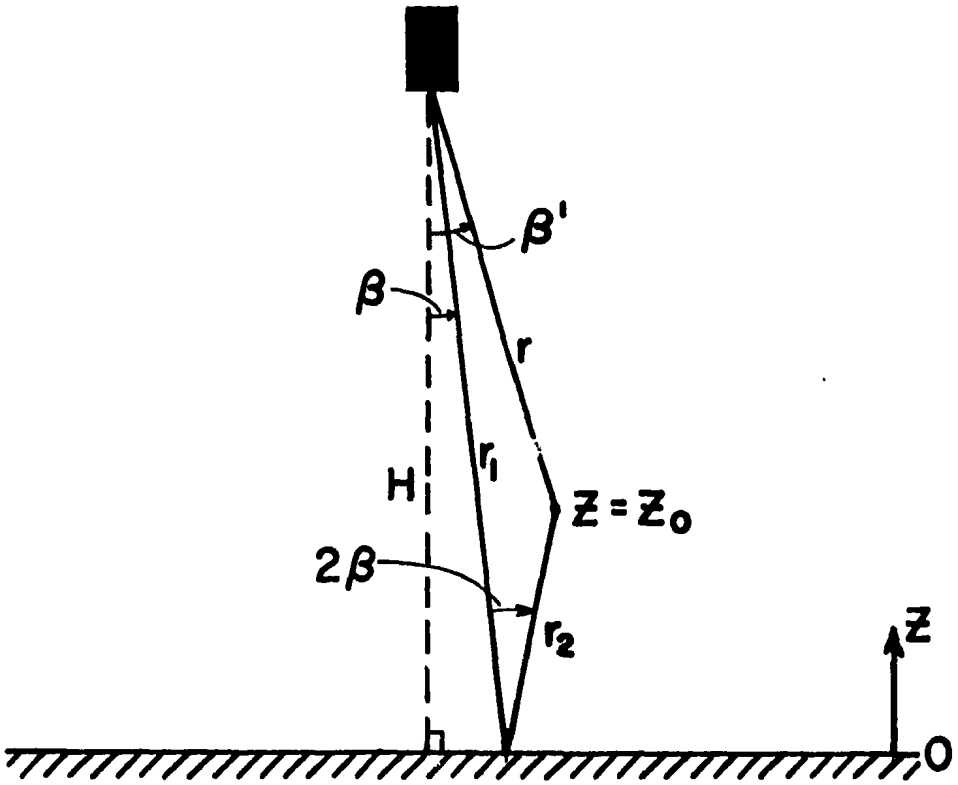

Figure 2.2: Direct, and alternate acoustic path to a particle by a bottom interaction.

the range to bottom. The third signal received is the specular re-reflected scattered wave, and involves two interactions with the bottom, via raypaths labelled r_1 and r_2 in Figure 2.2. The travel time along these raypaths is,

$$t_2 = \frac{2}{c}(r_1 + r_2) \tag{2.18}$$

or,

$$t_2 = \frac{2}{c}\left(\frac{H + z_0}{\cos\beta}\right). \tag{2.19}$$

Now consider the difference between t_1 and t_2 relative to the bottom arrival, t_{bottom}. First,

$$t_{bottom} - t_1 = \frac{2}{c}\left(H - \frac{H - z_0}{\cos\beta'}\right) \tag{2.20}$$

then,

$$t_2 - t_{bottom} = \frac{2}{c}\left(\frac{H + z_0}{\cos\beta} - H\right). \tag{2.21}$$

For small β and β' the cosines are approximately unity and therefore,

$$t_{bottom} - t_1 \cong t_2 - t_{bottom}. \tag{2.22}$$

Relation 2.22 shows that the arrival from the direct backscatter, and the arrival of the re-reflected backscatter, are equally displaced in time, and hence range, from the direct bottom arrival.

It should be noted that another arrival to the transducer exists which follows the path along r_1, r_2, and towards the transducer along r. For narrow beam pulsed acoustic systems these arrivals, however, are indistinguishable from the direct bottom arrival.

2.3 Bottom Reflection

The detection system employs a coherent, monochromatic transmitted pulse. The received signals are envelope detected, so that phase information from pulse to pulse is removed, and both coherent and incoherent waves contribute to the average detected signal. The transmitted pulse is incident on an irregular surface comprised of natural, irregular sand. The reflected wave will generally contain both coherent and incoherent components. The relative magnitude of the coherent and incoherent components depends upon the size of the surface roughness elements compared to the acoustic wavelength and direction of the incident wave. Stated another way, irregularity is an intrinsic property of the surface, but roughness is a relative property.

The degree of roughness is approximately assessed by using the Rayleigh criterion [Rayleigh, 1945; Ogilvy, 1991]. Figure 2.3 shows two incident rays, initially in phase, reflecting from an irregular surface. The phase difference, φ, between the two secondary wavelets in the plane of incidence upon reflection is

$$\varphi = k_c \left[\Delta h(\cos\theta_1 + \cos\theta_2) + \Delta x(\sin\theta_1 - \sin\theta_2)\right] \qquad (2.23)$$

where $\Delta h = h_1 - h_2$ is the difference in surface height, $\Delta x = x_2 - x_1$ is the horizontal separation of the rays, θ_1 is the incident angle, and θ_2 is the reflected angle. Both of these angles are measured from the normal of a suitable reference plane. The Rayleigh criterion states that for $\varphi \leq \pi/2$ the two reflected waves are mostly in phase and interfere constructively, thus the surface appears smooth. For $\pi/2 < \varphi \leq \pi$ the

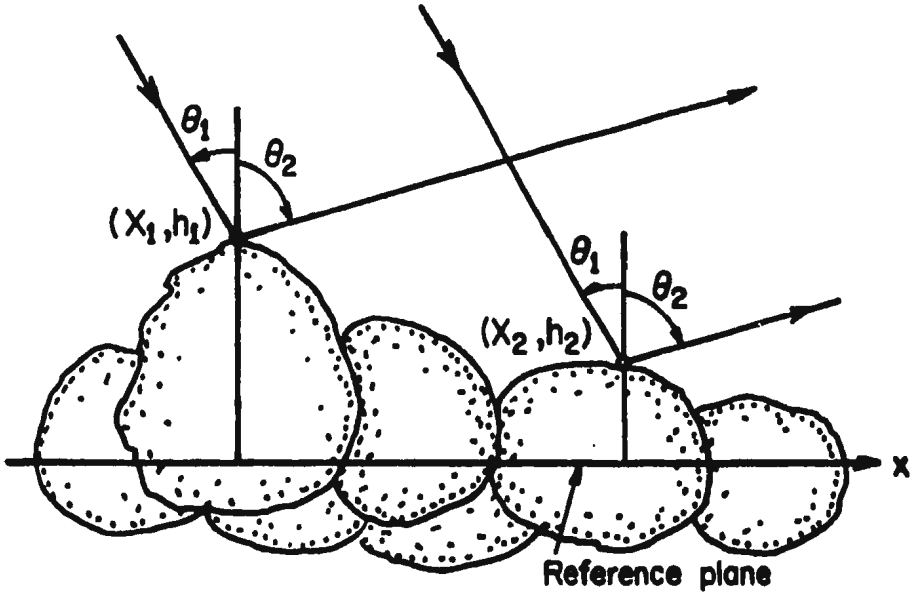

Figure 2.3: Geometry for definition of the Rayleigh criterion, adapted from Ogilvy [1991].

two reflected waves are mostly out of phase and interfere destructively, so the surface appears rough.

Surfaces that are generally irregular ($\Delta h \neq 0$) may or may not reflect the incident energy as though they are rough. In the specular direction ($\theta_1 = \theta_2$), the phase between the reflected waves is given by,

$$\varphi = 2k_c \Delta h \cos\theta_1. \tag{2.24}$$

If this is small compared to π for all points on the surface, the surface will appear as though it is mostly smooth. When this value is no longer small compared to π the amplitude in the specular direction will decrease. In the non-specular directions (diffuse) the phase difference between the two reflected rays is given by Equation 2.23. The phase of this energy is generally distributed over 0–2π as θ_2 varies, and has no fixed relationship with the phase of the incident field. The diffuse component is called the incoherent field. A summary of these statements is presented in Table 2.1.

	Specular $\theta_1 = \theta_2$	Diffuse $\theta_1 \neq \theta_2$
Smooth $\Delta h = 0$	$\varphi = 0$ *coherent*	None
Irregular $\Delta h \neq 0$	$\varphi = 2k_c \Delta h \cos\theta_1$ *coherent & incoherent*	$\varphi = k_c \Delta h(\cos\theta_1 + \cos\theta_2)$ $+k_c \Delta x(\sin\theta_1 - \sin\theta_2)$ *incoherent*

Table 2.1: Summary of terminology, and phase relationships based on Equation 2.23 for the two reflected rays depicted in Figure 2.3.

For randomly irregular surfaces Δh is replaced with the rms surface height σ with respect to some mean plane of reference. In analogy to Equation 2.24, for a surface

to be considered relatively smooth in the specular direction requires that,

$$R_a = k_c \sigma \cos\theta_1 \leq \frac{\pi}{4} \quad (= 0.78) \tag{2.25}$$

where R_a is called the Rayleigh parameter. The choice of $R_a \leq \pi/4$ is somewhat arbitrary but does represent the essential physics of the problem. From the Rayleigh parameter the reflection will be more specular if θ_1 approaches grazing incidence ($\theta_1 \rightarrow \pi/2$), or $k_c\sigma$ becomes small (long wavelength limit). Otherwise, the surface appears as though rough and the reflection becomes dominantly diffuse. To estimate R_a an estimate for the value of σ is required.

Direct surface measurements of σ for sand beds have not been made. Pace *et al.* [1985] conducted experiments using acoustic beams normally incident on a surface composed of natural smooth cobble. The value of σ (1.8 mm) measured by Pace *et al.* for this surface was approximately equal to the halfwidth (2 mm) of the cobble size distribution. This result can be understood as follows. Consider a vertical stack of a fixed number of particles. If the particles are all the same size, then the height of the stack will always be the same. If however, a distribution of sizes exist, then building the stack by randomly choosing particles from the distribution will result in a distribution of possible heights. The width of this height distribution is proportional to the width of the size distribution. To make this clear, the simple case of two particle sizes is considered. An idealised bed is made of stacked planes of spherical particles. One hundred layers were stacked, and this experiment was repeated 1000

times. Histograms of the height of the resulting heights, with the mean removed, are shown in Figures 2.4(a) and (b). Particles of similar size ($\frac{9}{10}$ and 1 unit) were used to generate Figure 2.4(a), while particles with a greater size difference ($\frac{1}{2}$ and 1 unit) were used to generate Figure 2.4(b).

The dependence of the surface height distribution on the width of the size distribution is demonstrated by Figure 2.4. For a narrow range of particle sizes in Figure 2.4(a) the surface height distribution is likewise narrow. Similarly, when the range of particle sizes is broader so is the distribution of surface heights. The surface height distributions of the top layer of particles in Figure 2.4 closely resembles a Gaussian distribution. (Note that in the model, the probability of obtaining a given height is governed by the binomial distribution, the limiting form of which for a large number of trials is the Gaussian distribution [Morse, p158, 1969].) Pace *et al.* remark that their measured surface height distribution was in poor agreement with the Gaussian distribution, however the acoustic results seemed insensitive to this discrepancy. Thus it is apparent that the necessity for Gaussian surface statistics can be relaxed.

The fullwidth of the size distribution for Stanhope Beach sand is 70μm [Hay and Sheng, 1992; Sheng, 1991], therefore following Pace *et al.*, $\sigma \simeq 35\mu$m. For normal incidence $\theta_1 = 0$, and the resulting Rayleigh parameters are 0.33 and 0.76 for 2.25 and 5 MHz, respectively. Thus, the seabed appears moderately rough at both frequencies, but less so at 2.25 MHz.

An often employed formalism in the theory of rough surface reflection is that of the

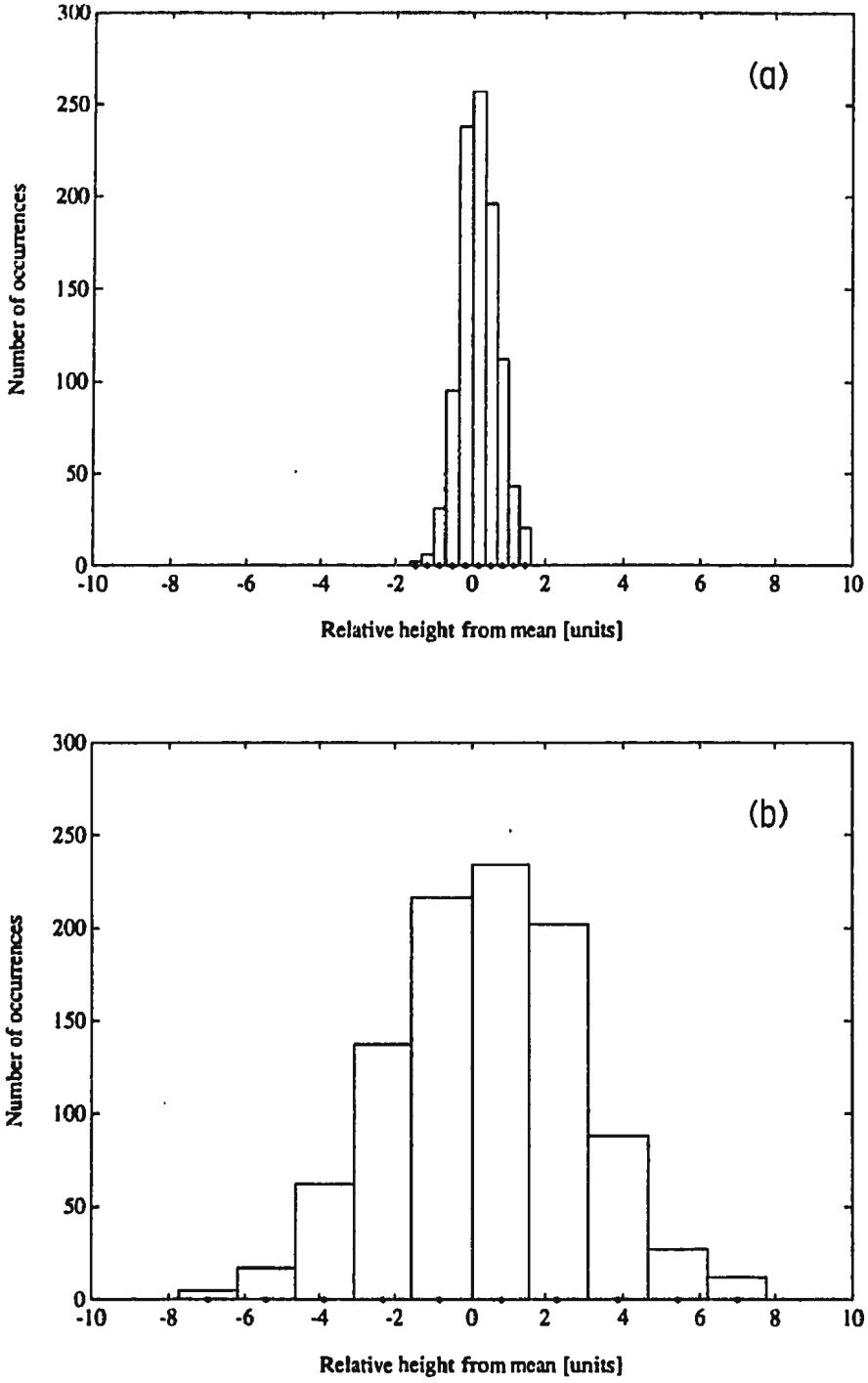

Figure 2.4: Modelled surface height distributions (mean removed) of the 100^{th} stacked layer using particle sizes: (a) $\frac{9}{10}$ and 1 units, and (b) $\frac{1}{2}$ and 1 units.

Helmholtz-Kirchhoff (H-K) integral. Thorne and Pace [1984] and Pace *et al.* [1985] have validated the H-K theory, using the second order phase approximation of Clay and Medwin [1977, p505]. As found in Pace *et al.* [1985], the total ensemble averaged reflected intensity, $\langle I \rangle$ for normal incidence backscatter, is given by

$$\langle I \rangle = \frac{R^2\, G^2\, D^2\, e^{-g}}{2\rho_0 c\, (H + z_0)^2} + \langle I_{incoh.} \rangle. \tag{2.26}$$

The first term on the right-hand side of Equation 2.26 is the contribution to the coherent reflected field. $\langle I_{incoh.} \rangle$ is the contribution to the incoherent reflected field, and is discussed below. R is the reflection coefficient, ρ_0 is the density of the propagation medium, c is the soundspeed in water, $G^2 = 2\rho_0 c I_o r_*^2$ is a source term where I_o is the sound intensity at range r_*, and g is called the roughness parameter, discussed next.

The roughness parameter is related to the Rayleigh parameter, and for normal incidence and specular reflection is expressed as

$$g = 4k_c^2\sigma^2. \tag{2.27}$$

Large and small g correspond to rough and smooth surfaces respectively, and surfaces with $g \sim O(1)$ are considered moderately rough. Equation 2.26 demonstrates the (exponential) decrease in the amplitude of the coherent field as g increases, as energy is transferred to the incoherent component of the field. The behaviour of the reflection as a function of increasing g is sketched in Figure 2.5. Using the above value for σ, the corresponding values of g at frequencies 2.25 and 5 MHz for Stanhope Beach are approximately 0.5 and 2.2. Both are of order unity, signifying a moderately rough

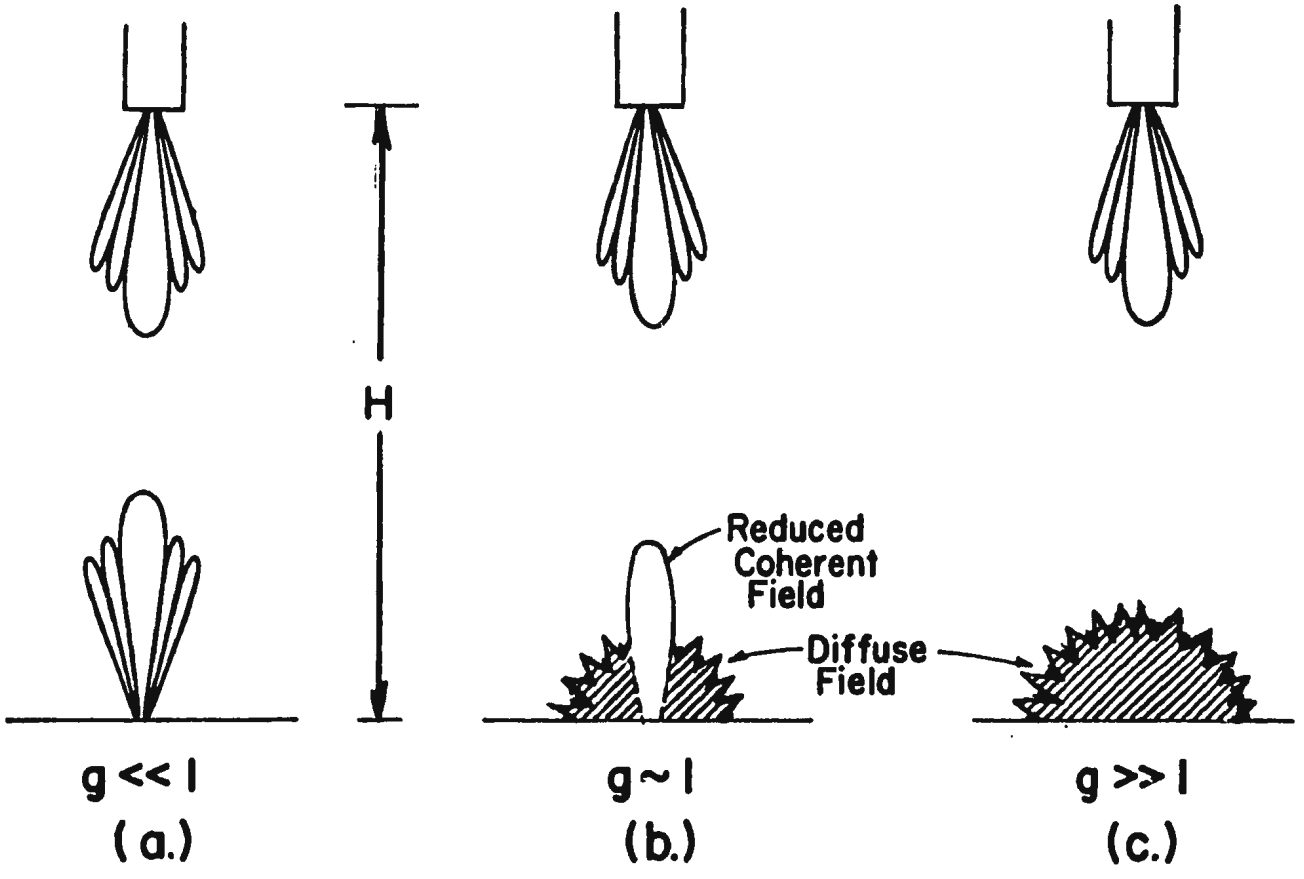

Figure 2.5: Shown are polar plots of the mirrored incident beam pattern for (a) a relatively smooth surface $g \ll 1$, (b) a moderately rough surface $g \sim 1$, and (c) a very rough surface $g \gg 1$.

surface.

Estimates of relative contributions to the incoherent and coherent field at 2.25 and 5 MHz are sought. Figure 2.6 illustrates the general problem. A specular raypath is denoted by the solid line. The dashed line shows a possible non-specular path for the transmitted pulse, and the dotted line shows a possible non-specular path for the scattered wave. In general, all possible combinations of incident and return non-specular raypaths must be accounted for.

From Pace *et al.* the contribution to the incoherent field reflected in the specular direction reduces for normal incidence to,

$$\langle I_{incoh.} \rangle = \frac{R^2\ G^2\ W^2}{16\ \rho_0 c\ H^2\ z_0^2} \left(\frac{T^2}{4\ \sigma^2} \right) g^2\ e^{-g}\ \Lambda(g, s, T) \tag{2.28}$$

where T is the surface autocorrelation length, and $W \simeq H \tan(\beta_0)$ is the beam halfwidth at range H. The function $\Lambda(g, s, T)$ is given by,

$$\Lambda(g, s, T) = \sum_{n=1} \frac{g^{n-1}}{n!} \frac{1}{(s\ T^2 + n)} \tag{2.29}$$

and is closely related to the confluent hypergeometric class of functions, specifically the incomplete gamma function [Abramowitz and Stegun, 1965, p262]. The quantity s is given by,

$$s = \frac{1}{2} \left(\frac{1}{W^2} + \frac{W^2\ k_c^2}{4} \left(\frac{1}{H} + \frac{1}{z_0} \right)^2 \right) \tag{2.30}$$

which for $z_0 \ll H$ and the frequencies considered here (MHz) reduces to,

$$s \simeq \frac{k_c^2\ W^2}{8\ z_0^2}. \tag{2.31}$$

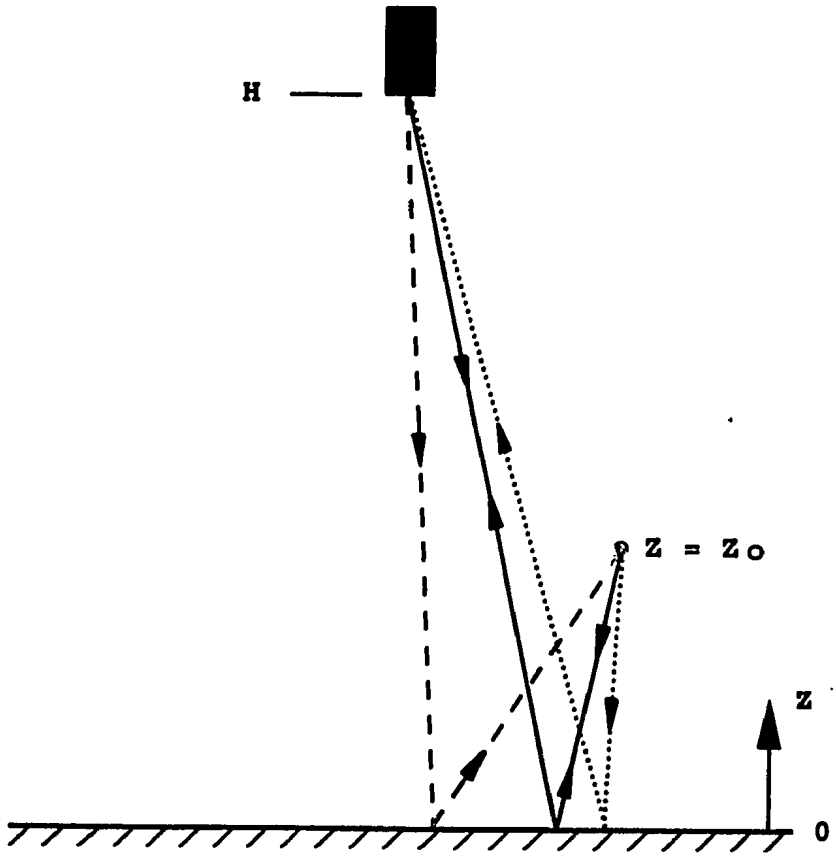

Figure 2.6: Geometry for specular (—) and non-specular (– – –) raypaths from the transducer to suspended sediment when the reflecting surface is rough. (· · · · · ·) shows a non-specular scattered raypath.

The ratio of incoherent to coherent contributions is then,

$$\frac{\langle I_{incoh.}\rangle}{\langle I_{coh.}\rangle} = \frac{W^2}{2z_0^2}\,(k_c^4\,\sigma^2\,T^2)\,\Lambda(g,s,T) \tag{2.32}$$

where $g = 4k_c^2\sigma^2$ and $D^2 \simeq 1$ have been used. Equation 2.32 shows the relative contribution to the incoherent field decreasing as one moves farther from the bottom (increasing z_0), and as the rms surface height σ decreases.

The cobble surface investigated by Pace *et al.* had a mean particle radius of $\overline{a} = 0.41$ cm, $T = 0.33$ cm, and $\sigma = 0.18$ cm. For their surface, therefore, $T \simeq 2\sigma$. Following this scaling for Stanhope Beach sand, $T \simeq 70\mu$m. For both frequencies, $W \simeq 4$ cm. At height 3 cm above the bottom ($z_0 = 3$ cm) values for sT^2 are 0.11 and 0.54, for 2.25 and 5 MHz, respectively. Using the above values for g, values of Λ are 1.0 and 1.4, for 2.25 and 5 MHz, respectively. Note that for these parameters, Λ displays weak dependence on frequency, and is of order unity. The ratio of incoherent to coherent reflected intensities estimated from Equation 2.32 are 0.05 and 1.6, for 2.25 MHz and 5 MHz, respectively. This calculation indicates that the incoherent component may play the dominant role at 5 MHz.

The H-K theory, however, requires that surfaces have small slopes, and large radii of curvature relative to the insonifying wavelength. This is manifest in the expression for the diffuse field as the surface autocorrelation length, T. For the H-K theory to be valid, the condition

$$\frac{4\pi}{\lambda}\left(\frac{T^2}{2\sigma}\right) \gg 1 \tag{2.33}$$

must be satisfied [Beckmann and Spizzichino, 1987, p193]. (The values for the left-hand side of Equation 2.33 for Pace *et al.* are 6.3 and 25.2 for their choice of frequencies.) Using $T = 0.8\overline{a}$, and $T = 1.8\sigma$ from Pace *et al.*, Equation 2.33 reduces to $k_c\overline{a} \gg 0.7$. This condition is not satisfied since for the Stanhope Beach measurements $k_c\overline{a} \sim O(1)$ (approximately 0.8 and 1.7, at 2.25 and 5 MHz, respectively). Moreover, since natural sand is irregular compared to smooth cobble it is likely that T is even smaller for sand relative to $\overline{a}$.

It is concluded that the H-K theory may not be directly applicable to the present problem. Nevertheless, it does serve to illustrate the important point that the incoherent component of the reflected intensity increases in importance as one approaches the surface, and that it is probably much less important at 2.25 MHz.

Thus far only reflection in the specular direction has been considered. In general, reflection from non-specular directions must be included to obtain the total reflected intensity at height z_0 (Figure 2.6). Furthermore, the intensity received at the transducer from the wave backscattered from a particle at height z_0 and re-reflected from the bottom (Figure 2.6), would in general also include non-specular raypaths (Figure 2.6). Including such rays in the problem would require knowledge of the angular dependence of scattering from sand particles. The angular dependence of scattering from irregular particles for $0.5 < x < 14$ has been considered for the optical case [Chýlek *et al.*, 1976], the angular dependence of sound scattering from sand in suspension is however not known.

To simplify the problem, only specular reflection will be considered. Furthermore, as both the incoherent and coherent components are proportional to the same reflection coefficient, R (Equations 2.26 and 2.28), the problem will be formulated in terms of a coherent incident wave. The validity of the approach will be tested by comparing suspended sediment concentrations obtained based on this assumption to concentrations obtained by other methods.

2.4 Pressure from the Mirror Signal

The pressure, p'_s, received at the transducer from a single particle, following the specularly reflected paths r_1 and r_2 in Figure 2.2, is now derived. The vertical distance to the sea-bottom is H. First consider the incident pressure, p'_i, felt by the particle via the specular bottom reflection. The total distance traveled by a transmitted pulse to the particle is $r_1 + r_2$, and the attenuation integrals are treated separately over the paths r_1 and r_2, thus,

$$\begin{aligned} p'_i &= RAD(\beta)\frac{p_* r_*}{(r_1 + r_2)} \exp\left\{ - \int_0^{\frac{H}{\cos\beta}} \alpha \, dr' - \int_{\frac{r}{\cos\beta}}^{\frac{H}{\cos\beta}} \alpha \, dr' \right\} \\ &\cong RAD(\beta)\frac{p_* r_*}{(r_1 + r_2)} \exp\left\{ - \int_0^{H} \alpha \, dr' - \int_{r}^{H} \alpha \, dr' \right\} \end{aligned} \tag{2.34}$$

using the small angle approximation for cosines. R is the specular reflection coefficient, assumed independent of β (for small β). The incident pressure, p'_i, is then backscattered from the particle thus returning to the transducer by retracing the incident path. Analogous to Equation 2.3, the received scattered pressure is written,

$$p'_s(r) \doteq R p'_i D(\beta) \left[\frac{a f_\infty(a,\pi)}{2(r_1 + r_2)} \right] \exp\left\{ - \left(\int_r^H \alpha \, dr' + \int_0^H \alpha \, dr' \right) \right\}. \tag{2.35}$$

Substituting p'_i into $p'_s(r)$,

$$p'_s(r_0) = AD^2(\beta) R^2 p_* r_* \left[\frac{a f_\infty(a,\pi)}{2 r_0^2} \right] \exp\left\{ -2 \left(\int_0^r \alpha \, dr' + 2 \int_r^H \alpha \, dr' \right) \right\} \tag{2.36}$$

where

$$r_0 = r_1 + r_2 \tag{2.37}$$

which is the total path length, and for small β

$$\int_0^H \alpha \, dr' = \int_0^r \alpha \, dr' + \int_r^H \alpha \, dr'. \tag{2.38}$$

The motivation for Equation 2.38 is to separate the total attenuation into regions above and below the range of interest, r. Forming the product $p_s' \cdot p_s'^*$, the mean square scattered pressure from the jth particle, $p_{sj}'^2(r_0)$ is,

$$p_{sj}'^2(r_0) = A^2 D^4(\beta) R^4 p_*^2 r_*^2 \left[\frac{a^2 \mid f_\infty(a,\pi) \mid^2}{4r_0^4}\right] \exp\left\{-4\left(\int_0^r \alpha \, dr' + 2\int_r^H \alpha \, dr'\right)\right\}. \tag{2.39}$$

In complete analogy to the derivation of Equation 2.9, substituting Equations 2.6, 2.7, and 2.39 into 2.5, the ensemble mean square scattered pressure from the mirror echo, $p_s'^2(r_0)$ is,

$$p_s'^2(r_0) = \frac{3}{8} A^2 R^4 \kappa \epsilon F'^2 p_*^2 r_*^2 \int_{r_0-\Delta}^{r_0+\Delta} \frac{1}{r_0'^2} \exp\left\{-4\left(\int_0^r \alpha \, dr' + 2\int_r^H \alpha \, dr'\right)\right\} dr_0' \tag{2.40}$$

where

$$\Delta = \frac{c\tau}{4} \tag{2.41}$$

and κ and $F^2$are as previously defined.

The integration over the transmitted pulse in Equation 2.40 must now be performed. Define this integral to be the function $L(r_0)$,

$$L(r_0) = \int_{r_0-\Delta}^{r_0+\Delta} \frac{1}{r_0'^2} \exp\left\{-4\left(\int_0^r \alpha \, dr' + 2\int_r^H \alpha \, dr'\right)\right\} dr_0'. \tag{2.42}$$

Substituting $\eta = r_0' - r_0$, we have,

$$L(r_0) = \int_{-\Delta}^{\Delta} \frac{1}{(\eta + r_0)^2} \exp\left\{-4\left(\int_0^{2H-r_0-\eta} \alpha\, dr' + 2\int_{2H-r_0-\eta}^{H} \alpha\, dr'\right)\right\} d\eta$$

$$\cong \frac{1}{r_0^2}\int_{-\Delta}^{\Delta} \exp\left\{-4\left(\int_0^{2H-r_0-\eta} \alpha\, dr' + 2\int_{2H-r_0-\eta}^{H} \alpha\, dr'\right)\right\} d\eta \qquad (2.43)$$

by using $\eta \ll r_0$. After some manipulation of the integrations over r' in Equation 2.43, $L(r_0)$ becomes,

$$L(r_0) = \frac{1}{r_0^2} \exp\left\{-4\left(\int_0^{2H-r_0} \alpha_s\, dr' + 2\int_{2H-r_0}^{H} \alpha_s\, dr' - r_0\alpha_0\right)\right\}$$

$$\times \int_{-\Delta}^{\Delta} \exp\left\{-4(\alpha_0 + \alpha_s)\eta\right\} d\eta \qquad (2.44)$$

where α has been separated into its constituent parts, α_0 and α_s. The integration over η yields,

$$\frac{c\tau}{2}\left(\frac{\sinh\zeta}{\zeta}\right) \qquad (2.45)$$

which illustrates the origin of 2.15 in Section 2.1. Finally, substituting 2.44, 2.45, and

$$r_0 \approx 2H - r \qquad (2.46)$$

the mean square scattered pressure for the mirror signal becomes,

$$p_s'^2(r) = \frac{3}{8}A^2R^4\kappa\epsilon F^2 p_*^2 r_*^2 \frac{c\tau}{2}\left(\frac{\sinh\zeta}{\zeta}\right)\frac{e^{-4(2H-r)\alpha_0}}{(2H-r)^2}$$

$$\times \exp\left\{-4\left(\int_0^{r} \alpha_s\, dr' + 2\int_{r}^{H} \alpha_s\, dr'\right)\right\}. \qquad (2.47)$$

2.5 Ratio of $p_s'^2$ to p_s^2

The ratio of the mirror echo to the direct backscatter, $p_s'^2/p_s^2$, eliminates the common terms involving the backscattering form-factor, beam directivity, and system sensitivity constant.

Explicitly, the ratio of Equation 2.47 to Equation 2.13 reduces to,

$$\frac{p_s'^2}{p_s^2} = R^4 \exp\left\{-8\left((H-r)\alpha_0 + \int_r^H \alpha_s\, dr'\right)\right\} \frac{r^2}{(2H-r)^2}. \tag{2.48}$$

RASTRAN utilises a time variable gain (TVG), which corrects for attenuation caused by the ambient fluid, α_0, and the loss due to spherical spreading. As a result the $\frac{r^2}{(2H-r)^2}$ term and the term involving α_0 may be dropped from Equation 2.48, and what remains is,

$$\frac{\tilde{p}_s'^2(r)}{\tilde{p}_s^2(r)} = R^4 \exp\left\{-8\int_r^H \alpha_s(r')\, dr'\right\} \tag{2.49}$$

Equation 2.49 is the basis for the inversion algorithm to convert acoustic signals to estimates of suspended sediment concentration near the sea bed.

There are several important features of the result in Equation 2.49. First, the integrated attenuation is due only to scattering between the range r and the bottom. Second, the result is independent of the backscatter form factor, $f_\infty(a,\pi)$, the projected beam's directivity, $D(\beta)$, and the system constant, A. Finally, the result depends on R^4.

The exponential term in Equation 2.49 contains α_s, which depends on acoustic frequency, mass concentration, and particle size. Provided the particle size is known

the function α_s provides the only connection between measured acoustic pressures on the left-hand side of Equation 2.49, and the mass concentration. For N uniformly sized particles per unit volume,

$$\alpha_s = \frac{N\Sigma_s}{2} \tag{2.50}$$

where Σ_s is the total scattering cross section for a single particle [Morse and Ingard, 1968, p426].

Sheng and Hay [1988] have constructed a model for the attenuation coefficient α_s based on the High-pass model of Johnson [1977]. The model is a rational polynomial that represents the overall shape of the data, and has the shape characteristic of a high-pass filter, hence its name. The High-pass model is written,

$$\frac{a\alpha_s}{\epsilon} = \frac{K_\alpha x^4}{[1 + \frac{4}{3}K_\alpha x^4 + \xi x^2]} \tag{2.51}$$

where $K_\alpha = (\gamma_k^2 + \gamma_\rho^2/3)/6$ and γ_k and γ_ρ are the compressibility and density contrasts between the scatterer and the ambient fluid respectively, and $x = k_c a$. ξ is an adjustable constant ≥ 1. For quartzlike sand, $\xi = 1$ is chosen to provide a better fit to experimental data at intermediate values of x, and the compressibility and density contrasts are $\gamma_k = -0.93$ and $\gamma_\rho = 0.77$ respectively, therefore $K_\alpha = 0.18$. Equation 2.51 was shown by Sheng and Hay [1988] to give good agreement with experimental attenuation data over the range $0 < x < 25$, and has been recently employed by other investigators [Thorne *et al.*, 1990; Vincent *et al.*, 1991]. For the range of particle sizes at Stanhope Beach values of $a\alpha_s/\epsilon$ at 5 MHz are roughly 5 to

8 times larger than at 2.25 MHz.

Using Equation 2.12 the mass concentration, M, is expressed in terms of the High-pass model,

$$M = \frac{[1 + \frac{4}{3}K_a x^{-1} + x^2]}{K_a x^{-1}} \rho_0 \, a \, \alpha_s, \tag{2.52}$$

for particles of uniform size. In the inversion scheme presented in the next chapter, uniform particle size is assumed to simplify the analysis. The effect of this assumption on the results is tested in Chapter 5.

Chapter 3

Inversion

This chapter presents the inversion scheme which permits suspended sediment concentration to be inferred from measured acoustic pressures. The left-hand side of Equation 2.49 is known completely, and the right-hand side contains the two unknowns, a and M, particle size and concentration respectively, through the use of Equation 2.52. Given a particle size, a, then M can be determined from Equation 2.49.

3.1 Description of Field Site and Data

The data analysed in this thesis are from a nearshore sediment transport experiment carried out at Stanhope Lane Beach in October-November 1989. Other results from this experiment have been presented elsewhere [van Hardenberg *et al.* 1991;

Hay and Sheng, 1992]. Stanhope Lane Beach is located on the central north coast of Prince Edward Island, and faces approximately north into the Gulf of St. Lawrence. The beach is characterised by a nearly continuous shelving sandy beach over a sandstone pebble pavement of variable width. Well sorted quartz sand with median grain sizes ranging between 0.16–0.30 mm comprise the beach material, and as one moves seaward from the beachface towards nearshore submerged bars, the median grain size decreases.

Three major bars, parallel to the shore, are shown in Figure 3.1 at 100 m, 200 m, and 380 m from the baseline. The RASTRAN instrument frame was deployed on the seaward face of the second sand bar, as illustrated in this Figure. The median grain size at this location is 170 μm.

Sediment characteristics relevant to the present problem include grain density, ρ_0', and particle size. Sand at Stanhope Lane Beach is mainly quartz, which has a bulk grain density of 2.65 g/cm^3 [Clarke, 1966]. Natural sediments generally follow a log-normal size distribution [Hatch and Choate, 1929; Einstein 1950; Chow, 1954; Flammer, 1962], where the analytic expression for the log-normal size distribution is,

$$n(a) = \frac{1}{\sqrt{2\pi}\,\ln a_g}\,\frac{1}{a}\exp\left[-\frac{(\ln a - \ln a_g)^2}{2\ln^2 \sigma_g}\right], \tag{3.1}$$

where a_g and σ_g are particle geometric mean radius and geometric standard deviation, respectively. For Stanhope Beach, $a_g = 79\mu m$ and $\sigma_g = 1.25$ provide a good fit to the data, as illustrated in Figure 3.2 from Sheng [1991].

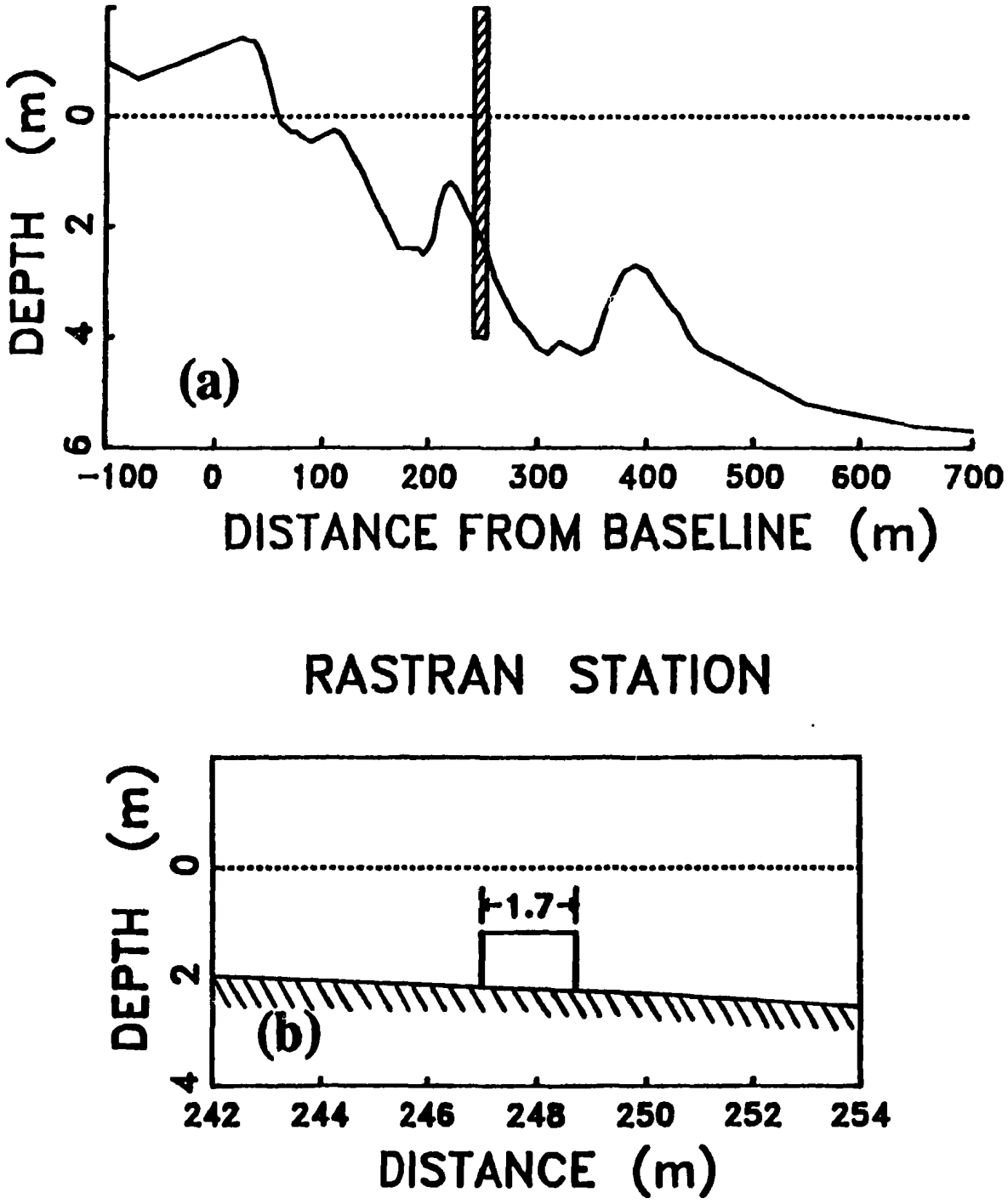

Figure 3.1: (a) Beach profile at Stanhope Lane, Prince Edward Island. (b) The deployment location of the RASTRAN system, showing RASTRAN frame, with no vertical exaggeration. (from Sheng, 1991)

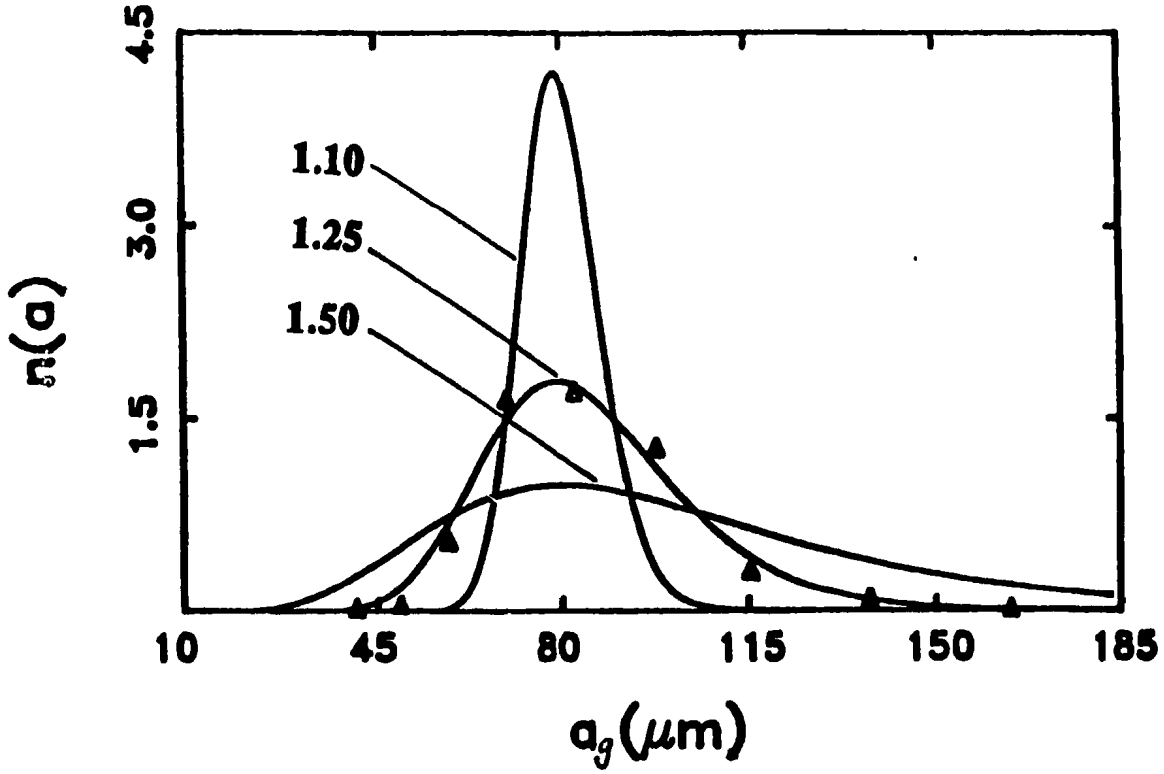

Figure 3.2: The log-normal size distribution for Stanhope Lane Beach sand.

The positioning of instruments on the RASTRAN frame is shown in plan and end view in Figure 3.3. A cluster of three acoustic sounders operating at the frequencies 1, 2.25, and 5 MHz respectively, and a fourth sounder operating at 2.25 MHz located a distance of 1.45 m shoreward from the cluster, are mounted approximately 1 metre above the seabed. The three clustered transceivers are referred to as channels 1A, 2B, and 5C, and the shoreward transducer is designated as channel 2D. Connections to the shore-based data acquisition system are via armoured cables. Other instruments on the seaward end of the frame include: a 3 element vertical array of optical backscatter sensors (OBS) located at nominal heights of 5, 10, and 15 cm respectively above the seabed, and three Marsh- McBirney electromagnetic flowmeters to measure on- off-shore current at nominal heights of 20, 50, and 100 cm respectively above the seabed. On the shoreward end of the frame, the same number of OBS's and one flowmeter were fastened similarly. All data from non-acoustic instruments were recorded on the Dalhousie University UDATS (Underwater Digitization and Transmission System) system [Hazen *et al.*, 1987].

3.2 The RASTRAN System

A comprehensive description of the RASTRAN system is provided elsewhere [Hay, *et al.*, 1988], and only a summary is given here. Acoustic pulses of 20 μs duration, are transmitted at 10 ms intervals into the water column simultaneously by individual

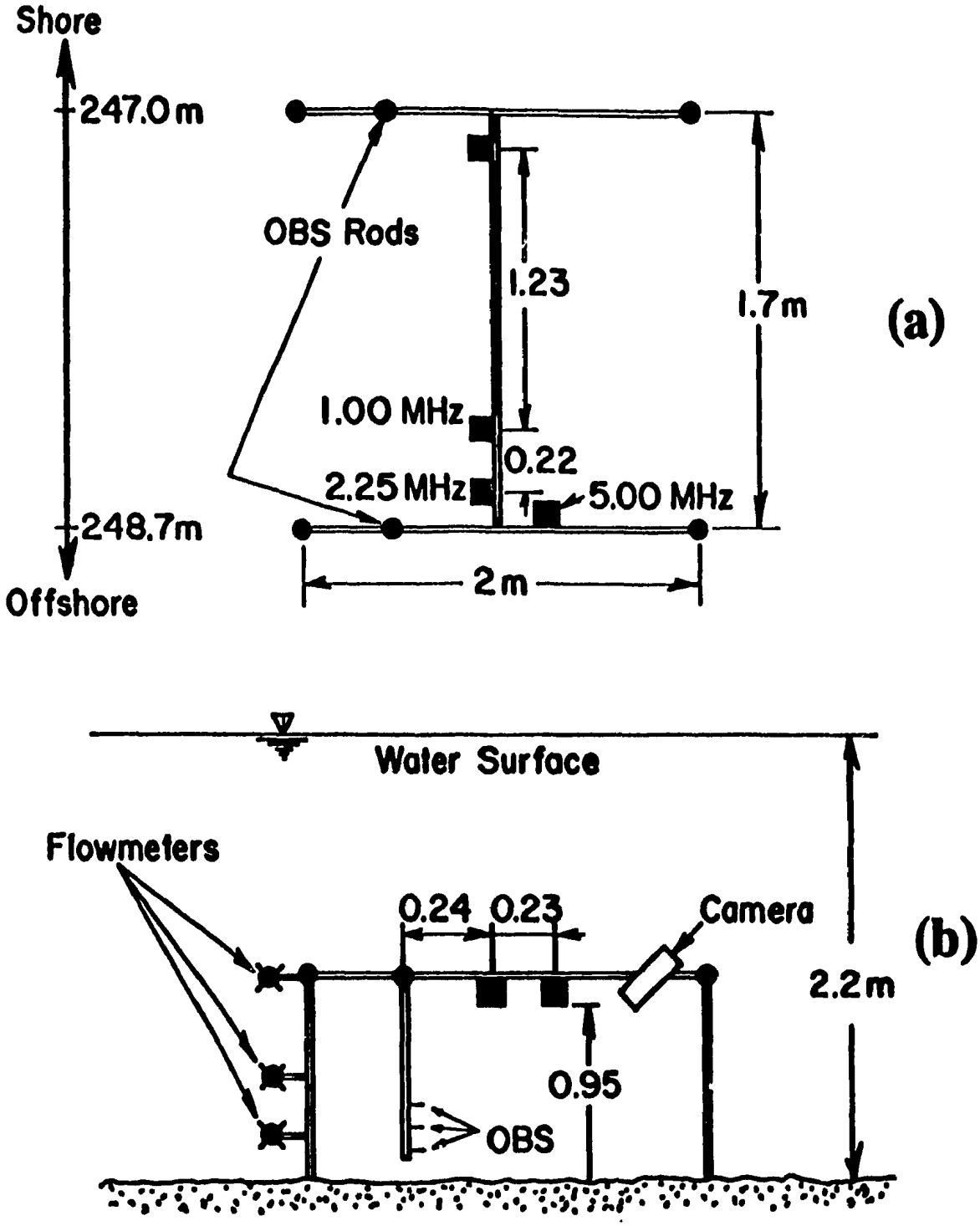

Figure 3.3: Instrument frame configuration for the 1989 field experiment at Stanhope Lane Beach. (a) Plan view. (b) End view, looking shoreward. Distances are in metres. (from Sheng, 1991)

Mesotech 810 submersible narrowband acoustic sounders, operating at the centre frequencies listed above. A summary of the transducer characteristics for each frequency of operation is provided in Table 3.1.

Freq. [MHz]	a_o [cm]	r_c [cm]	β_0 [deg.]
1.00	1.09	25.2	2.00
2.25	0.47	10.6	2.05
5.00	0.24	6.1	1.85

Table 3.1: a_o is the radius of the transducer. r_c is the farfield critical range. β_0 is the half beamwidth chosen at the -3 dB points of the beam's main lobe.

Received echoes are then TVG corrected and heterodyned down to a centre frequency of 455 kHz. The heterodyned signal is full-wave rectified and low-pass filtered in an envelope detector. It is noteworthy in the present context that this detection method removes phase information, so that both the coherent and incoherent components of the signal are detected. Analogue to digital conversion is then performed at a sampling rate of 200 kHz, and 5 consecutive samples are averaged. The information is therefore averaged over 25 μs in the data acquisition software, and assuming a sound-speed in water of 1500 m/s, the vertical resolution for a range bin is approximately 1.85 cm. The results of 4 consecutive pings are then ensemble averaged and stored at a rate of 6.6 Hz.

RASTRAN data files also contain information from OBS instruments, and flowme-

ters. Typical field runs lasted 6.5 minutes and result in files of roughly 1.2 megabytes. An example of RASTRAN data obtained during the 1989 deployment at Stanhope Beach exhibiting the acoustic mirror is presented in Figure 3.4. The effects of acoustic mirroring are seen in this figure during two main suspension events centred at approximately 0.3 and 4.5 minutes, respectively, and are strongly correlated with the OBS and flowmeter observations at the top of this figure.

The naming convention for the RASTRAN files is as follows: the first three numbers represent the Julian day when the data was collected, and the three digit extension represents the sequential data run collected on that day. Thus 300.030 means this data was the thirtieth (030) run collected on Julian Day 300 (Oct. 27) 1989.

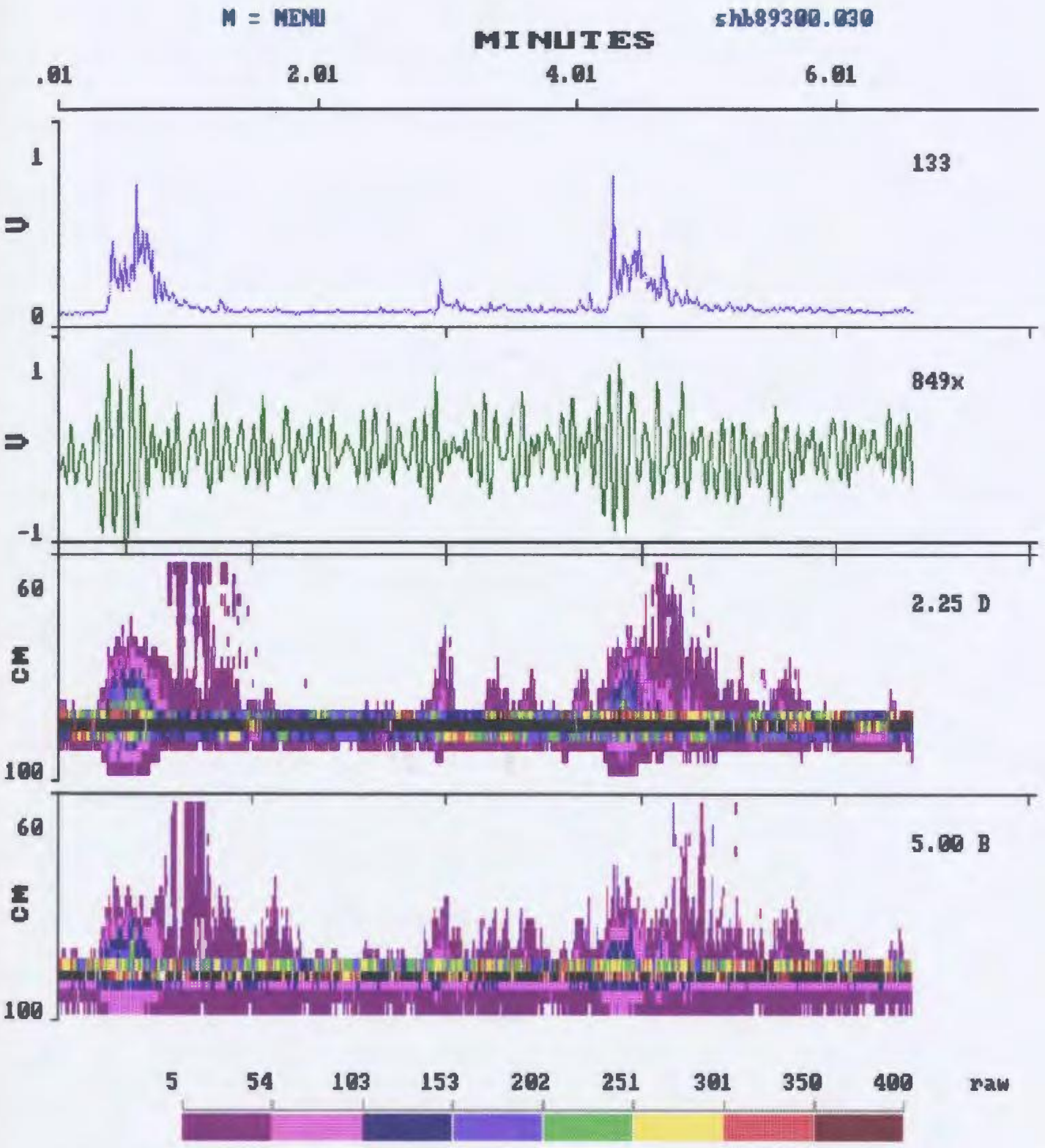

Figure 3.4: Run 300.030 data from Stanhope Lane 1989 deployment. Blue curve is the OBS record in units of volts: 1 V = 10 g/ℓ; green curve is the cross–shore current in volts: 1 V = 0.6 cm/s. Beneath these are the colour images of the raw acoustic data for the nearshore 2.25 MHz transducer, and the offshore 5 MHz transducer. Colour palette values are in mV.

3.3 The Inversion Scheme

This section presents the inversion algorithm that permits suspended sediment concentration to be computed from single frequency acoustic data. Although the algorithm depends on reflection from the seabed, it is shown that the final result is independent of the bottom reflection coefficient without approximation. The method described below is referred to henceforth as the *reflection method.*

Let the variable z be the height above the bottom using the coordinate transformation, $z = H - r$, where r is the range from the transducer, and H is the range to bottom from the transducer. Equation 2.49 of Section 2.5 can be rewritten in terms of these coordinates as,

$$\frac{\tilde{p}_s'^2(z)}{\tilde{p}_s^2(z)} = R^4 \exp\left\{-8\int_0^z \alpha_s(z')\,dz'\right\}. \tag{3.2}$$

The pressure from the mirror echo, $\tilde{p}_s'^2(z)$, is physically due to interaction with particles a distance z above the bottom, but will appear visually in the displayed data a distance z *below* the main bottom echo. A calibration factor, S, relates received acoustic pressure and recorded voltage, v, linearly by,

$$v(z) = S\tilde{p}_s(z) \tag{3.3}$$

permitting Equation 3.2 to be written in terms of recorded voltages,

$$\frac{v'^2(z)}{v^2(z)} = R^4 \exp\left\{-8\int_0^z \alpha_s(z')\,dz'\right\}. \tag{3.4}$$

Each range bin contains one voltage which is the bin average applied to the centre of the bin. To reflect the discrete nature of the data, replace z by z_N, where z_N is the distance from the (sediment) bottom to the centre of the N^{th} range bin above the bottom. For example, if the main bottom echo is in the $52nd$ range bin from the transducer, then $v(z_2)$ corresponds to the voltage in range bin 50, and $v'(z_2)$ corresponds to the voltage in range bin 54. Furthermore, these voltages are obtained after removing any background voltages from the total voltage. The background was simply taken as the smallest signal in the time series for each range bin. In general, if the bottom echo is in the b^{th} bin from the transducer, that requires data from the i^{th} range bin where,

$$i = \begin{cases} b - N & \text{for } v_N(z_N) \\ b + N & \text{for } v'_N(z_N) \end{cases} \tag{3.5}$$

Figure 3.5 illustrates this. Equation 3.5 reveals a limitation of the inversion since $b + N$ must be less than, or equal to, the number of range bins in a set. Thus, in the above example, $b = 52$, and the ratio on the left-hand side of Equation 3.4 cannot be evaluated for more than 3 range bin widths from the bottom since in the Stanhope experiment only 55 bins were stored.

Proceeding, Equation 3.4 is now written,

$$\frac{v'^2_N}{v^2_N} = R^{\,4} \exp\left\{-8 \int_0^{z_N} \alpha_s(z')\, dz'\right\} \tag{3.6}$$

where $v'^2_N = v'^2(z_N)$ and $v^2_N = v^2(z_N)$ are used for convenience. Since α_s is required to obtain the concentration, M, it is removed from the exponential in Equation 3.6

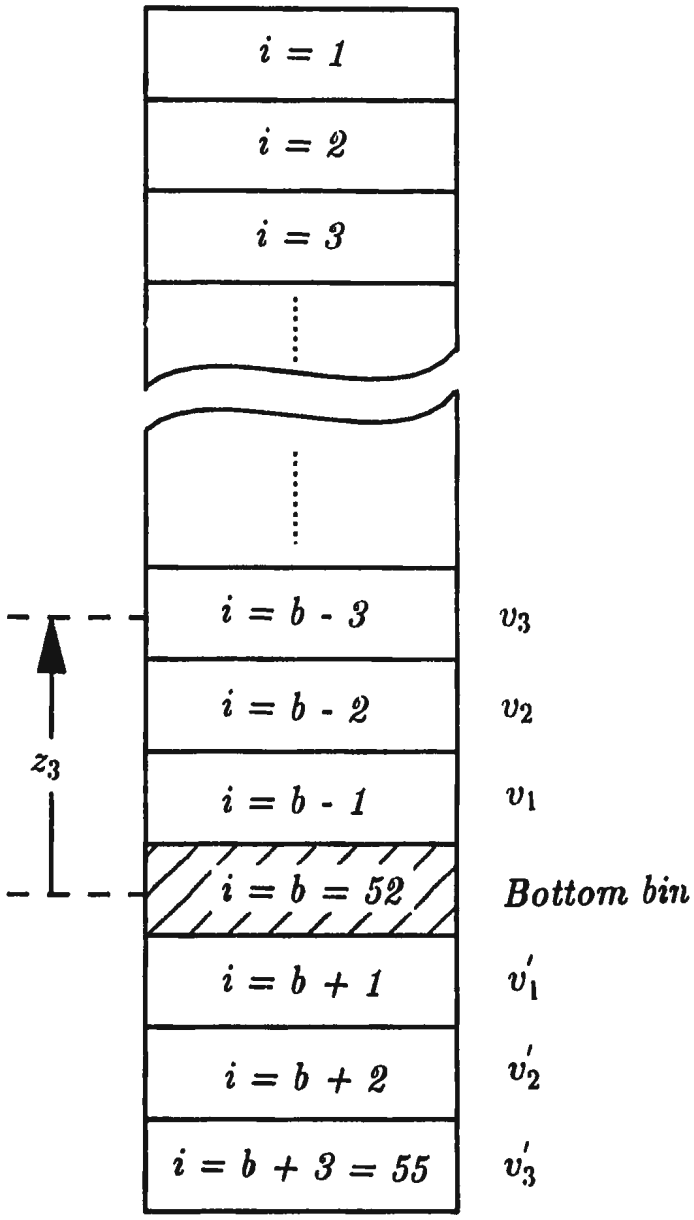

Figure 3.5: Illustration for example described in the text showing the use of the variables v_N^2, $v_N'^2$, and z_N, when the *set* contains 55 bins, and the bottom echo is in bin 52. Three voltage ratios are formed in this case.

by taking the logarithm of both sides. The equation is then,

$$\ln\left(\frac{v'_N}{v_N}\right)^2 = \ln R^4 - 8\int_0^{z_N} \alpha_s \, dz'. \tag{3.7}$$

To reduce variance in the final result a time–average of Equation 3.7, denoted by $\langle\cdots\rangle$, yields,

$$\langle \ln\left(\frac{v'_N}{v_N}\right)^2 \rangle = \ln R^4 - 8\int_0^{z_N} \langle\alpha_s\rangle \, dz' \tag{3.8}$$

where it is tacitly assumed that the bottom remains stationary with respect to the transducer over the duration of the time–average so that,

$$\langle \ln R \rangle = \ln R. \tag{3.9}$$

Defining the quantity,

$$\Gamma_N \equiv \langle \ln\left(\frac{v'_N}{v_N}\right)^2 \rangle \tag{3.10}$$

Equation 3.8 becomes,

$$\Gamma_N = \ln R^4 - 8\int_0^{z_N} \langle\alpha_s\rangle \, dz' \tag{3.11}$$

From Equation 3.11 and the definition of Γ_N it follows that

$$\Gamma_{N-1} = \ln R^4 - 8\int_0^{z_{N-1}} \langle\alpha_s\rangle \, dz' \tag{3.12}$$

provided $N \neq 1$, since Γ_0 is not defined. Subtracting 3.11 from 3.12 removes all dependence on the reflection coefficient and leaves the expression,

$$\Delta\Gamma_N = \Gamma_{N-1} - \Gamma_N = 8\int_{z_{N-1}}^{z_N} \langle\alpha_s\rangle dz'. \tag{3.13}$$

The integral on the right-hand side of Equation 3.13 is between two adjacent bin centres. When the integral is expressed as a sum over discrete data, each bin contributes half of its value to the sum, thus,

$$8\int_{z_{N-1}}^{z_N} \langle \alpha_s \rangle \, dz' = 8\Delta z \sum_{i=N-1}^{N} \frac{1}{2} \langle \alpha_{s,i} \rangle \tag{3.14}$$

where Δz is the width of a range bin, and $\alpha_{s,i}$ is the attenuation due to scattering in the i^{th} bin above the bin containing the bottom echo. The sum on the right-hand side of Equation 3.14 is recognised as being the average between the two adjacent bin centres, and so the average is applied to the boundary between these bins. So it is not confused with the time average we denote this average in space between the bin centres by an overbar, and define it by,

$$\overline{\langle \alpha_s \rangle}_N \equiv \sum_{i=N-1}^{N} \frac{1}{2} \langle \alpha_{s,i} \rangle. \tag{3.15}$$

Using 3.14 and 3.15 Equation 3.13 is

$$\overline{\langle \alpha_s \rangle}_N = \frac{1}{8\Delta z} \Delta \Gamma_N. \tag{3.16}$$

All of the quantities on the right-hand side of Equation 3.16 are known from the acoustic data. The High-pass model of Chapter 2 can be re-expressed to give suspended sediment concentration at the lower boundary of the N^{th} bin in terms of the scattering attenuation,

$$\overline{M}_N = \frac{[1 + \frac{4}{3} K_\alpha \langle x \rangle^4 + \langle x \rangle^2]}{K_\alpha \langle x \rangle^4} \, \rho_0' \, \overline{\langle a \rangle}_N \, \overline{\langle \alpha_s \rangle}_N \tag{3.17}$$

where $\overline{\langle a \rangle}_N$ is the vertically averaged particle size at the lower edge of the N^{th} bin, $\langle x \rangle = k_c \overline{\langle a \rangle}_N$, and use has been made of the approximation,

$$\langle \frac{[1 + \frac{4}{3} K_\alpha x^4 + x^2]}{K_\alpha x^4} \rangle \approx \frac{[1 + \frac{4}{3} K_\alpha \langle x \rangle^4 + \langle x \rangle^2]}{K_\alpha \langle x \rangle^4}, \tag{3.18}$$

which assumes that particle size for each height above bottom remains constant over time. Over the duration of each event this is likely to be true. To first order the size profile should remain relatively stationary over the duration of the run.

Equations 3.16 and 3.17 enable the sediment mass concentration to be computed upon assuming a value of $\overline{\langle a \rangle}_N$. Values of $\overline{\langle a \rangle}_N$ used in the inversion are from vertical size profiles obtained from the multifrequency inversion of Stanhope Beach data [Hay and Sheng, 1992]. In terms of $\Delta\Gamma_N$,

$$\overline{M}_N = \frac{[1 + \frac{4}{3} K_\alpha \langle x \rangle^4 + \langle x \rangle^2]}{K_\alpha \langle x \rangle^4} \, \rho_0' \frac{\overline{\langle a \rangle}_N}{8\Delta z} \, \Delta\Gamma_N. \tag{3.19}$$

The result in Equation 3.19 does not depend on the reflection coefficient R. Also, the inversion does not permit concentration estimates to be made in the first range bin above the bottom, since Γ_0 is not defined. Moreover, the system utilises a 20 μs pulse and averages over 25 μs intervals. Thus part of the bottom echo is placed into an adjacent range bin above, or below, the range bin containing most of the bottom echo. As the bottom echo is strong, this can contaminate values of Γ_1, thence $\overline{M}_2$.

Chapter 4

Data Processing

This chapter describes computer based methods employed to estimate mass concentrations using the model for the mirror-image echo presented in the previous chapter. All software described in this chapter are implemented in Fortran77, and computations are carried out on a RISC based MIPS/120-5 workstation.

There are two major file selection criteria for choosing data appropriate to the objective of the thesis. The first criterion is that a file must clearly exhibit the mirror effect. Files that met this criterion also show that wave groups incident upon the beach were very well defined. The second criterion is that the main bottom echo must clearly occupy one range bin in the RASTRAN colour plots (Note that this does not exclude the possibility of signal leakage into adjacent bins). Moreover, the range bin in which the bottom echo resides cannot change over the duration of a suspension event.

It was found that of the 3 frequency transceiver cluster data gathered, the 5 MHz transceiver met these criteria most frequently, and was closer to the bottom, thus providing more range bins in the mirror echo. Data gathered by the shoreward 2.25 MHz transceiver (2D) are also of interest in this study since this transceiver is in shallower water providing longer post-bottom echoes than the offshore cluster. Furthermore, at 2.25 MHz the bottom reflection is expected to be more specular than at 5 MHz, and both attenuation due to scattering and chemical absorption are decreased.

4.1 General Processing Scheme

The treatment of the data is illustrated in Figure 4.1. Raw acoustic data in binary format is first smoothed with a 7 *set* moving average, where a set is a block of contiguous range bins as in Figure 3.5. Using a sampling rate of 6.6 Hz a 7 set average translates to a 1.1 second average. This preliminary step is the same as the multifrequency inversion [Sheng, 1991; Hay and Sheng, 1992]. The 7 set smoothed files are further smoothed with a 41 set, or approximately 6 second, moving average. The motivation for further smoothing is to reduce the variance in time averaged $\ln(v_N'^2/v_N^2)$ terms. This filters out the effects of individual surface waves (typical period 4–5 s) on the suspension.

The programs **inv2D** and **inv5** (described in the next section) read the 2.25 and

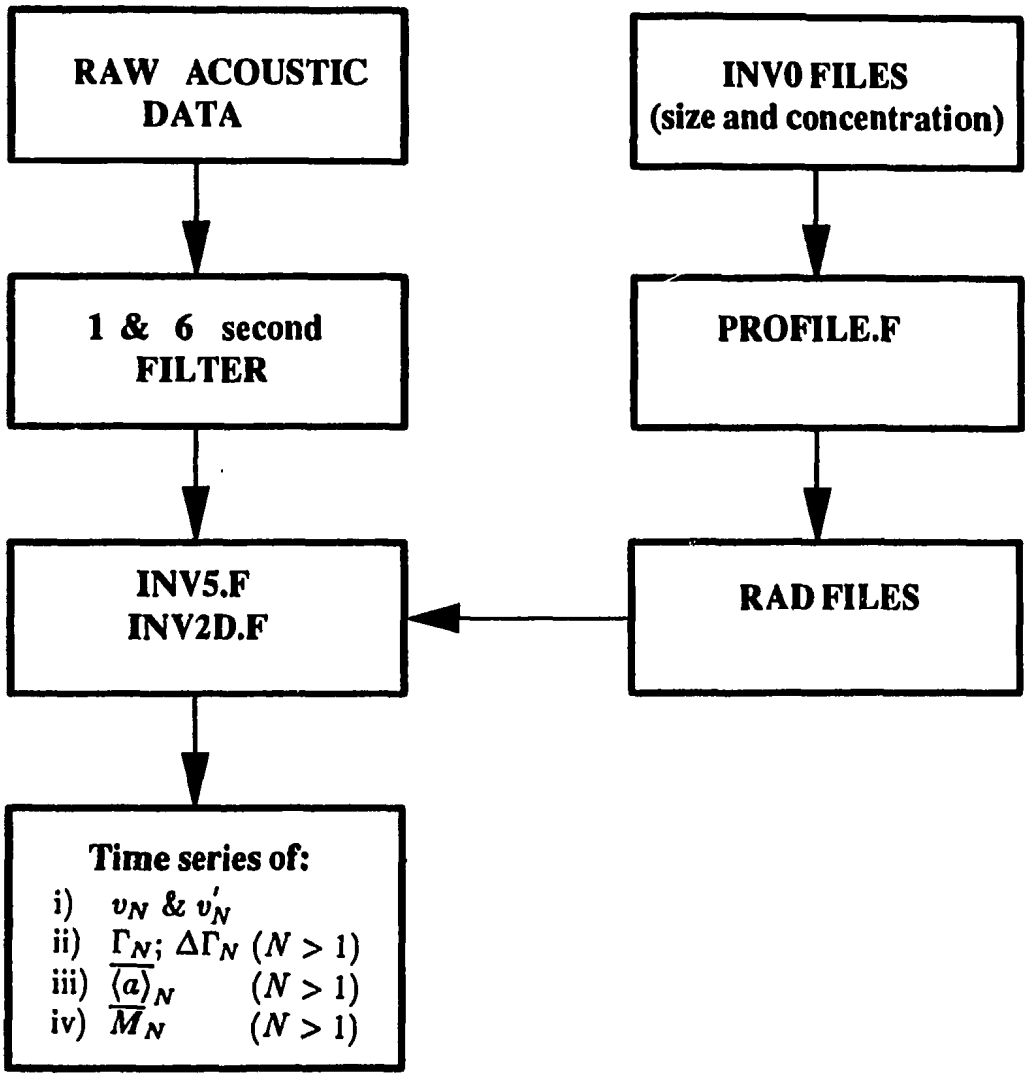

Figure 4.1: Block diagram showing evolution of data from raw form to end results.

5 MHz channels from the 41 set smoothed data, respectively, and require particle size information. A program called **profile**, reads the size files from the multifrequency inversion and averages the time series over the duration of the file, producing a file containing an average particle size, and standard deviation, for the centre of each range bin — these files are called **rad** files. Both **inv2D** and **inv5** read **rad** files, proceeding then to invert the acoustic data to obtain mass concentration. The output of these inversion programs is a collection of ascii files c ntaining time series of the inversion's intermediate computations, and the final mass concentration time series.

4.2 Description of the Inversion Programs

Figure 4.2 shows a flow chart of the Fortran programs **inv2D** and **inv5**. Only major points are discussed here. For the selected file, the required user inputs are: the bottom bin number, b; the number of sets for block time averaging, Q, which provides the $\langle \cdots \rangle$ in Equation 3.8; and the name of the appropriate **rad** file. Since the Mesotech 810 acoustic sounders utilise a factory preset TVG based on temperature and salinity values differing from field values, field values of T and S for a particular RASTRAN data run must also be entered to permit a TVG correction.

The general procedure is to step through the file in contiguous blocks of Q sets each. A value of $Q = 20$ sets produces two estimates of concentration over the filter length. Averaging over fewer sets is not meaningful. For each block, a loop is executed

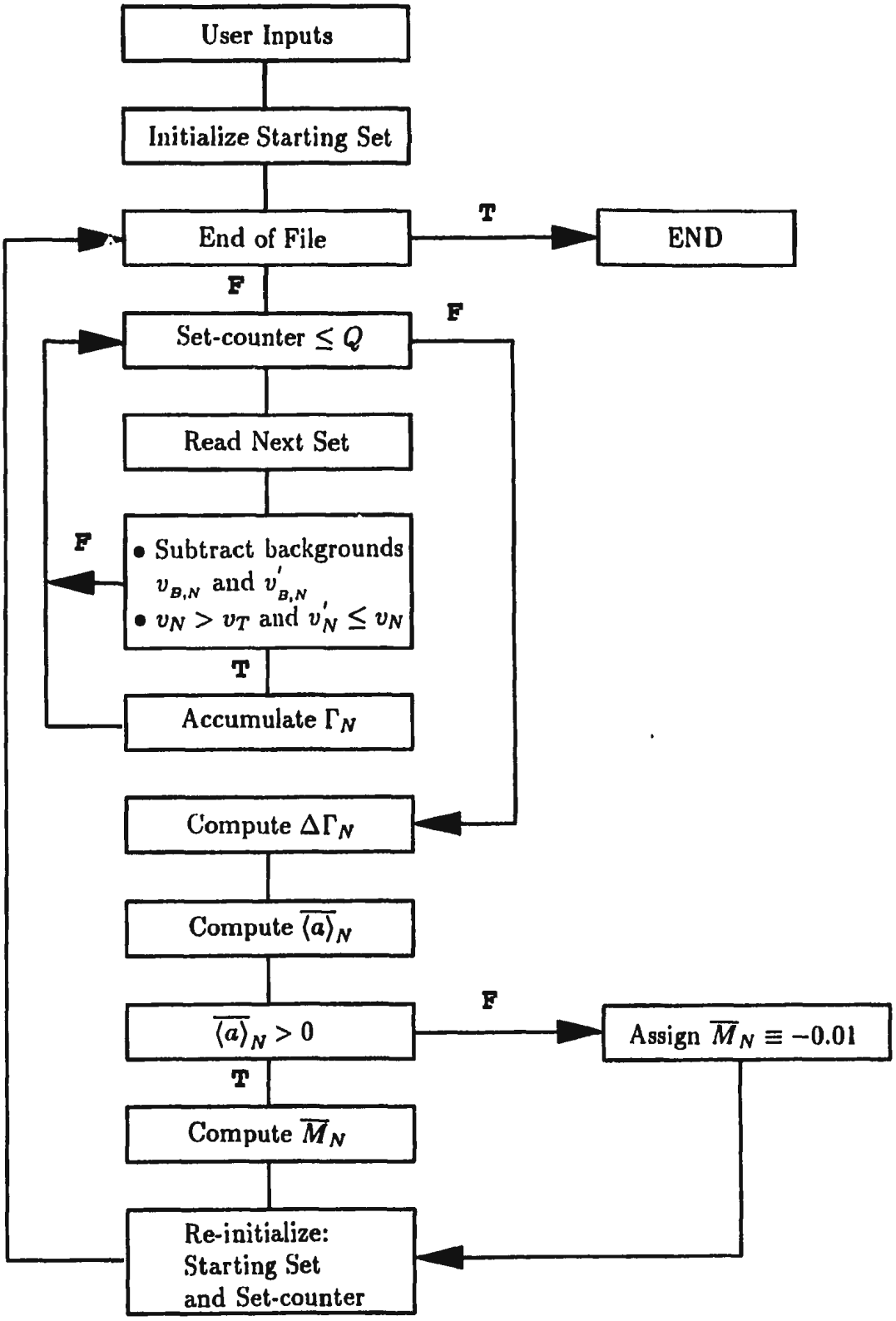

Figure 4.2: Block diagram for the inversion programs **inv2D** and **inv5**.

through Q sets, and accumulates acceptable values of $\ln(v_N'^2/v_N^2)$, where v_N' and v_N include a background signal subtraction. The value of N spans $N = 1 \ldots 55 - b$, the number of squared-voltage ratios available. The values of $\ln(v_N'^2/v_N^2)$ considered to be acceptable are those for which the criterion,

$$\frac{v_N'}{v_N} \leq 1 \tag{4.1}$$

where the voltages have been background corrected, is true. If this ratio were otherwise, it would imply that the reflection coefficient were greater than unity, which is impermissible on physical grounds. A further criterion is that the direct backscatter signal must be above a threshold voltage, v_T. This avoids computing concentration estimates when the above criteria are met, but are meaningless due to low signal levels. Once Q sets have been looped through, the average of $\ln(v_N'^2/v_N^2)$ is computed and stored, accounting properly the number of acceptable sets. Next, a value of $\Delta\Gamma_N$ is computed. Values of $\Delta\Gamma_N$ less than zero are unacceptable since α_s must be positive. When $\Delta\Gamma_N$ is negative it is an indication that the method has failed for that block of Q sets. For $\Delta\Gamma_N > 0$ the program proceeds and computes the scattering attenuation and then the mass concentration, $\overline{M}_N$, which is archived on disk. The case $\Delta\Gamma_N = 0$ is rare in practice. An example of these intermediate calculations is provided in Figures 4.3 and 4.4.

All output time series are of approximately 130 data points in length. Typical program execution time on a complete file of RASTRAN data for one acoustic frequency

takes about 30 seconds.

4.3 Confidence Limits based on Signal Fluctuations

Confidence limits for mass concentration time series presented in Chapter 5 are based on fluctuations in $\Delta\Gamma_N$. Recalling that,

$$\Delta\Gamma_N \equiv \Gamma_{N-1} - \Gamma_N \tag{4.2}$$

and,

$$\Gamma_N \equiv \langle \ln \left(\frac{v'_N}{v_N} \right)^2 \rangle, \tag{4.3}$$

the dependence of M_N on $\Delta\Gamma_N$ (Equation 3.19) is,

$$\overline{M}_N = \frac{[1 + \frac{4}{3} K_\alpha \langle x \rangle^4 + \langle x \rangle^2]}{K_\alpha \langle x \rangle^4} \rho'_0 \frac{\overline{\langle a \rangle}_N}{8\Delta z} \Delta\Gamma_N \tag{4.4}$$

Fluctuations in $\Delta\Gamma_N$, thence $\overline{M}_N$, are related to fluctuations in the acoustic data, v_N^2 and $v_N'^2$. These fluctuations need not be noise, but rather real fluctuations in signal due to varying suspended sediment concentrations.

The inversion programs compute the standard deviation of Γ_N for each N, for each block of Q sets, indicated by the symbol ε_N. It follows that minimum and maximum possible values of Equation 4.2 can be reasonably represented by,

$$\begin{aligned} \Delta\Gamma_N^- &= (\Gamma_{N-1} - \varepsilon_{N-1}) - (\Gamma_N + \varepsilon_N) \\ \Delta\Gamma_N^+ &= (\Gamma_{N-1} + \varepsilon_{N-1}) - (\Gamma_N - \varepsilon_N) \end{aligned} \tag{4.5}$$

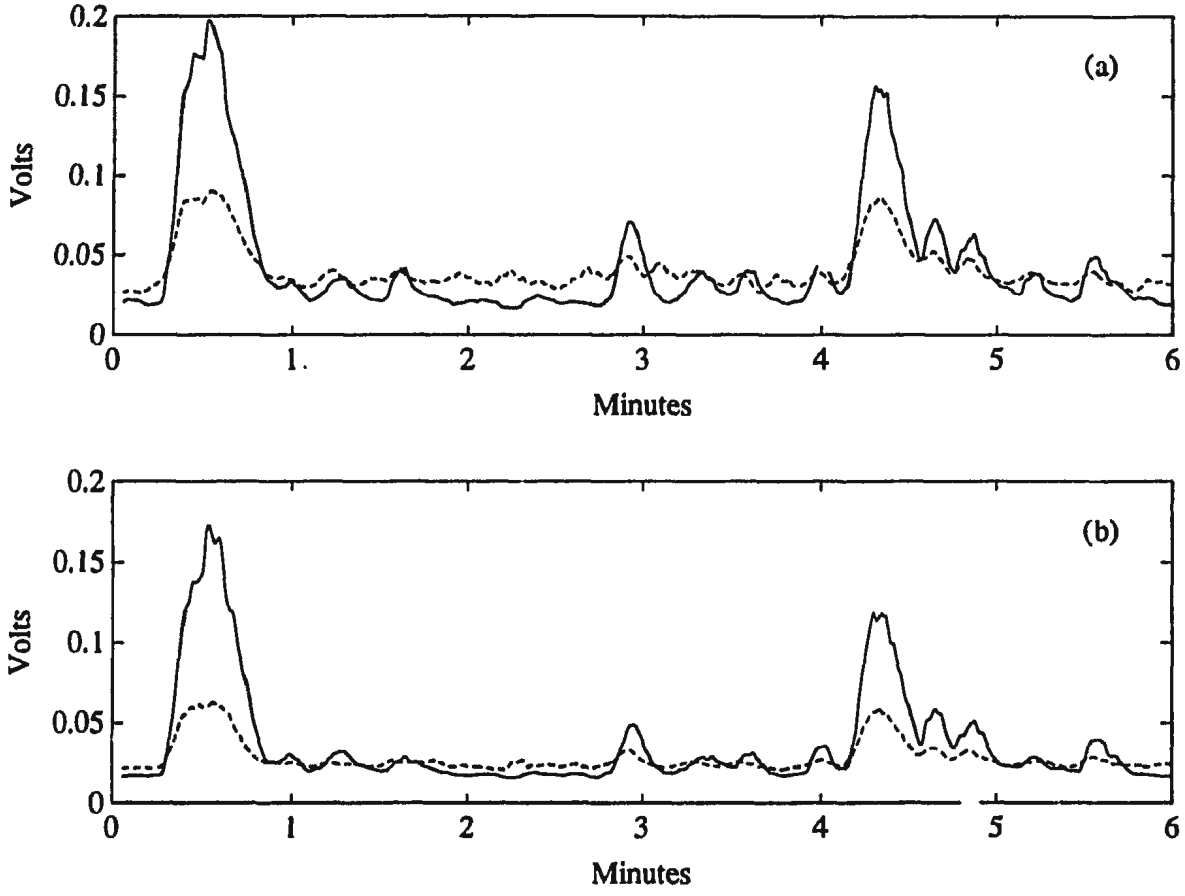

Figure 4.3: Data from run 300.030, at 5 MHz. (a) Raw voltage for V_2 (—) and mirror signal V_2' (- - -). (b) Raw voltage for V_3 (—) and mirror signal V_3' (- - -).

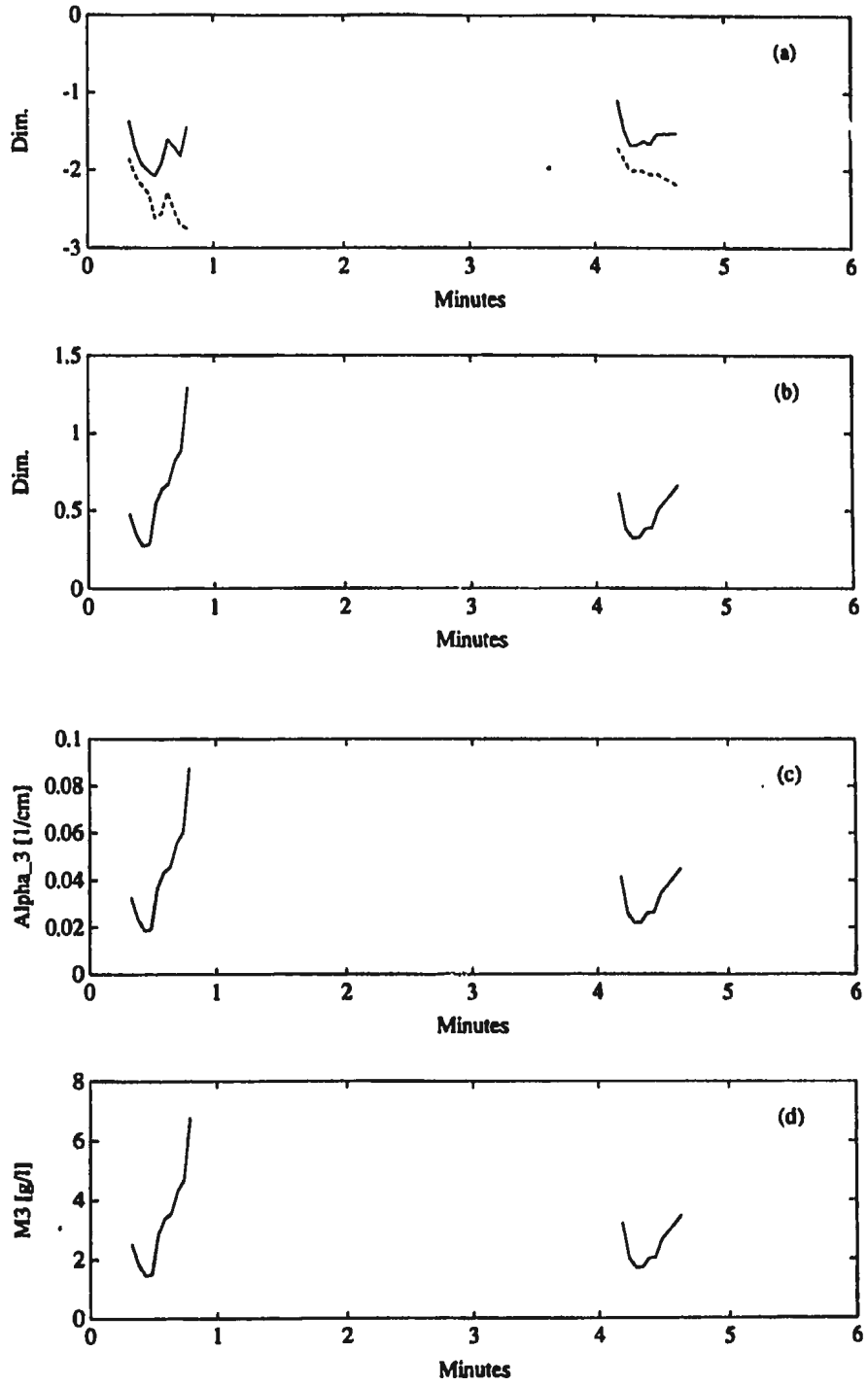

Figure 4.4: Data from run 300.030, at 5 MHz. (a) Computed values for Γ_2 (—) and Γ_3 (- - -) after background levels have been removed from the raw data. (b) Computed value for $\Delta\Gamma_3$, (c) Computed value for $\alpha_{s,3}$ ($= \frac{\Gamma_2 - \Gamma_3}{8\Delta z}$), and (d) Computed concentration $\overline{M}_3$.

respectively. Making use of,

$$\overline{\langle \alpha_s \rangle}_N^{\pm} = \frac{1}{8\Delta z} \Delta \Gamma_N^{\pm} \tag{4.6}$$

the limits $\overline{M}_N^-$ and $\overline{M}_N^+$ define minimum and maximum values for the mass concentration based on these fluctuations respectively, where,

$$\overline{M}_N^{\pm} = \frac{[1 + \frac{4}{3} K_\alpha \langle x \rangle^4 + \langle x \rangle^2]}{K_\alpha \langle x \rangle^4} \rho_0' \, \overline{\langle a \rangle}_N \, \overline{\langle \alpha_s \rangle}_N^{\pm}. \tag{4.7}$$

The values obtained from Equation 4.7 are used for placing confidence limits on results presented in the next chapter.

4.4 Confidence Limits based on Errors in Particle Size

Confidence in mass concentration estimates obtained from Equation 4.7 also depend on the uncertainty in $\overline{\langle a \rangle}_N$. For the employed inversion scheme this value does not change in time, therefore what uncertainty exists in the mass concentration due to error in radius will also be invariant in time. A simple test of the sensitivity of the High-pass model to changes in $\overline{\langle a \rangle}_N$, and hence x, is to hold the value of the attenuation constant for each 2.25 and 5 MHz, while varying a over the range plus and minus one standard deviation from the mean profile radius, denoted by $\overline{\langle a \rangle}_N^{+}$ and $\overline{\langle a \rangle}_N^{-}$, respectively. Thus, Equation 4.7 is written,

$$\overline{M}_N^{\mp} = \frac{[1 + \frac{4}{3} K_\alpha \langle x^{\pm} \rangle^4 + \langle x^{\pm} \rangle^2]}{K_\alpha \langle x^{\pm} \rangle^4} \rho_0' \overline{\langle a \rangle}_N \pm \overline{\langle \alpha_s \rangle}_N \tag{4.8}$$

where $\langle x^{\pm} \rangle \equiv k_c \overline{\langle a \rangle}_N^{\pm}$.

Figure 4.5 shows the 6.5 minute averaged particle size vertical profile for run 300.030 obtained from the multifrequency inversion, and the program **profile**. The solid line in this Figure represents $\overline{\langle a \rangle}_N$, and the dashed lines represent the one standard deviation limits on this value. The range over which a varies lies approximately between 60 μm and 140 μm, the mean value being near 100 μm.

Recalling Equation 2.51 for the High-pass model,

$$\frac{a\alpha_{s,i}}{\epsilon} = \frac{K_\alpha x_i^4}{[1 + \frac{4}{3} K_\alpha x_i^4 + x_i^2]} \tag{4.9}$$

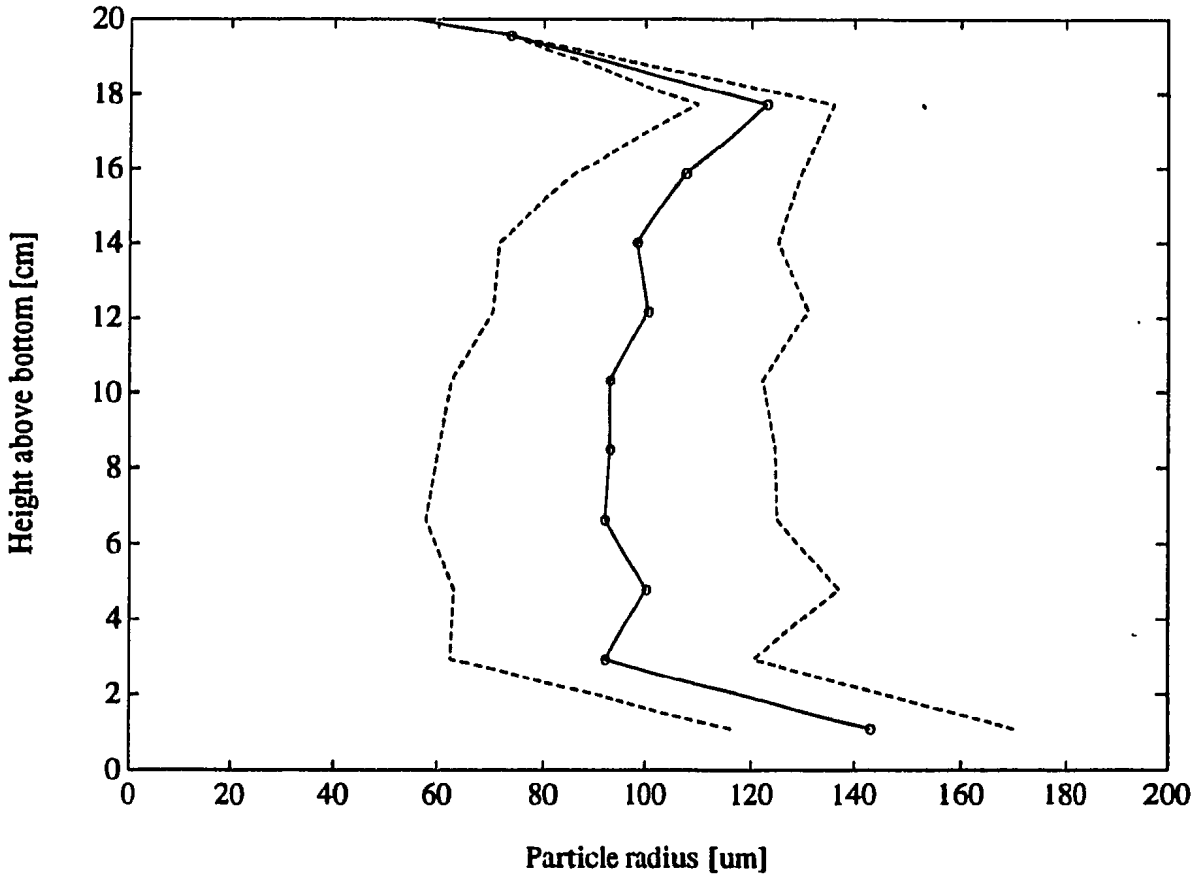

Figure 4.5: File-averaged (6.5 minutes duration) radius profile for run 300.030. The solid line represents the mean value, and the dashed lines represent one standard deviation from the mean.

where $\epsilon = M/\rho_0'$, and $x_i(= k_i a)$ and $\alpha_{s,i}$ represent the dimensionless size parameter and scattering attenuation for the i^{th} frequency in MHz, respectively. For a fixed time and height above the sea bottom the quantity a/ϵ is the same for any frequency. To estimate the relative values of the scattering attenuation at the two frequencies $i = 2.25$ and $i = 5$, Equation 4.9 is used to obtain,

$$\frac{\alpha_{s,2.25}}{\alpha_{s,5}} = \frac{x_{2.25}^4}{x_5^4} \times \frac{[1 + \frac{4}{3}K_\alpha x_5^4 + x_5^2]}{[1 + \frac{4}{3}K_\alpha x_{2.25}^4 + x_{2.25}^2]}. \tag{4.10}$$

For a typical particle radius of 100 μm, and using $K_\alpha = 0.18$ for quartz, this reduces to,

$$\alpha_{s,2.25} \approx 0.22\ \alpha_{s,5}. \tag{4.11}$$

A typical value for $\alpha_{s,5}$ during the peak of an event is 0.04 cm^{-1} which leads to a predicted value of $\alpha_{s,2.25} = 0.009$ cm^{-1}.

Using these values for $\alpha_{s,i}$, M as a function of x (for radii 60 μm to 140 μm) at 2.25 and 5 MHz is depicted in Figure 4.6 by the dashed and solid lines respectively. The circles represent predicted concentrations at x values for a particle of the mean radius, 100 μm. There are two salient features in this figure: first, at the mean radius the two frequencies give nearly identical results, approximately 3 g/ℓ in this example; second, at 2.25 MHz the possible range of concentration is much greater than at 5 MHz, especially for smaller particles.

The High-pass model given by Equation 2.51 is renormalised so that neither side depends explicitly on the particle radius, a, but rather on the acoustic wavenumber,

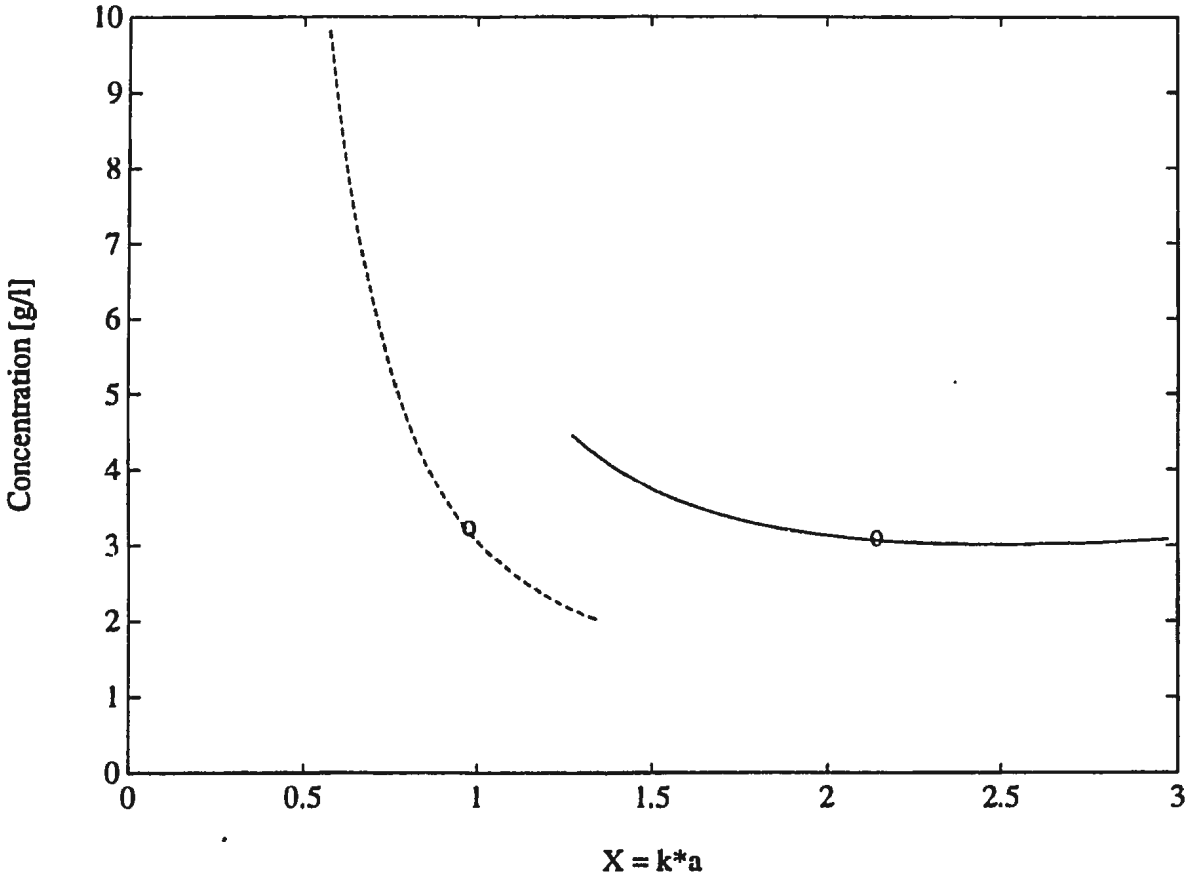

Figure 4.6: Dependence of M on changing particle size through the variable x, using the High-pass model of scattering attenuation. The dashed line represents M vs. $x_{2.25}$, and the solid line represents M vs. x_5. The value for α_s has been fixed at 0.04 cm^{-1} and the value for α_s at 2.25 MHz has been fixed at 0.009 cm^{-1}. The circles represent inverted concentrations for a particle size of 100μm at each frequency.

k_c. This is achieved by dividing each side of Equation 2.51 by the dimensionless size parameter, x. The resulting expression is,

$$\frac{\alpha_s}{\epsilon k_c} = \frac{K_\alpha x^3}{[1 + \frac{4}{3} K_\alpha x^4 + x^2]}. \tag{4.12}$$

The right-hand side of this function is plotted in Figure 4.7 where the circles on the curve represent the range of x spanned by particles of radius $60\mu m \geq a \geq 140\mu m$ at 2.25 MHz, and the x's represent the same thing at 5 MHz. One can clearly see the sensitivity of the High-pass model near $x \simeq 1$, or equivalently at 2.25 MHz for the considered particle size range. In contrast, the curve is a much slower changing function over the same range of particle radii at 5 MHz. This sensitivity at 2.25 MHz to particle size is supported by Figure 4.6.

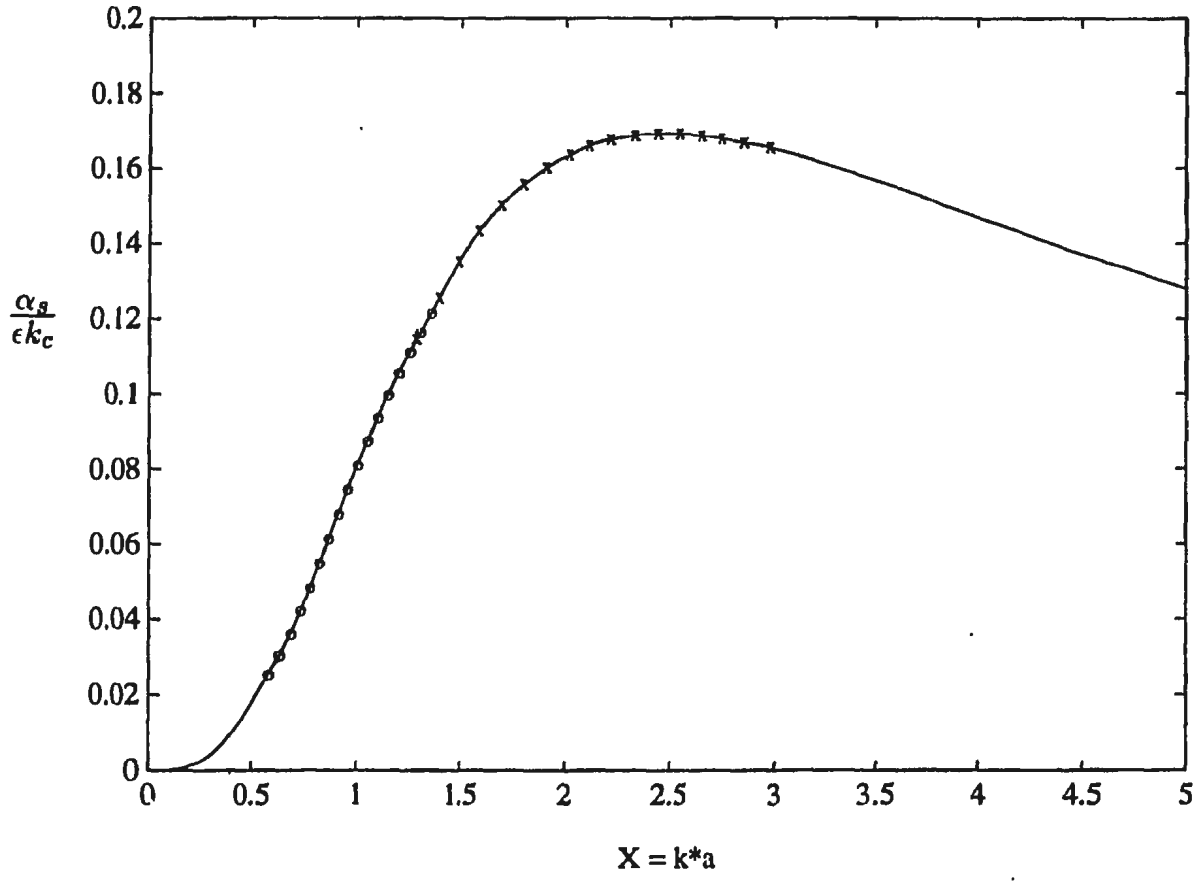

Figure 4.7: The High-pass model renormalised such that neither side depends explicitly on the particle radius, a. Circles represent the range of x spanned by a particles of radii $60\mu m \geq a \geq 140\mu m$ at 2.25 MHz; x's represent the range of x spanned by the same particles at 5 MHz.

4.5 Sensitivity of Mass Concentration to Background Subtraction

As shown in Equation 4.4, the inverted concentration, $\overline{M}_N$, depends on $\Delta\Gamma_N$, rewritten here for convenience,

$$\overline{M}_N = \frac{[1 + \frac{4}{3}K_\alpha\langle x\rangle^4 + \langle x\rangle^2]}{K_\alpha\langle x\rangle^4}\ \rho_0'\ \overline{\langle a\rangle}_N\ \frac{\Delta\Gamma_N}{8\Delta z}. \tag{4.13}$$

Figure 4.8 shows a representative time series, taken from run 300.030, of total signal for the third bin above the bottom, v_3. From Figure 4.8 it is clear that the total signals consist of a constant bias, or background, plus the signal containing information about a suspension event. (Throughout the thesis the voltages, v_N and v_N', are assumed to be only that part of the total signal containing information about a suspension event.) Assigning the variables V_N and V_N' for the total signals N bins above and below the bottom bin respectively, and the constants $v_{B,N}$ and $v_{B,N}'$ for the corresponding background signals, Equation 4.2 becomes,

$$\Delta\Gamma_N = \langle \ln\left(\frac{V_{N-1}' - v_{B,N-1}'}{V_{N-1} - v_{B,N-1}}\right)^2 \rangle - \langle \ln\left(\frac{V_N' - v_{B,N}'}{V_N - v_{B,N}}\right)^2 \rangle. \tag{4.14}$$

It is important to understand how the background signals, and their subsequent treatment, affect the final estimates of mass concentration. Computing ratios in Equation 4.14 will introduce uncertainty when the numerator and denominator inside each logarithm approach zero together. This applies directly to Equation 4.14 when the total signals, V_N and V_N', approach the background values, $v_{B,N}$ and $v_{B,N}'$, almost

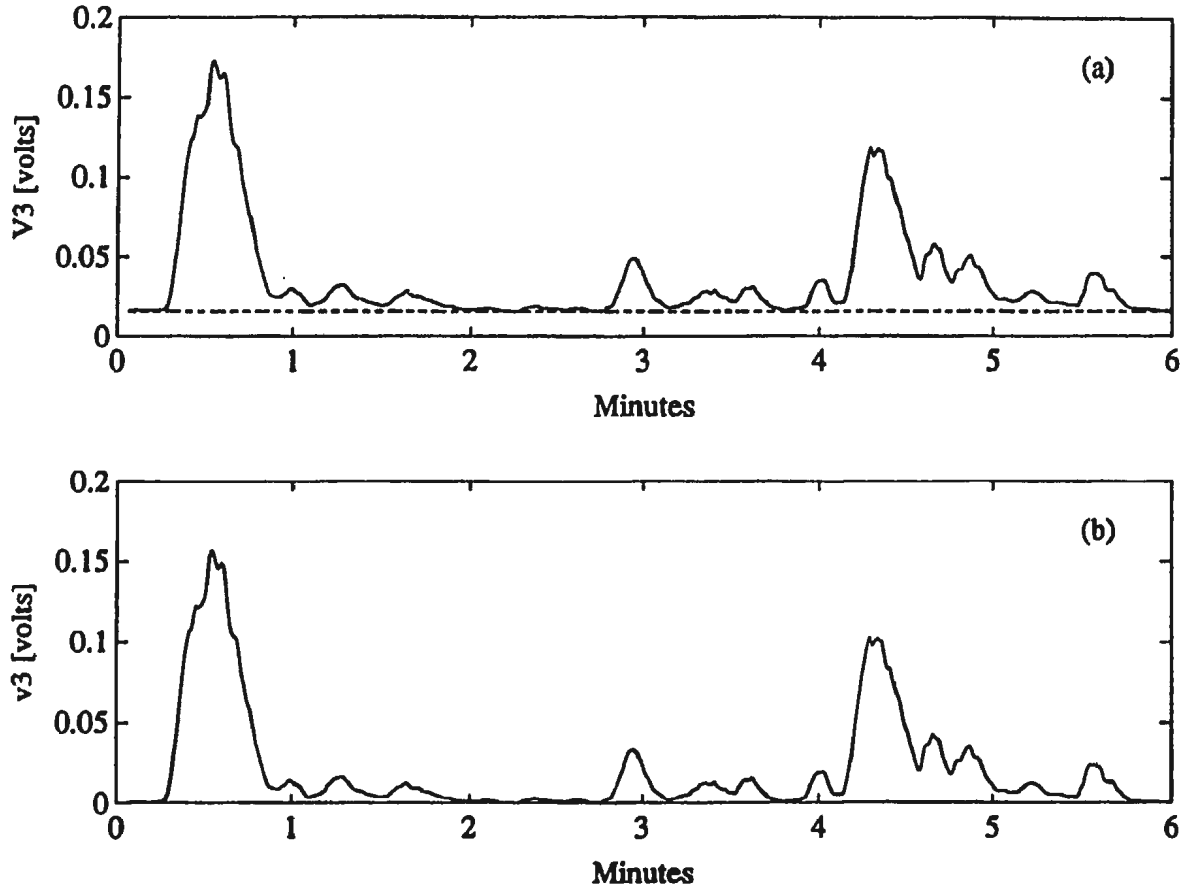

Figure 4.8: Time series from run 300.030 illustrating the voltages V_3, v_3, and $v_{B,3}$. (a) Time series of raw signal uncorrected for background, $v_{B,3}$. The dashed line indicates the background level. (b) Same as in (a) except $v_{B,3}$ has been subtracted.

simultaneously near the start and end of a suspension event. For this reason the ratios are most stable at the event's peak, when the total signal is much greater than the background. Because of the logarithms in Equation 4.14 linear changes in the amount of background signal subtracted lead to non-linear changes in the inverted concentration. A threshold voltage of 40 mV on v_N effectively solves the first of these problems. When the threshold is lower than this events spuriously appear in the reflection method results at times when significant suspension events do not exist.

A sample calculation illustrates directly the effects of removing background signal on the inverted mass concentration. Using total signal values at a specific time during an event, and uniformly varying the amount of background subtracted from zero to the full background level, a general relationship between the inverted concentration and the amount of background subtracted can be obtained, for that time. Such an example is provided in Figure 4.9. This example is computed for the 5 MHz inverted result in the third bin above the bottom, at time 0.5 minutes into run 300.030. Since most of the background levels are similar in magnitude, the ordinate axis shows only the variation of $v'_{B,3}$. The Figure shows that the inverted concentration increases as more of the background is subtracted. The increase in inverted concentration when the full background level is subtracted is approximately 20% more than without subtracting background levels.

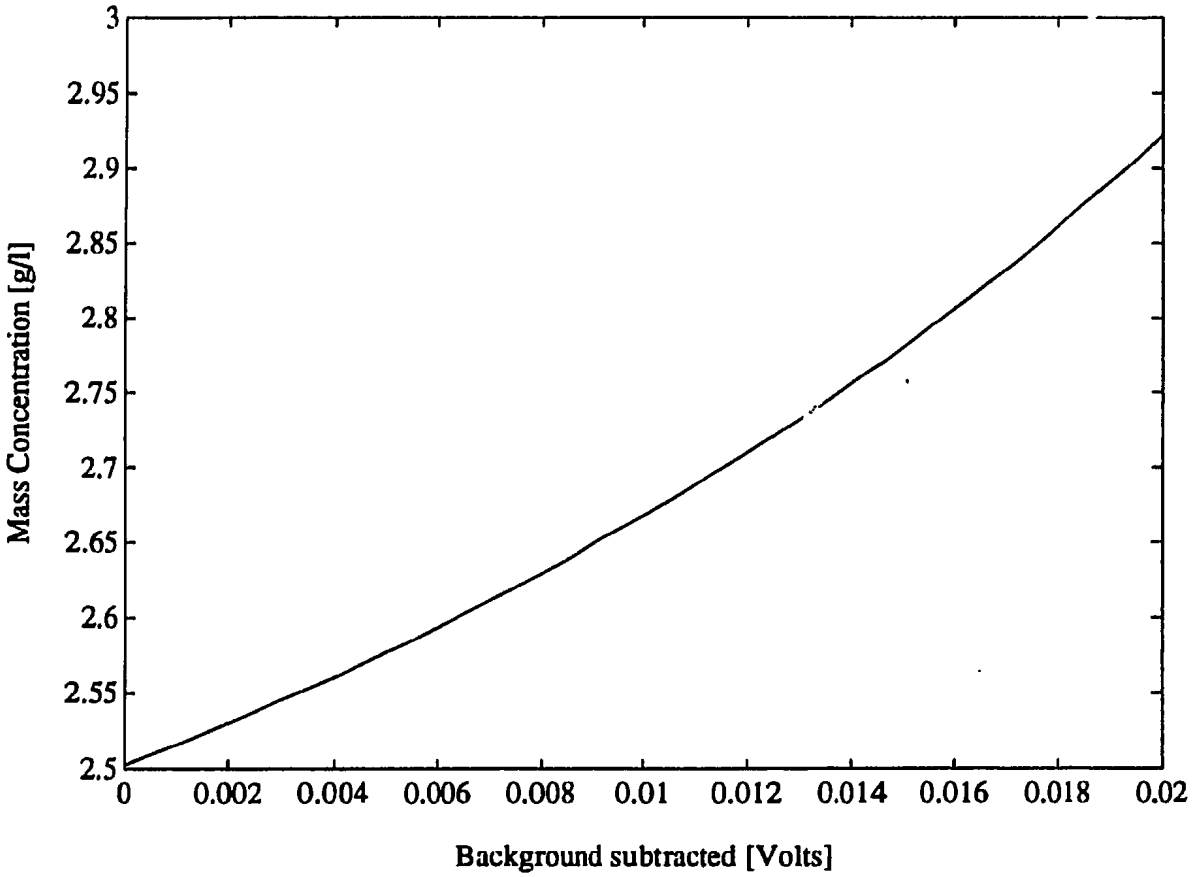

Figure 4.9: Variation in mass concentration ($\overline{M}_3$) at 5 MHz with amount of background signal subtracted for the first suspension event in run 300.030.

Chapter 5

Results

The inversion process described in Chapter 3 is employed to convert RASTRAN data collected at Stanhope Lane Beach during October–November 1989 to suspended sediment concentration. Concentrations obtained using the reflection method are compared with multifrequency and OBS methods to test whether the acoustic mirror is the consequence of coherent bottom reflection.

Results for two RASTRAN runs are presented. Section 5.1 presents results from run 300.030 for the 5 and 2.25 MHz sounders. Section 5.2 presents results from run 307.025 for the 5 MHz sounder, and describes a case for which the reflection method fails. Results are presented in the form of concentration time series derived from the reflection method, and are compared with the results of the multifrequency backscatter technique, and optical backscatter measurements.

Linear correlation coefficients, R_{zy}, and the mean relative difference, D_{zy}, are

provided in tables. The mean relative difference is given by,

$$D_{zy} = \frac{1}{I} \sum_{i=1}^{I} \frac{|y_i - z_i|}{y_i} \tag{5.1}$$

where I is the total number of data points in the plot used for calculation, y_i represents the measured value, and z_i is the calculated value. In cases where the correlation between the reflection method and either of the other methods appear significant or provides insight, the scatterplots are provided.

Because of a failed connector, only OBS data from the shoreward end of the instrument frame (Figure 3.3) are available. All OBS comparisons are made with the lowest of the 3 sensors, OBS 133. Although the height of the OBS detector above bottom is known for each data run, OBS instrument design imposes some limitations on interpretation of the recorded signal. The OBS beam pattern is about 30° full width horizontally, 50° vertically, and has a range not more than 20 cm (based on manufacturer's specifications) [Downing *et al.*, 1981]. Thus at 10 cm range the OBS beam interrogates a 9 cm high vertical section in the water column. Moreover, the detected volume decreases with increasing particle concentration, due to nearer particles shadowing further ones. OBS calibrations were performed utilising surficial sand obtained at the deployment site. Therefore, the OBS measurements assume that for all heights and times, suspended sediment sizes are the same.

Finally, all data has been identically filtered with a 6 second moving average removing fluctuations at and above the frequencies of the incident gravity waves.

5.1 Run 300.030

Figure 3.4 of Chapter 3 is reproduced in Figure 5.1 for convenience. At the top of this Figure the unfiltered cross shore current record is shown. At both 2.25 MHz and 5 MHz, two suspension events are seen in Figure 5.1, and each is strongly correlated with the passing of a well defined wave group. This is consistent with earlier observations [Hanes and Huntley, 1986; Hay *et al.*, 1988; Vincent and Green, 1990]. The OBS data at the top of this Figure indicate this as well. Event 1 starts at approximately 0.2 minutes into the run and ends at approximately 1 minute, or 48 s duration. Event 2 starts at approximately 4.2 minutes into the run and ends at approximately 4.8 minutes, or 36 s duration.

Figures 5.2(a) and (b) show the filtered direct backscatter and mirror image signals for the 5 MHz signal near the bottom, respectively. Time series in this figure are well correlated with each other in time and appear to be unaffected by the bottom echo. Furthermore, Figure 5.2 demonstrates the ability of the seabed to behave as a mirror since signal amplitudes decrease as one moves further from the seabed, for both the direct backscatter and mirror signals.

Field values of temperature and salinity collected at the shoreline for this particular run are 9° C and 29 ppt, respectively. These values yield a soundspeed of 1477 m/s [Clay and Medwin, 1977, p88], and a range resolution of $\Delta z = 1.846$ cm per range bin, and are also used to calculate the attenuation due to sea water. The

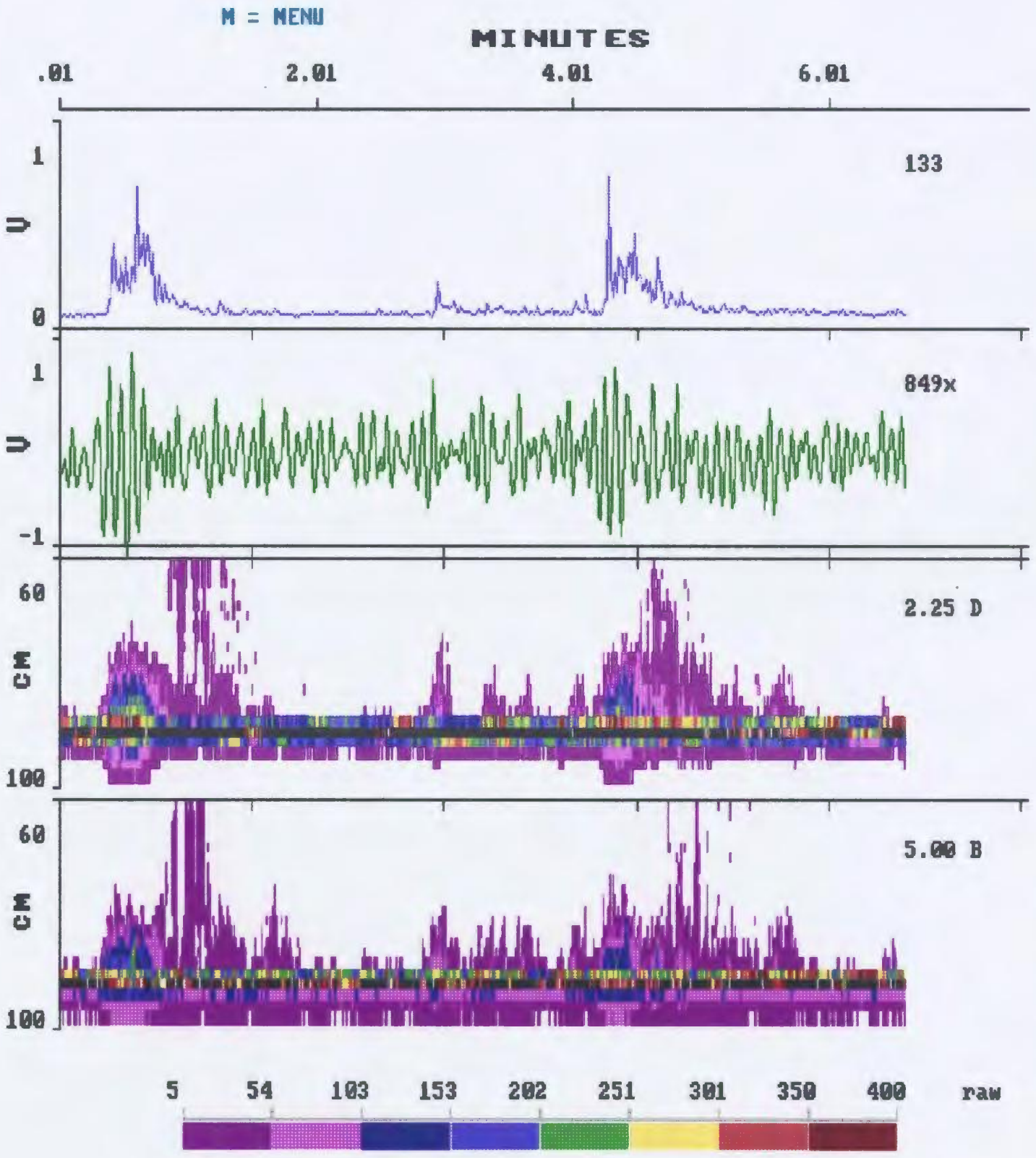

Figure 5.1: RASTRAN false colour plot for run 300.030.

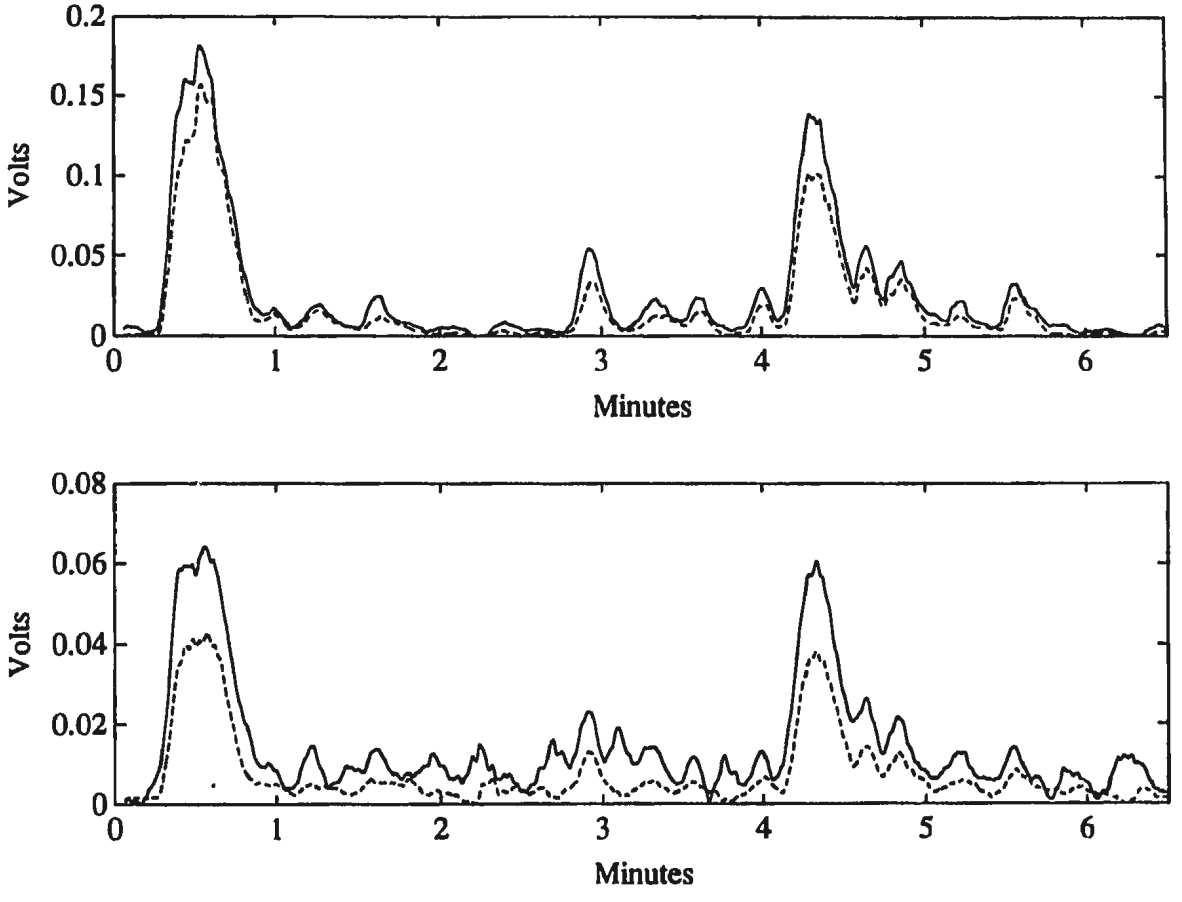

Figure 5.2: Filtered time series for run 300.030 at 5 MHz of: (a) direct backscatter voltages v_2 (—) and v_3 (- - -); (b) mirror image voltages v_2' (—) and v_3' (- - -).

range to the fluid-sediment interface was measured with a LeCroy model 9400 120 MHz digital oscilloscope to a resolution of 0.1 cm. The details of this procedure are described in Hay and Bowen [1993].

The file-averaged vertical size profile of Figure 4.5, obtained from the multifrequency inversion on run 300.030, is reproduced here for convenience in Figure 5.3. Data below 6 cm height provide input for particle radius in the High-pass model. Particle sizes from the multifrequency inversion at heights greater than 3 cm above the bottom have a mean diameter of about 180 μm, which is only 6% greater than the measured mean diameter of 170 μm near the RASTRAN frame. The particle size estimate nearest the bottom is considerably larger. This is the result of bottom echo contamination for the multifrequency inversion in this range bin.

5.1.1 Results at 5 MHz

For the 5 MHz transducer the range to bottom for this run was 94.3 cm, placing the bottom in the upper portion of the $52nd$ range bin. The observed position of the bottom echo in the RASTRAN acoustic data corroborates this result, so for this run squared-voltage ratios of mirror signal and direct backscatter signals are centred around the $52nd$ bin ($b = 52$). Hence, at 5 MHz three values, Γ_1, Γ_2, and Γ_3, are calculated, yielding two concentration estimates, $\overline{M}_2$ and $\overline{M}_3$, as functions of time. In a method described by Hay and Sheng [1992], the mean height of OBS 133 above bottom is determined to be 4.8 cm. The OBS values should therefore be compared

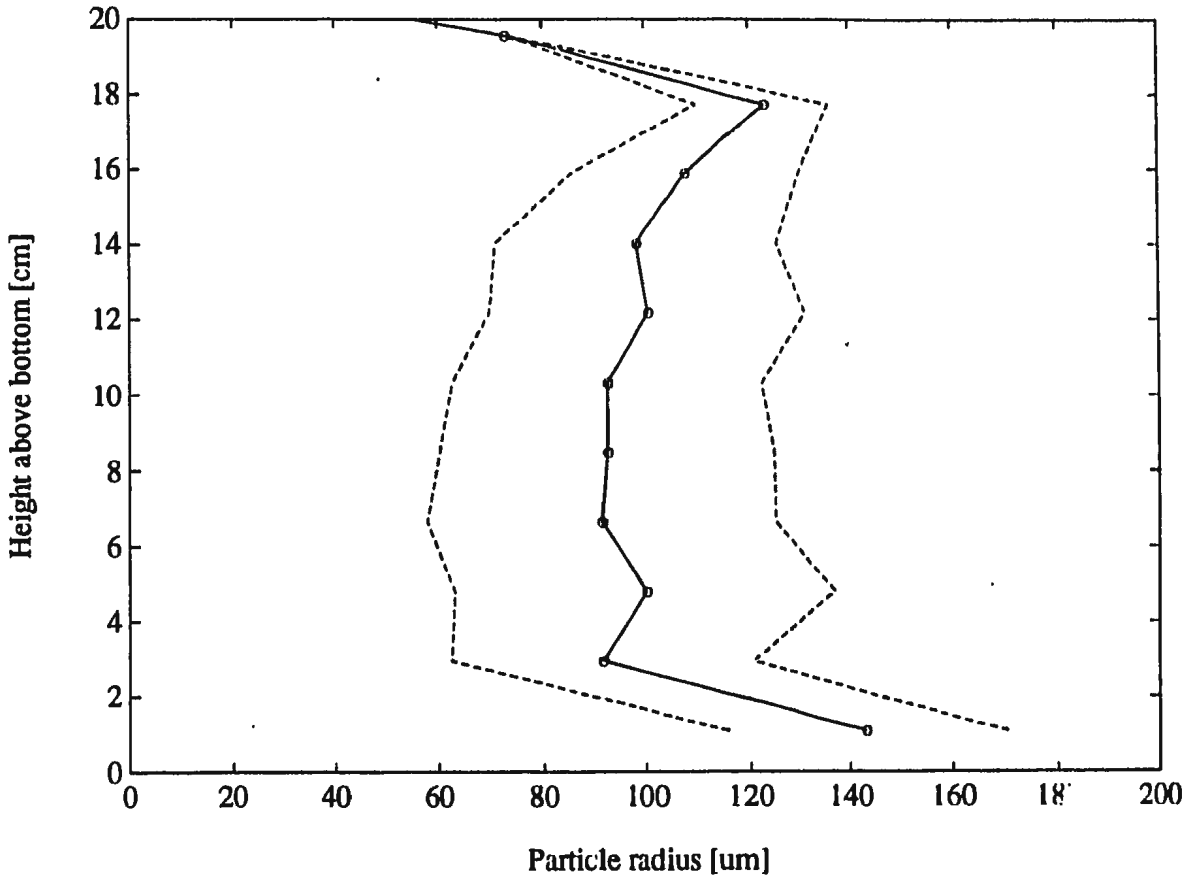

Figure 5.3: File-averaged vertical profile of particle size for run 300.030. The solid line (—) represents the mean, and the dashed lines (- - -) represent one standard deviation from the mean.

to those in the third range bin above the bottom for this sounder.

Time series of concentration for run 300.030 from the 2 inversion methods and OBS are presented in Figure 5.4 for comparison purposes. Values of $\overline{M}_2$ and $\overline{M}_3$ from the reflection method are illustrated in Figures 5.4(a) and 5.4(b), respectively. Values of M_3 from the multifrequency method and the OBS are illustrated in 5.4(c) and 5.4(d), respectively. For all reflection method time series the two solid lines represent $\overline{M}_N^{\pm}$, based on signal fluctuations, as described previously. Instances where an isolated point in time yielded a result, the confidence limits are indicated with circles (o). Times for which no reflection method result is shown (i.e. between the 2 events) indicate that this method has failed either because $v'_N/v_N \geq 1$, or v_N was less than the chosen threshold voltage, 40 mV. For the multifrequency backscatter results in 5.4(c) the two solid lines represent ± 1 standard deviation from the mean over 20 sets.

It is clear from Figures 5.4(a) and 5.4 (c) that the results of the reflection method and the multifrequency backscatter are consistent. Because $\overline{M}_2$ applies to the lower boundary of the second bin above the bottom bin, and M_3 (multifrequency method) applies to the centre of the third bin above the bottom bin, these two results are 1.5 bins apart vertically ($\simeq$ 2.8 cm), with the multifrequency bin being farther above bottom. Peak concentration values are higher for the reflection method than for the multifrequency method at similar times. This is an expected result because concentrations increase as one approaches the seabed.

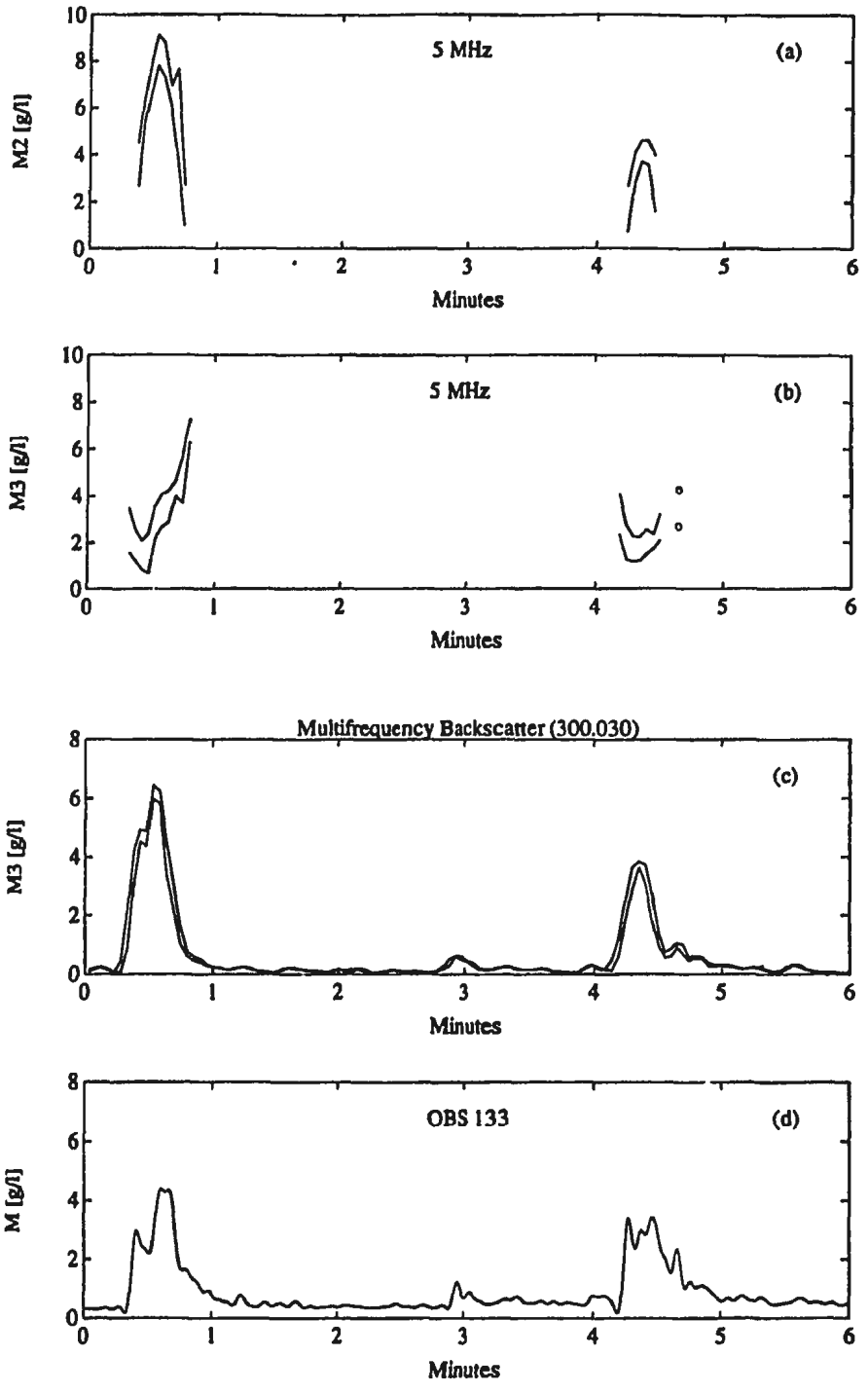

Figure 5.4: Reflection method sediment concentration at 5 MHz for run 300.030. Confidence limits (—) based on signal fluctuations are shown as functions of time. Illustrated are (a) reflection method $\overline{M}_2$, (b) reflection method $\overline{M}_3$, (c) multifrequency backscatter M_3, and (d) OBS 133.

Figures 5.4(b) and 5.4(d) illustrate two features: first, the reflection method predicts that concentration decreases as one increases the height above the seabed (compare with 5.4a); second, that at the centre of each event, when reflection method results are more reliable, the inverted concentrations agree well with the OBS measurement.

Figure 5.5 shows results similar to those in Figure 5.4 except that the upper and lower concentration estimates, $\overline{M}_N^+$ and $\overline{M}_N^-$, correspond to using $\overline{\langle a \rangle}_N^-$ and $\overline{\langle a \rangle}_N^+$ in Equation 3.19, respectively. The plots show that the concentration estimates at 5 MHz are rather insensitive to uncertainties in particle size, in accord with the analysis in Chapter 4. This is especially obvious in Figure 5.5(a) where the two lines defining the range of possible concentrations are barely discernible. It is less obvious in 5.5(b), but still noticeable. The larger difference in the possible range for $\overline{M}_s$ is due to a larger standard deviation in $\overline{\langle a \rangle}_N$ for that height.

For further comparison between the reflection method and the OBS, and multifrequency methods, a linear regression analysis was performed. A summary of these results is provided in Table 5.1. Note that linear regressions may not be the best indicator of the validity of the reflection method. Data can have nearly zero correlation but can be clustered near the 1:1 line, representing perfect agreement between the reflection method OBS/multifrequency techniques, which generally supports the reflection method.

Figures 5.6(a) through (d) show scatterplots where the linear correlation between

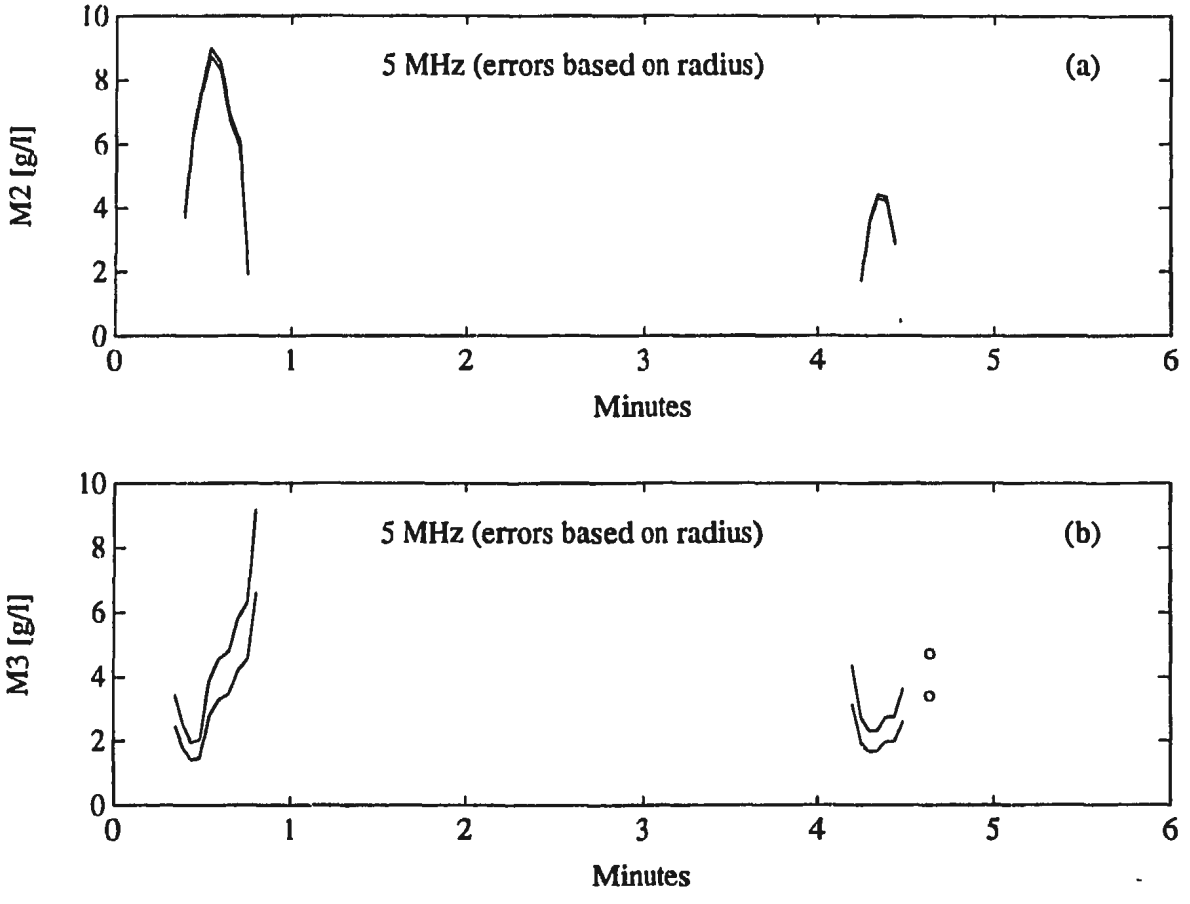

Figure 5.5: Run 300.030 time series of inverted concentration from single frequency reflection at 5 MHz, where the confidence limits (—) are based on the possible range of particle radii.

reflection estimates of $\overline{M}_2$, OBS 133, and multifrequency methods appear significant. The dashed line in these figures represents the semi-major axis of the ellipse best confining the data. One observes in Figures 5.6(a) through (d) that the slope of the regression line is consistently less than unity. The results of Crawford and Hay [1993] suggest that the ratio algorithm employed for the multifrequency inversion yields concentration estimates which can be low by as much as a factor of 2. This could explain the low slope in the scatterplots. Similarly, Figures 5.7(a) and (b) show the correlation between the reflection method estimates of $\overline{M}_3$ and OBS and multifrequency methods, respectively. In general, the correlations for $\overline{M}_3$ are not as good, and the reasons for this are not entirely clear.

Reflection Method	OBS 133	Multifrequency Backscatter				
		M_1	M_2	M_3	M_4	M_5
$\overline{M}_2$	0.43 † (0.78)	-0.71 (0.82)	0.20 (0.79)	0.89 † (0.36)	0.94 † (1.5)	0.90 † (5.4)
$\overline{M}_3$	0.58* † (0.28)	0.45 (0.89)	0.18 (0.86)	-0.25* (0.76)	0.27* (0.41)	0.21* (2.6)

Table 5.1: Results at 5 MHz for run 300.030. Values for the linear regression coefficient, R_{zy}; values of D_{zy} are in parentheses. The asterisk indicates that outliers have been disregarded in calculating the estimate. † denotes that the scatterplot is provided.

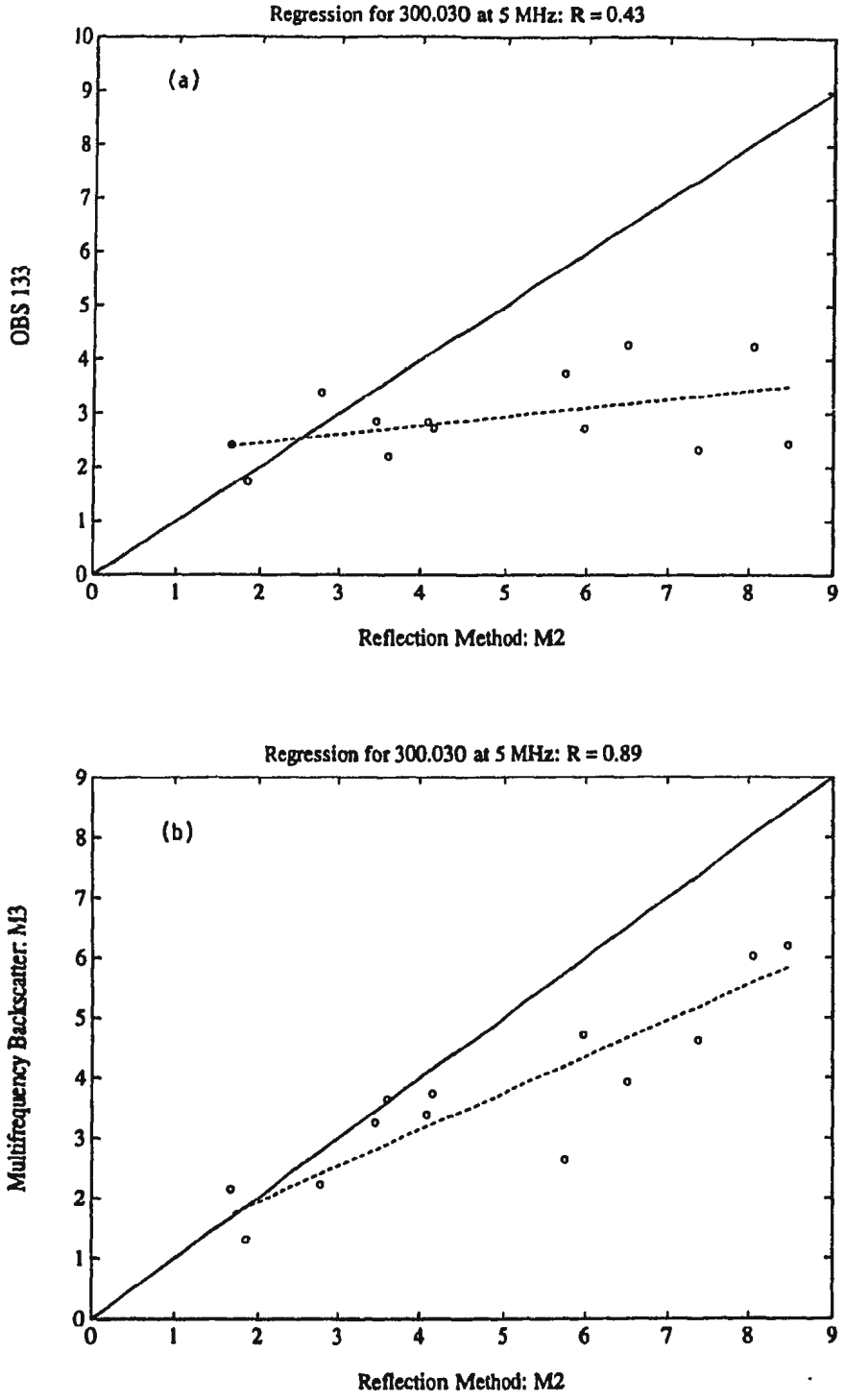

Figure 5.6: Scatterplots for run 300.030 showing comparison of $\overline{M}_2$ at 5 MHz with (a) OBS, (b) M_3, (c) M_4, and (d) M_5, from the multifrequency backscatter inversion.

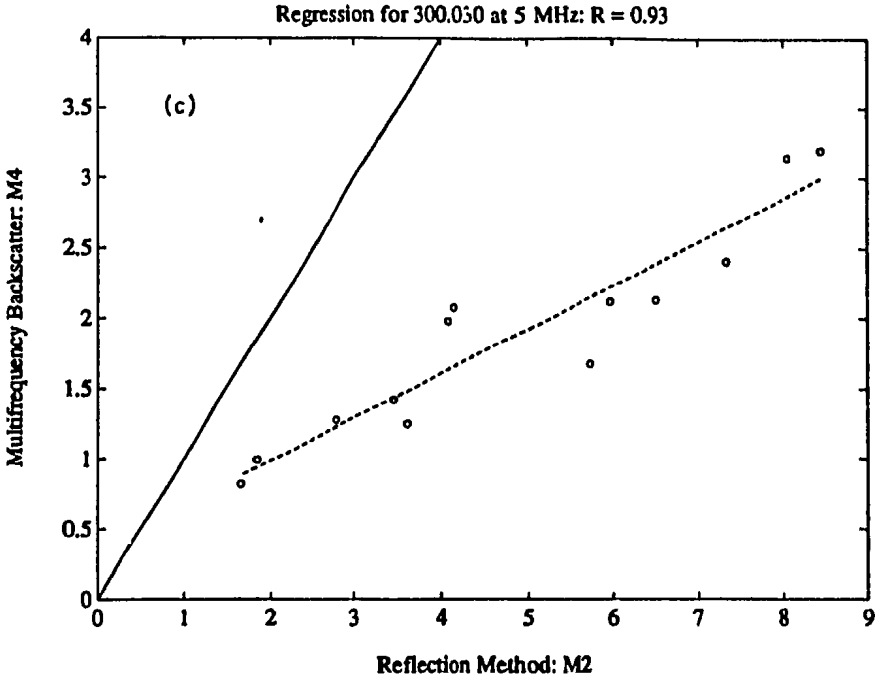

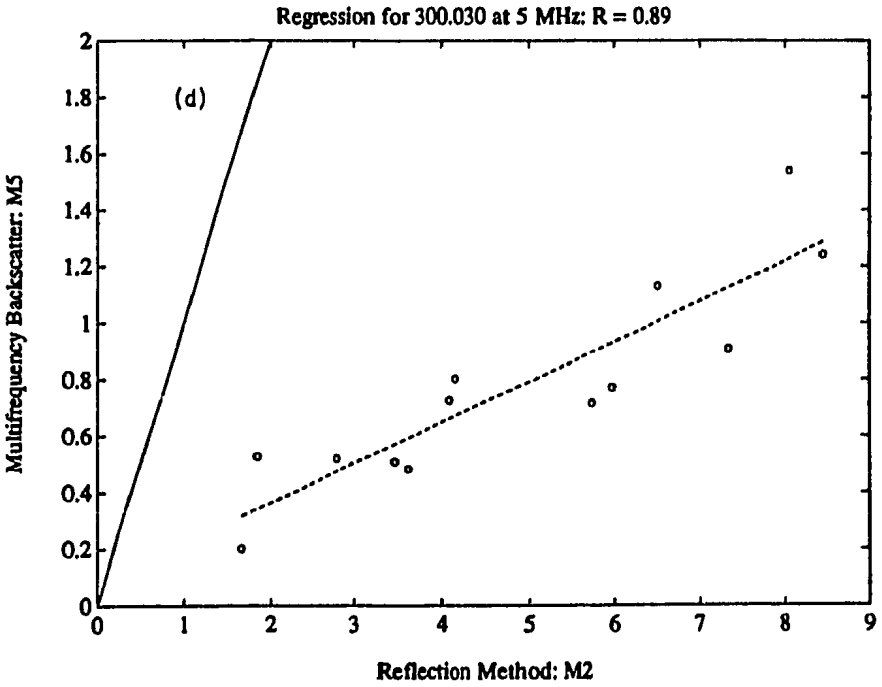

5.6 (continued)

The multifrequency backscatter inversion employs three transceivers with non-overlapping beams, one of which was a different height above the bottom. This leads to an uncertainty with respect to absolute height above the bottom for final concentration estimates since range to bottom evolves in time and space. Thus, it is plausible that the multifrequency result M_3 lies *closer* to the bottom than expected, yielding a higher correlation with $\overline{M}_2$ than with $\overline{M}_3$. The correlation is expected to be good between $\overline{M}_3$ and the OBS, since the height of the OBS places the centre of it beam nearer to the third bin above the bottom. Indeed the best correlation of 0.58 is between $\overline{M}_3$ and the OBS, shown in Figure 5.7, but could only be obtained by disregarding data for which the OBS measurements were less than 2 g/ℓ in Figure 5.4(d). This may indicate a susceptibility of the reflection method in coping with low concentrations, since signal levels are nearer to the chosen threshold, and are more prone to a lower S/N ratio.

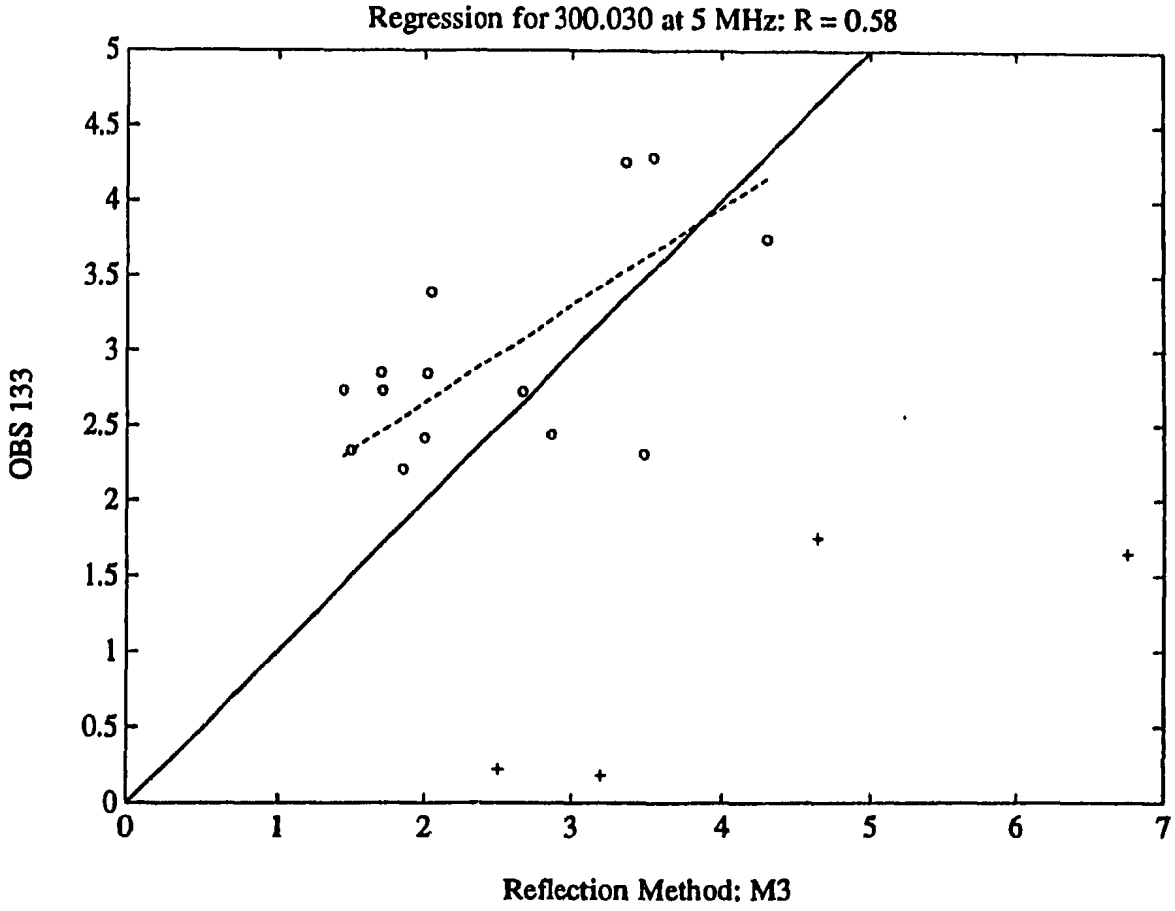

Figure 5.7: Scatterplot for run 300.030 showing comparison of $\overline{M}_3$ at 5 MHz with OBS 133 (points omitted from the calculation of R_{zy} and D_{zy} considered outliers are denoted by '+' as explained in the text).

5.1.2 Results at 2.25 MHz

For the shoreward 2.25 MHz transducer (2D), the range to bottom is 92.6 cm, placing the fluid-sediment interface near the top of the 51*st* range bin ($b = 51$). This is confirmed in the data and results in 4 values, $\Gamma_1 \cdots \Gamma_4$, and thus three concentration estimates, $\overline{M}_2$, $\overline{M}_3$, and $\overline{M}_4$, as functions of time. The mean height of OBS 133 above bottom at the nearshore end of the instrument frame is 3.1 cm, placing it within the second range bin above the bottom.

Time series of concentration for run 300.030 at 2.25 MHz from the reflection method, where the confidence limits are based on signal fluctuations, are presented in Figure 5.8. OBS and multifrequency results are the same as shown in the 5 MHz case. Although it is seen in this figure that the concentration decreases as one moves away from the seabed, the most striking feature of the inverted results are the large concentration estimates, even at the lower bound. Possible reasons for this are reserved for discussion later in this section.

Similar to the 5 MHz case, the inversion was run again at 2.25 MHz but the confidence limits were based on the possible range of particle radii. Figure 5.9 shows these results. The upper and lower solid lines correspond to using $\overline{\langle a \rangle}_N^-$ and $\overline{\langle a \rangle}_N^+$ in the inversion, respectively. The dashed line indicates the inverted result from using the mean radius, $\overline{\langle a \rangle}_N$. From these computations one can see that the method at 2.25 MHz is far more susceptible to uncertainties in particle radius than to signal

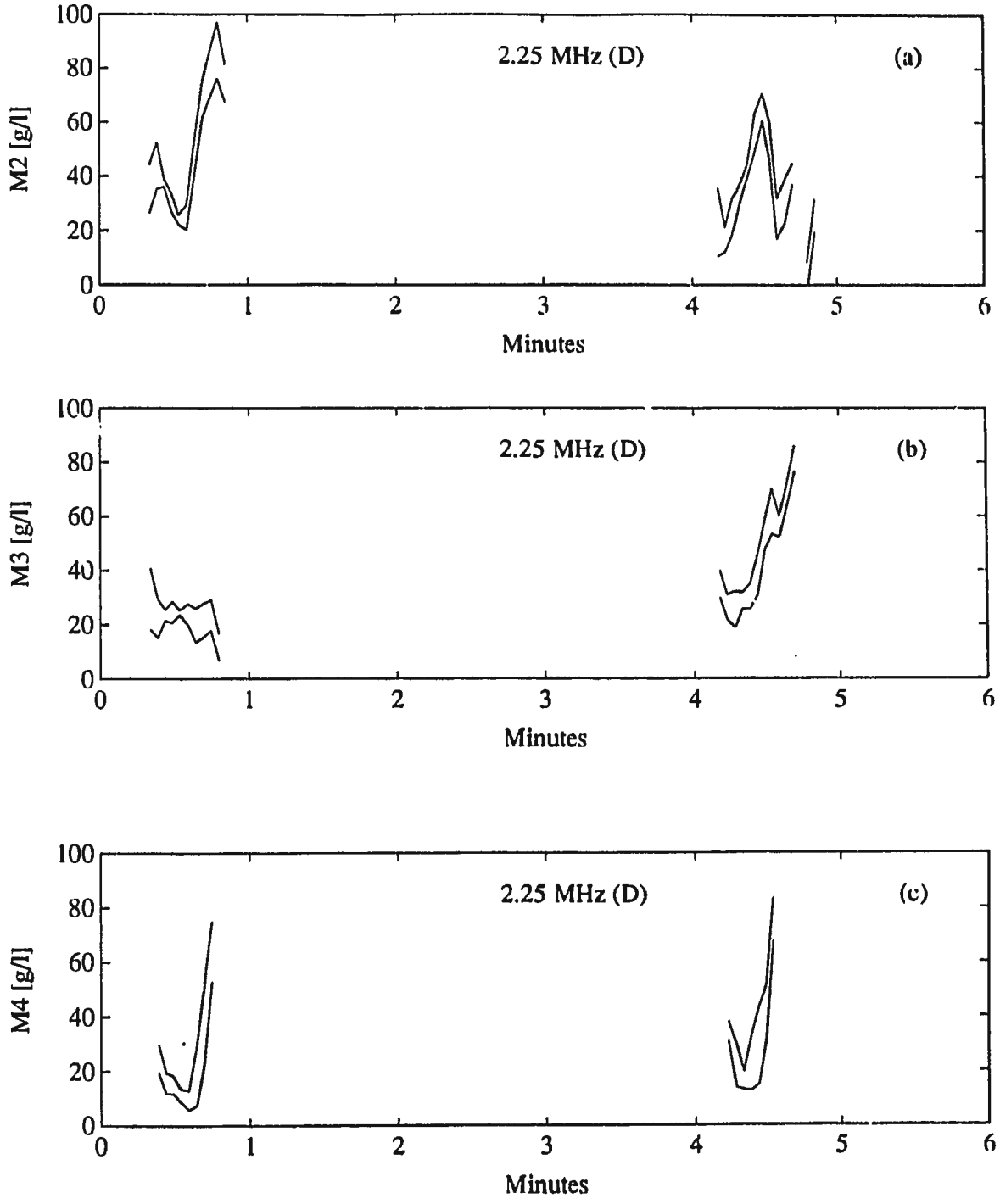

Figure 5.8: Reflection method results at 2.25 MHz for run 300.030. Confidence limits (—) are based on signal fluctuations.

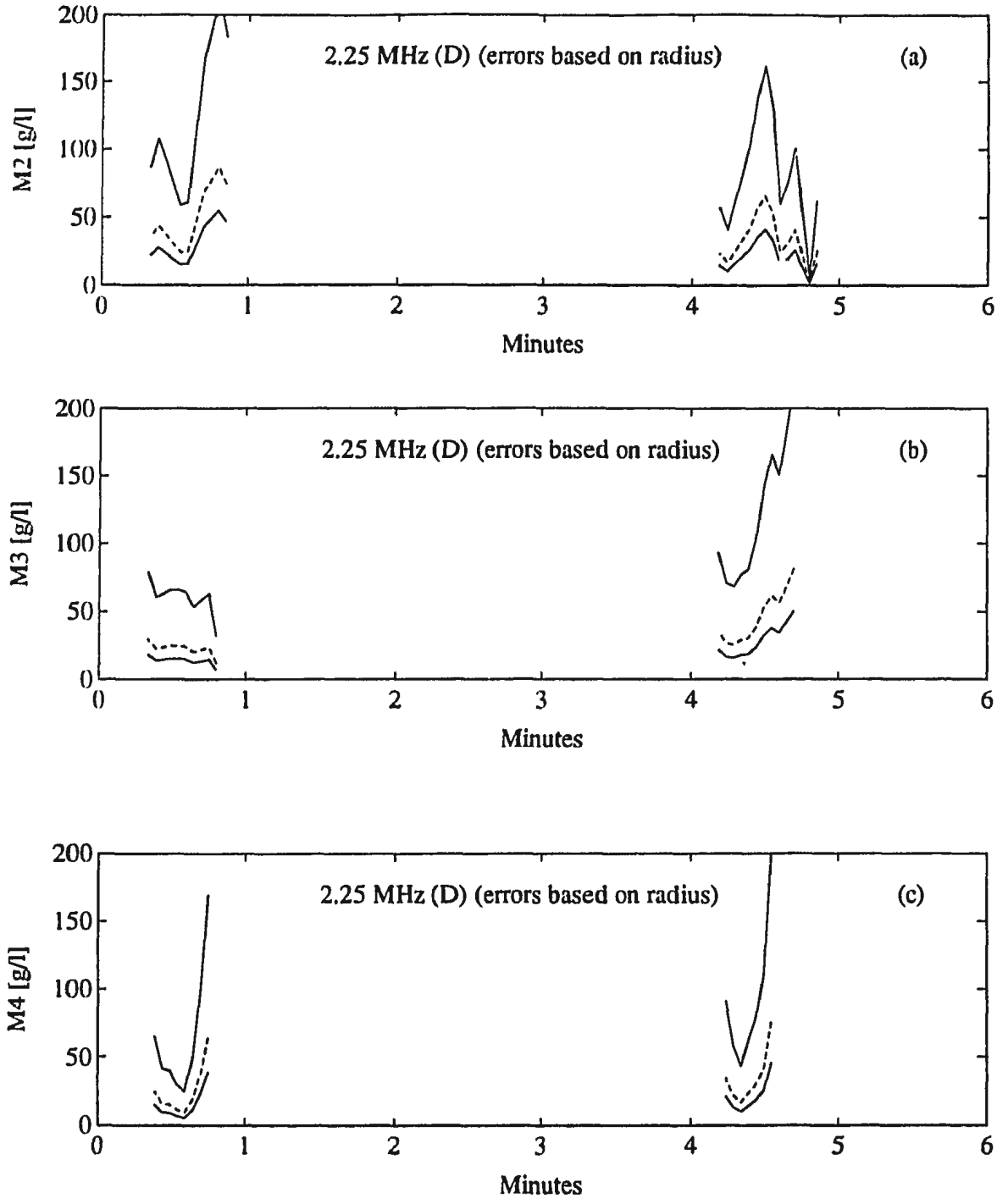

Figure 5.9: Reflection method results at 2.25 MHz for run 300.030. The mean inverted concentration (- - -) and confidence limits (—), based on the possible range of particle radii, are shown as functions of time. Upper solid lines correspond to using $\langle a \rangle^-$, lower solid lines to using $\langle a \rangle^+$.

fluctuations, indicated by the increased spacing of the confidence limits. This is especially true for the case of using the smaller radius estimate, $\overline{\langle a \rangle_N}^{-}$. Again, even at the lower bound (larger particles) inverted concentrations seem quite high compared to all other results, regardless of method.

Reflection Method	OBS 133	Multifrequency Backscatter				
		M_1	M_2	M_3	M_4	M_5
$\overline{M}_2$	0.22* (13)	0.29 † (0.70)	0.06* (0.93)	-0.21 (35)	-0.17 (61)	-0.13 (110)
$\overline{M}_3$	-0.42* (11)	0.16* † (0.89)	0.23* † (0.90)	-0.55 (26)	-0.49 (44)	-0.31 (88)
$\overline{M}_4$	-0.46 (11)	0.24 (0.51)	-0.39 (1.2)	-0.87 (18)	-0.79 (28)	-0.61 (57)

Table 5.2: Results at 2.25 MHz (2D) for run 300.030. Values for the linear regression coefficient, R_{zy}; values of D_{zy} are in parentheses. † denotes that the scatterplot is provided.

As before, a regression analysis was performed. The results of this analysis are summarised in Table 5.2. In general, the linear correspondence between the reflection method and the other methods is either low, or negatively correlated. Three scatterplots are provided in Figures 5.10(a), (b), and (c) for a comparison of $\overline{M}_2$ with M_1, $\overline{M}_3$ with M_1, and $\overline{M}_3$ with M_2 respectivley. The results shown in Figure 5.10 exhibit only small positive correlation after removing outliers from the computation, which are mostly from inverted data at the beginning and end of events where results are less stable. However, all of these plots exhibit a relatively dense cluster of points near the 1:1 line. This indicates that on average the two methods yield similar values of concentration in this example, and thereby support the reflection method.

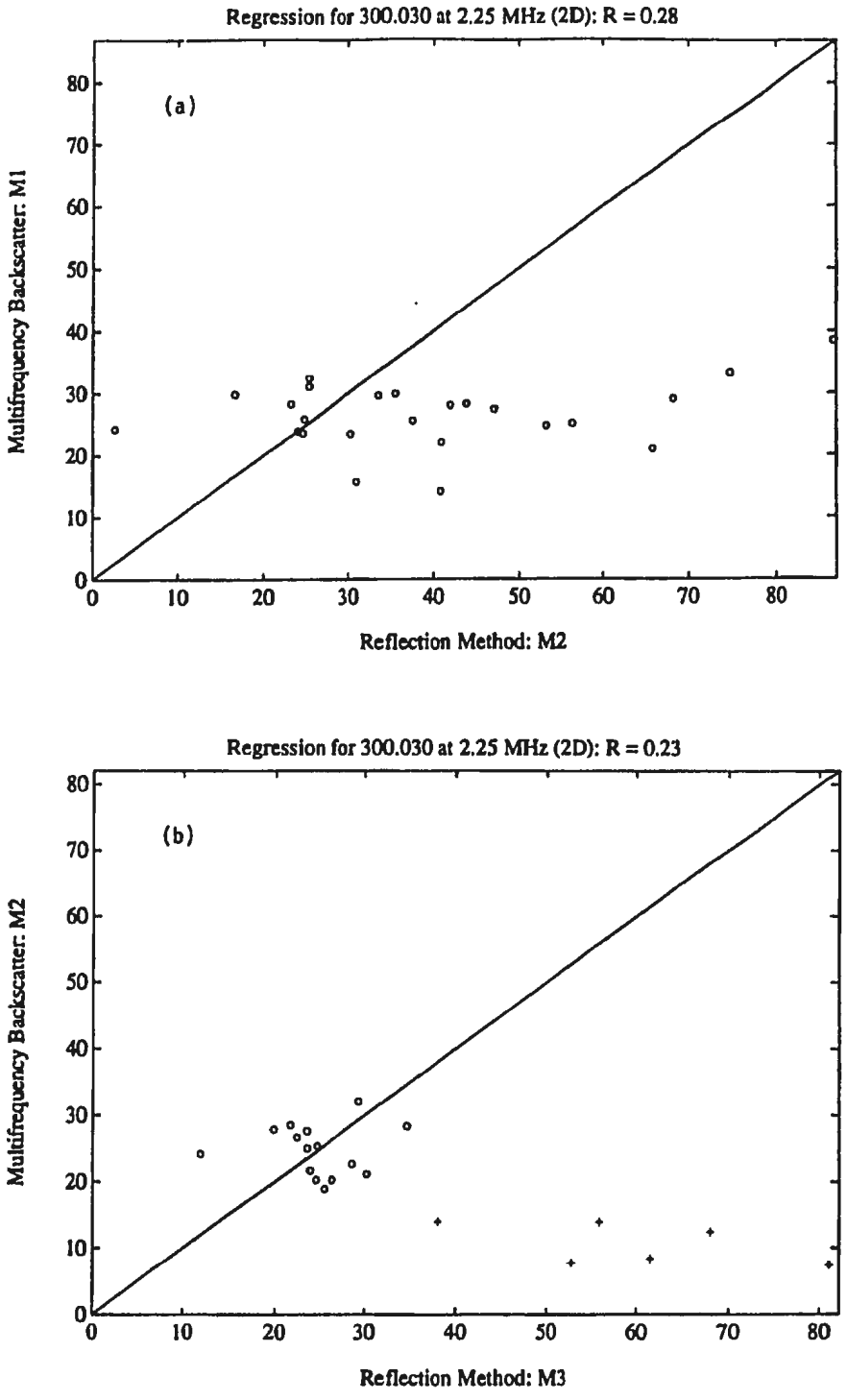

Figure 5.10: Scatterplots for run 300.030 at 2.25 MHz (2D) comparing (a) $\overline{M}_2$ with M_1, (b) $\overline{M}_3$ with M_2, and (c) $\overline{M}_3$ with M_1, respectively (points omitted from the calculation of R_{zy} and D_{zy} considered outliers are denoted by '+' as explained in the text).

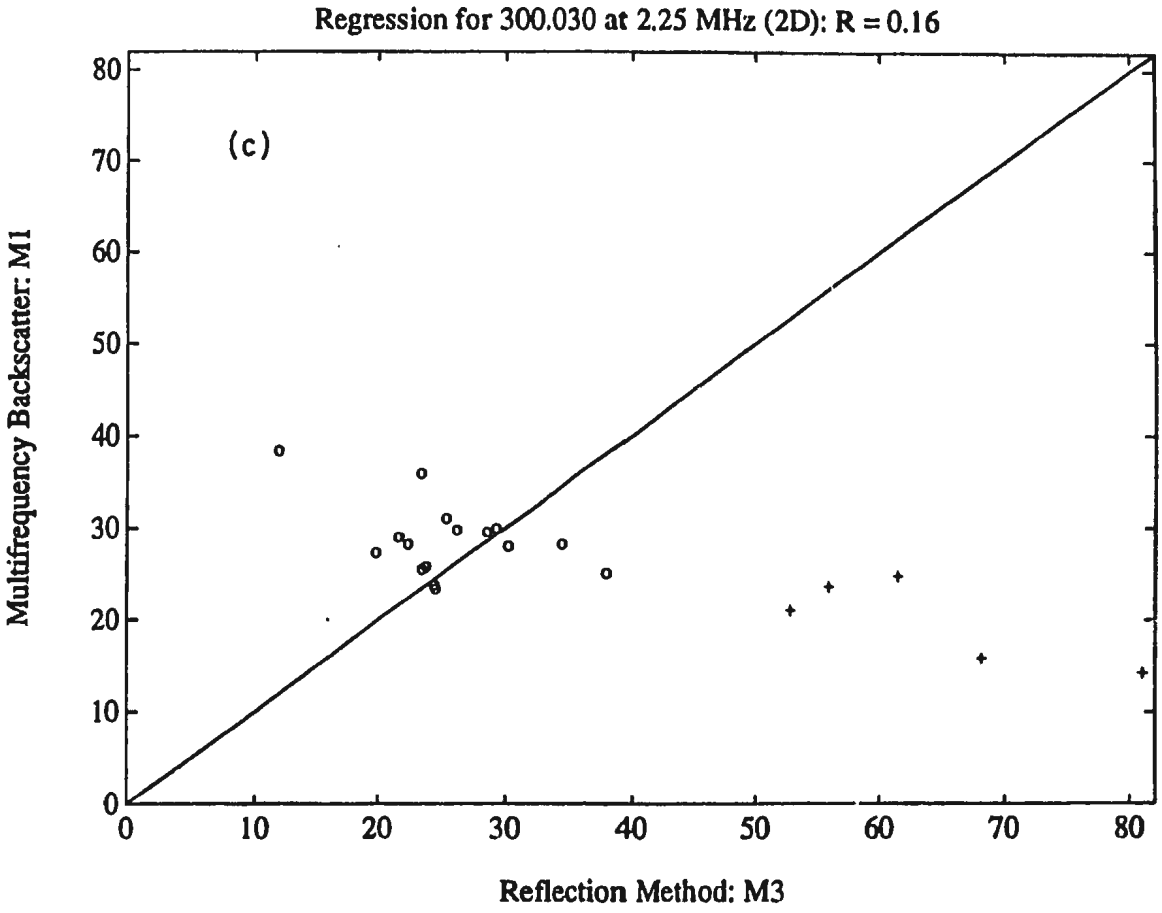

5.10 (continued)

The results in Figure 5.9 demonstrate that the distribution of particle sizes cannot explain the discrepancy between the reflection method results at 2.25 MHz and the multifrequency results. Other possible explanations are now discussed. For the reflection method the inverted concentration is a function of the scattering attenuation, α_s, thus abnormally high computed concentrations indicate that the computed values of α_s are anomalously high. It has been shown previously [Varadan *et al.*, 1983] that the single-scattering assumption may be violated if the concentration of suspended particles is greater than 1% by volume, corresponding to a limit of about 30 g/ℓ for quartz sand, and beyond this value the scattering attenuation decreases. Measurements on real sand [Hay, 1991] have confirmed the linearity up to approximately 1% by volume. Since the theory employed assumes single-scattering, and the computed scattering attenuation is too high it follows that multiple scattering is not the mechanism for the discrepancy. This suggests that the problem may lie in the inversion algorithm near frequencies of 2.25 MHz, more generally near frequencies for which the dimensionless size parameter $x \simeq 1$.

One must consider the accuracy of the High-pass model, when compared to measured values of $\overline{a}\alpha_s/\epsilon$, where $\overline{a}$ is the mean particle radius. The measured values from experiments by Jansen [1978; 1979] and Schaafsma and der Kinderen [1986], are summarised in Table II of Sheng and Hay [1988]. While the mean percentage difference between the High-pass model and the measured values is of order 15% for values of $x \leq 2$, individual measurements can have up to 30% discrepancy, usually

corresponding to the High-pass model overestimating $\bar{a}\alpha_s/\epsilon$. For $x \approx 1$, the measurements are split as to whether or not the High-pass model over- or underestimates the measurements. Recently, it has been shown [personal communication from Dr. A. E. Hay, Memorial University of Newfoundland] that the High-pass model is inaccurate, and that a modified theory is forthcoming. This will also require modification of the multifrequency results, which make use of the High-pass model.

Another possible explanation for the discrepancy at 2.25 MHz exists, however. This is the contribution from non-specular reflection, and is discussed in Chapter 6.

5.2 Run 307.025

In addition to presenting the 5 MHz results this section discusses the susceptibility of the $\overline{M}_2$ estimate to contamination in Γ_1 from the bottom echo. This section will omit much of the discussion provided in the previous section, as it is equally applicable.

Figure 5.11 shows the RASTRAN false-colour image for run 307.025, corresponding to the $25th$ run collected on November 3, 1989. Five major suspension events, centered near 0.2, 1.7, 2.8, 4.5, and 6.1 minutes, respectively, are most easily seen in the OBS signal of this Figure, and are concurrent with the acoustic data shown below that.

Figures 5.12(a) and (b) show the filtered direct backscatter and mirror image

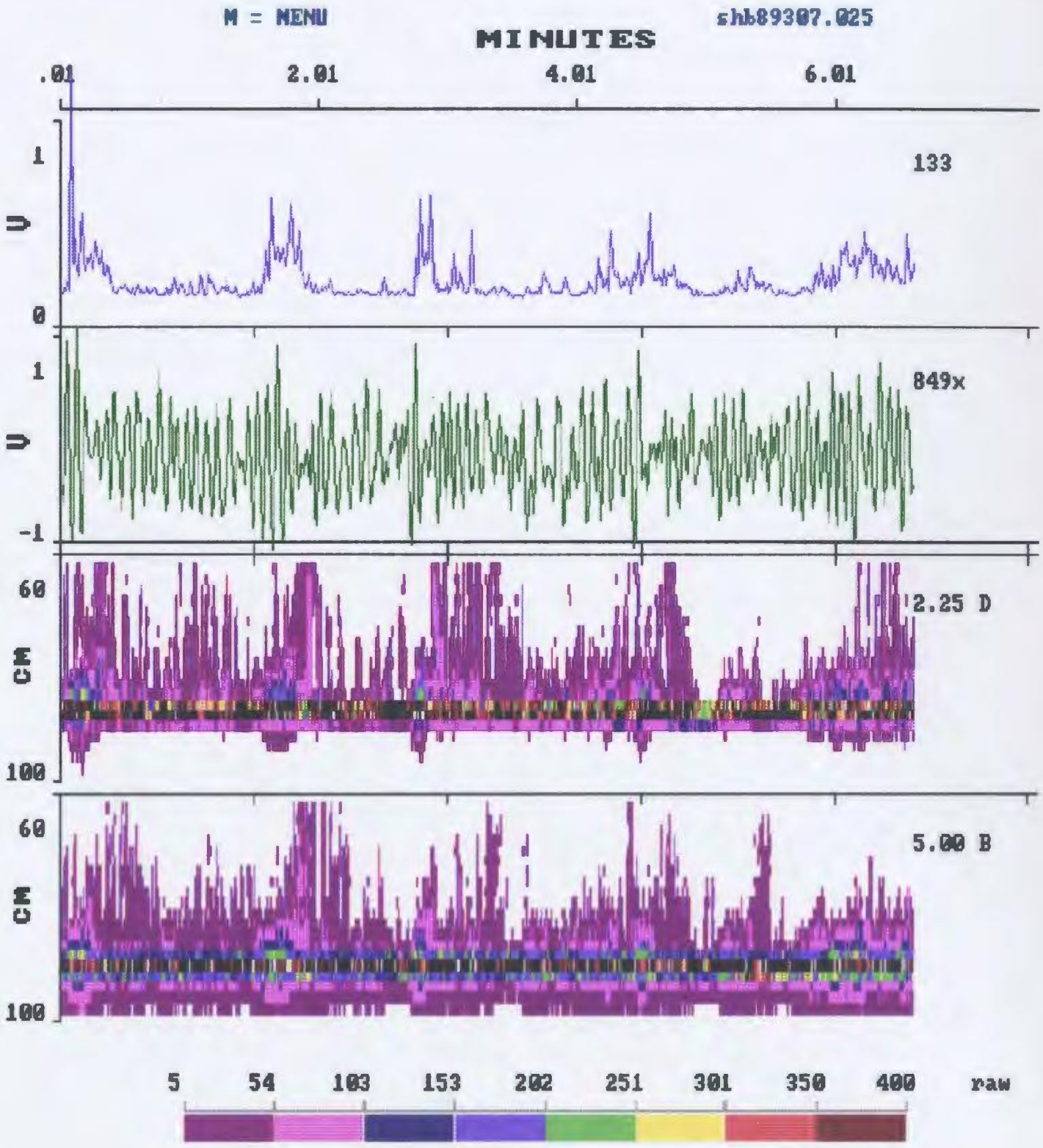

Figure 5.11: RASTRAN false colour plot for run 307.025.

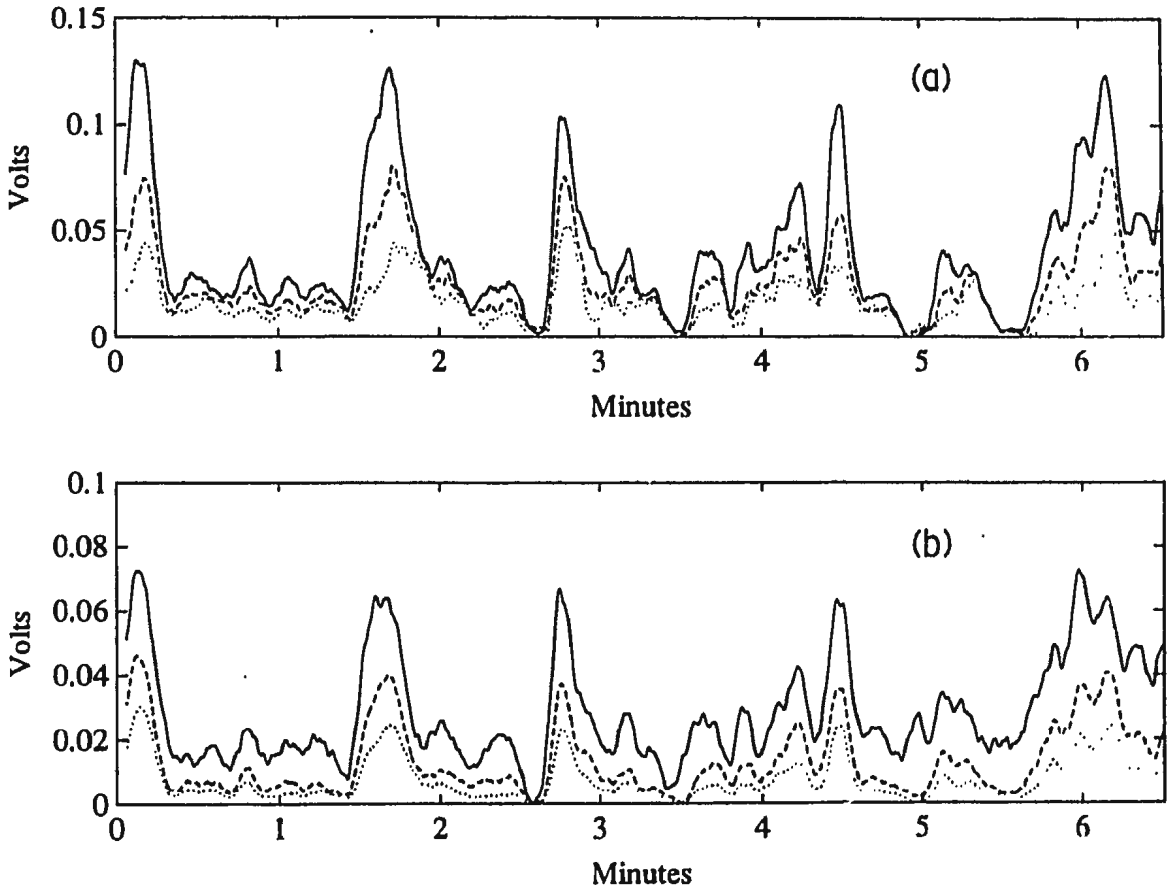

Figure 5.12: Filtered time series for run 307.025 at 5 MHz of: (a) direct backscatter voltages v_2 (—), v_3 (- - -), and v_4 (·····); (b) mirror image voltages v_2' (—), v_3' (- - -), and v_4' (·····).

signals for the 5 MHz signal, respectively. The same commentary applies to this Figure as for Figure 5.2 .

Field values of temperature and salinity collected at the shoreline for this particular run are 9.13°C and 29 ppt, respectively. These values yield a soundspeed of 1479 m/s, and a range resolution of $\Delta z = 1.849$ cm per range bin. The file-averaged vertical size profile for this run is provided in Figure 5.13. For this file data from the bottom 10 cm of this profile are used as input to the High-pass model.

5.2.1 Results at 5 MHz

For the 5 MHz transducer the range to bottom for this run was 93.2 cm, placing the bottom in the upper portion of the 51*st* range bin. This is supported by the bottom echo in the RASTRAN acoustic data, so for this run squared-voltage ratios of mirror signal and direct backscatter signals are centred around the 51*st* bin ($b = 51$), yielding four values, $\Gamma_1 \cdots \Gamma_4$, and three concentration estimates, $\overline{M}_2$, $\overline{M}_3$ and $\overline{M}_4$, as functions of time. The mean height of OBS 133 above bottom is 2.4 cm, which is within the second range bin above the bottom for this sounder.

Time series of inverted concentration for run 307.025 from the two inversion methods and OBS are illustrated with identical scaling in Figure 5.14 for comparison purposes. Inverted concentrations for $\overline{M}_2$ and $\overline{M}_3$ from the reflection method are shown in Figures 5.14(a) and 5.14(b), respectively. Figure 5.14(c) shows concentrations for M_2, M_3, and M_4 obtained from the multifrequency backscatter method. The standard

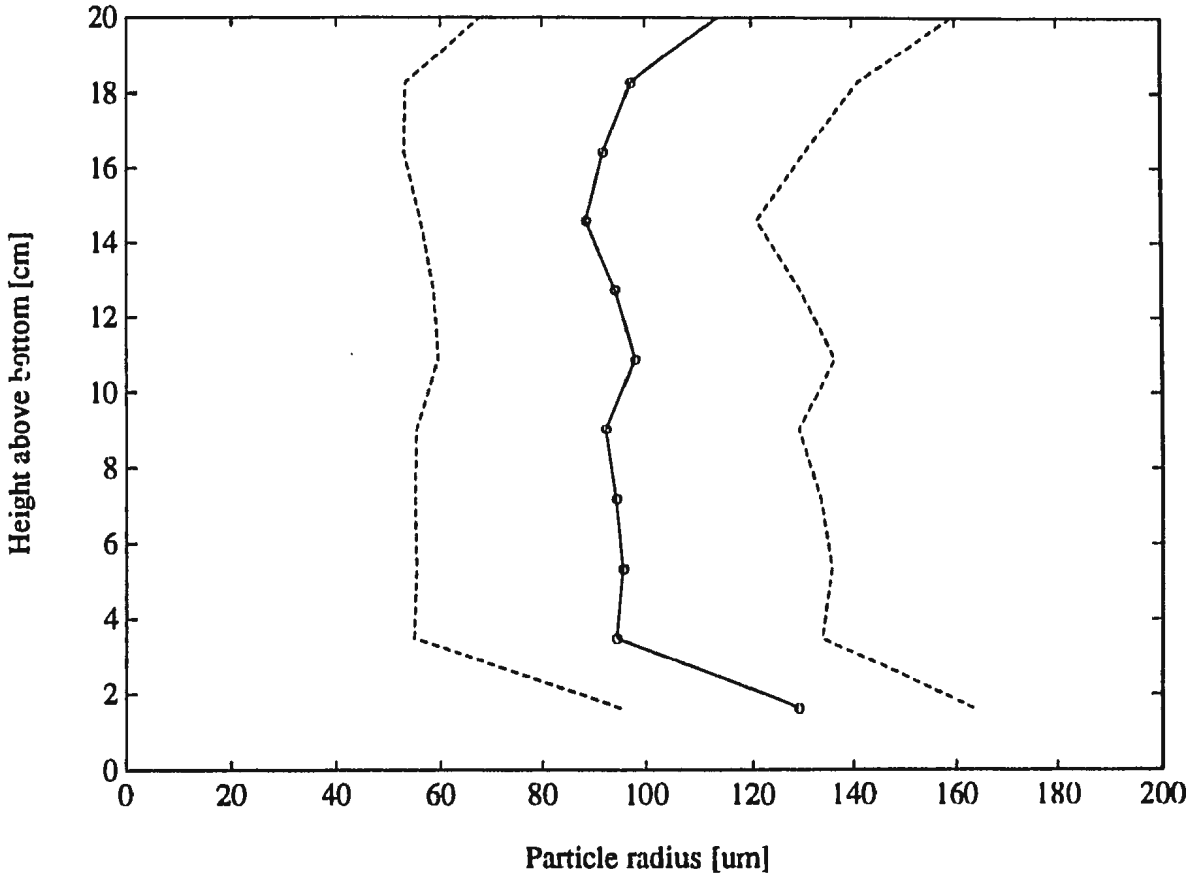

Figure 5.13: File-averaged vertical profile of particle size for run 307.025. The solid line (—) represents the mean, and the dashed lines (- - -) represent one standard deviation from the mean.

deviations on the results in Figure 5.14(c) are omitted, but are similar in magnitude to the standard deviations in the multifrequency results for run 300.030. As before, for reflection method time series in Figure 5.14 the two solid lines, and circles (o), represent $\overline{M}_N^{\pm}$, based on signal fluctuations. The OBS, and reflection method result for $\overline{M}_4$, are denoted by the solid and dashed lines, respectively, in Figure 5.14(d).

Overall, the three different methods have produced concentrations of the same order, and the reflection method has registered the five major events. One observes in Figure 5.14(c) that concentrations decrease further from the seabed. It is not clear from Figures 5.14(a) and 5.14(b) that the concentration decreases further from the seabed, except possibly for the events near 0.2 and 4.5 minutes respectively. The reflection method has failed in its estimates of $\overline{M}_2$ and $\overline{M}_3$ during the second event, centered at 1.7 minutes, since both the multifrequency result and OBS easily register the peak of this event. This failure of the reflection method during the second event is discussed later.

Figure 5.15 shows results similar to those in Figure 5.14 except that the upper and lower concentration estimates, $\overline{M}_N^{+}$ and $\overline{M}_N^{-}$, correspond to using $\overline{\langle a \rangle}_N^{-}$ and $\overline{\langle a \rangle}_N^{+}$ in Equation 3.19, respectively. Once more the uncertainties in inverted concentration at 5 MHz is due primarily to signal fluctuations, rather than uncertainties in particle size. Note however that $\overline{M}_3^{+}$ and $\overline{M}_4^{+}$ concentrations are slightly higher than the upper concentration bound due to signal fluctuations. This slight increase in inverted concentration is due to the use of the smaller particle size.

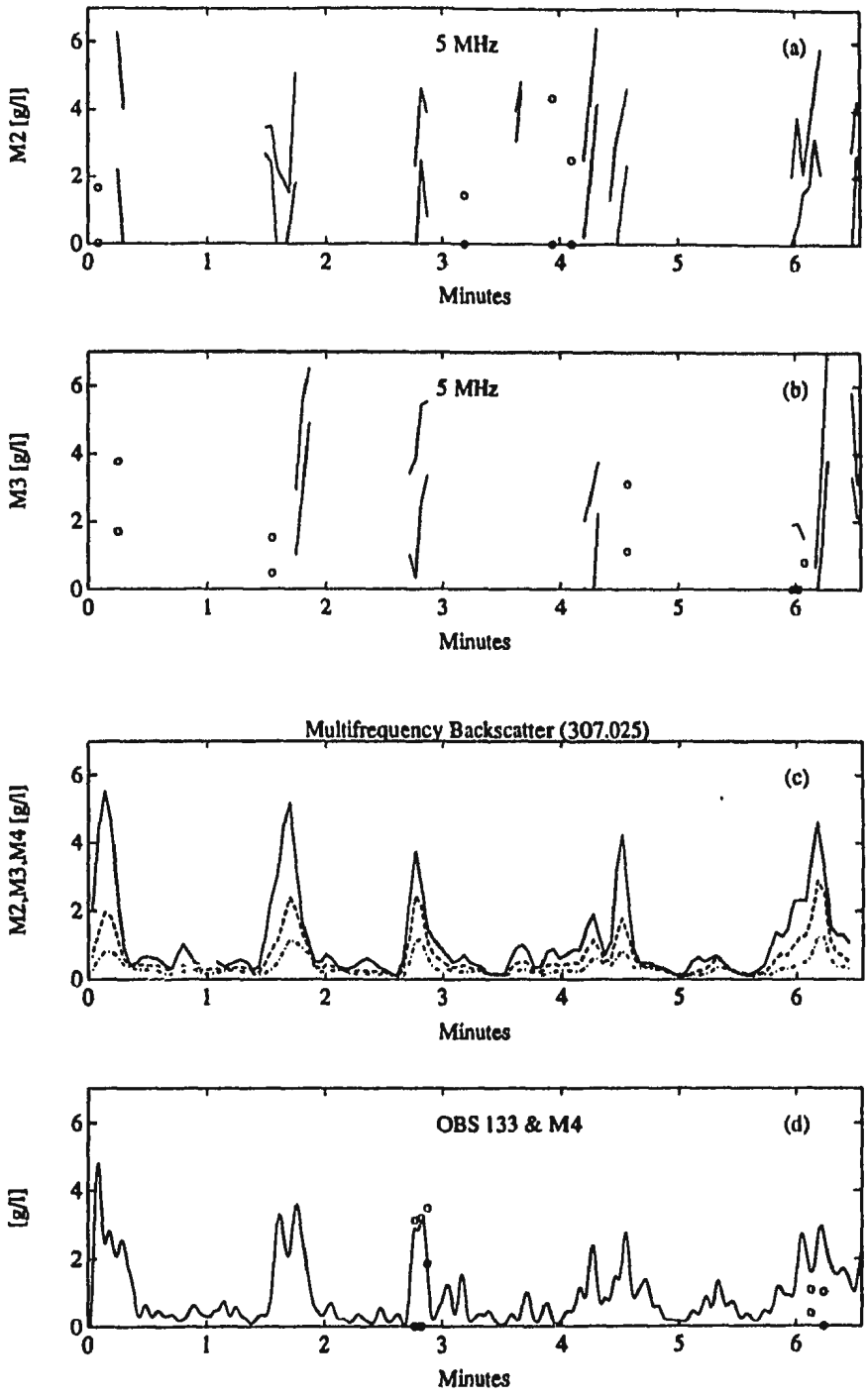

Figure 5.14: Reflection method sediment concentration at 5 MHz for run 307.025. Confidence limits (—) based on signal fluctuations are shown as functions of time. Illustrated are (a) reflection method $\overline{M}_2$, (b) reflection method $\overline{M}_3$, (c) multifrequency backscatter M_2, M_3, and M_4, and (d) OBS 133 (—) and $\overline{M}_4$ (o).

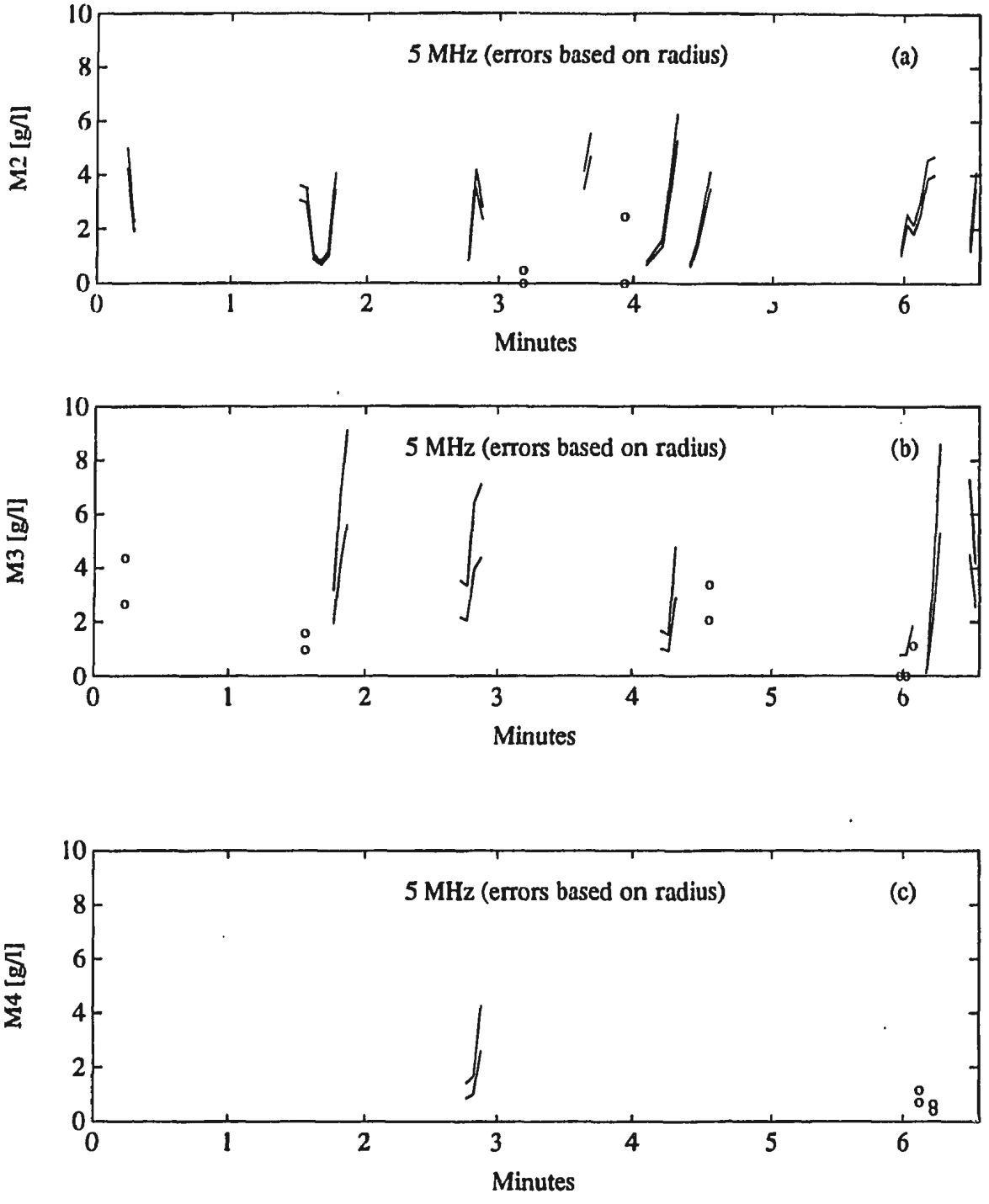

Figure 5.15: Run 307.025 time series of inverted concentration from single frequency reflection at 5 MHz, where the confidence limits (—) are based on the possible range of particle radii.

A summary of the linear regression analysis is presented in Table 5.3. Because the total duration of suspension events decreases further from the bottom, the number of sets available for the inversion decreases, therefore regressions involving $\overline{M}_4$ are not computed since only five data points exist for the comparison in this example.

Reflection Method	OBS 133	Multifrequency Backscatter				
		M_1	M_2	M_3	M_4	M_5
$\overline{M}_2$	0.65* † (0.37)	-0.45* (0.63)	-0.17 (0.83)	0.47* (0.90)	0.42* (4.6)	0.30 (8.2)
$\overline{M}_3$	0.27 (0.63)	-0.66 (0.67)	-0.51 (0.97)	0.69* † (0.32)	0.35* (2.7)	0.55 (5.3)

Table 5.3: Results at 5 MHz for run 307.025. Values for the linear regression coefficient, R_{zy}; values of D_{zy} are in parentheses. † denotes that the scatterplot is provided.

Figures 5.16(a) and 5.16(b) show scatterplots comparing reflection method estimates of OBS with $\overline{M}_2$, and M_3 with $\overline{M}_3$, respectively. Note that in each case points considered outliers (indicated by the '+' symbols) were excluded from the calculation. Points that were considered outliers in Figure 5.16(a) correspond to times when either method yielded concentrations less than 1 g/ℓ.

5.2.2 A case where the method fails

The failure of the reflection method to properly deduce $\overline{M}_2$ near 1.7 minutes into run 307.025 is now investigated. To keep the notation simple, only the proportionality of $\overline{M}_N$ to $\Delta\Gamma_N$ is required. From Equation 4.4,

$$\overline{M}_2 \propto \Delta\Gamma_2 \tag{5.2}$$

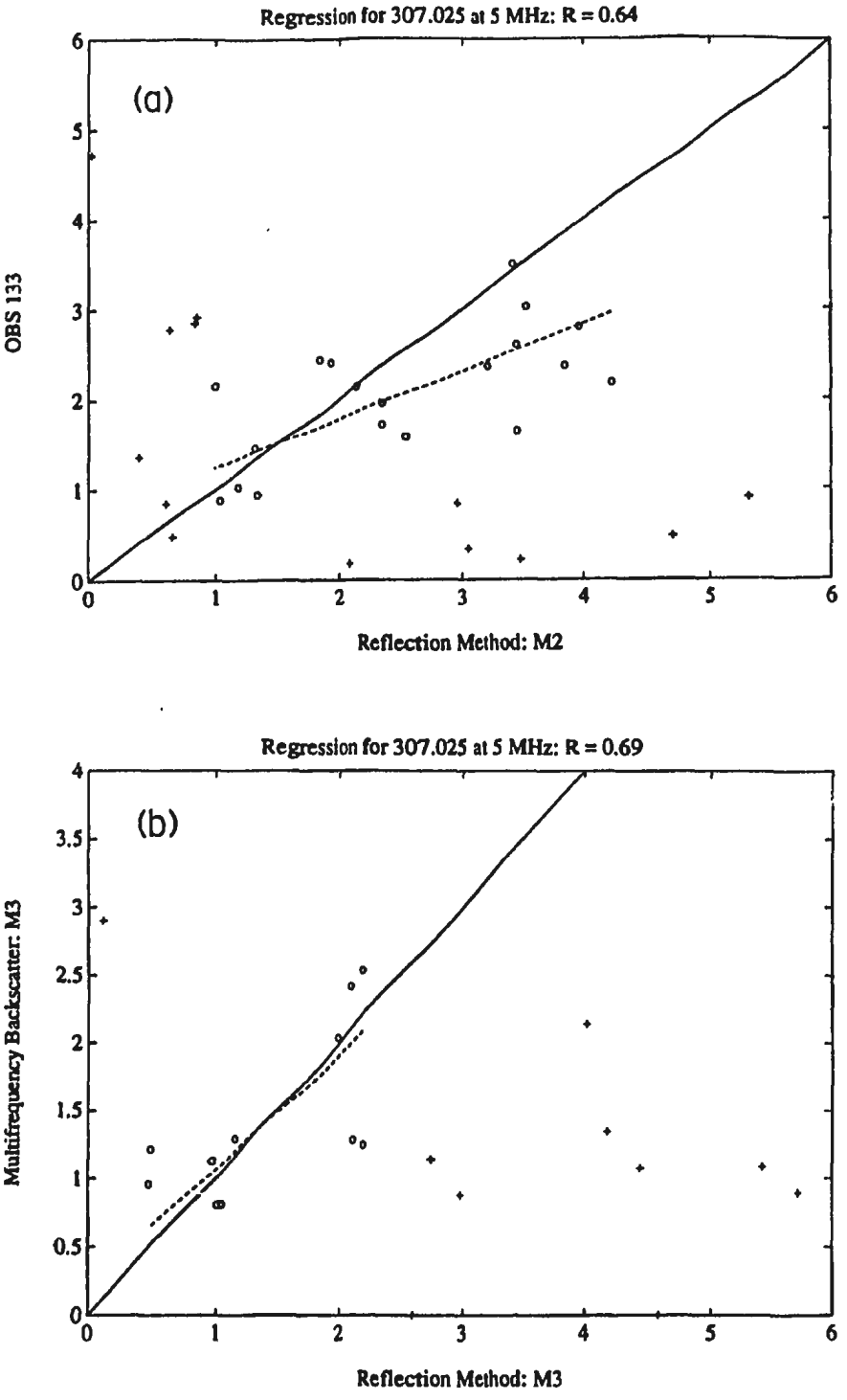

Figure 5.16: Scatterplots for run 307.025 at 5 MHz showing comparison of (a) OBS with $\overline{M}_2$, and (b) $\overline{M}_3$ with M_3 from the multifrequency backscatter method.

recalling that $\Delta\Gamma_2 \equiv \Gamma_1 - \Gamma_2$ and,

$$\Gamma_N \equiv \langle \ln \left(\frac{v'_N}{v_N} \right)^2 \rangle \tag{5.3}$$

and must be negative. Decreases in $\overline{M}_2$ occur when Γ_1 approaches Γ_2. In the case being examined it is reasonable to assume Γ_2 to be correct because it is isolated from the bottom echo. This implies that Γ_1 is decreasing (becoming more negative) when it shouldn't. This can be due to v_1 increasing, or v'_1 decreasing.

Figure 5.17(a) shows v'_1 and v_1, used to obtain Γ_1; Figure 5.17(b) shows v'_2 and v_2, used to obtain Γ_2. Shown in Figure 5.17(c) are Γ_1, Γ_2 and $\Delta\Gamma_2$. Only times where both Γ_1 and Γ_2 are less than zero produce a positive value of $\Delta\Gamma_2$. The reason for the low estimate of $\overline{M}_2$ for the times 1.6 to 1.7 minutes in Figure 5.17(d) corresponds to $\Delta\Gamma_2$ being nearly zero in Figure 5.17(c). As stated earlier, the position of the fluid-sediment interface lies in the upper portion of the bottom bin. It is therefore expected that part of the bottom echo has contributed to the bin reserved for v_1. This would explain the tendency for Γ_1 to be lower than it should be in this example, hence reducing the computed concentration for $\overline{M}_2$.

The decrease in $\overline{M}_3$ during the same times may be due to extra contributions to v'_3 from non-specular components of the reflection, which lie near the seabed where concentrations are higher. Note that based on geometry, contributions to mirror signals from non-specular components of reflection will become more apparent in the concentration estimates, the farther one goes above the seabed.

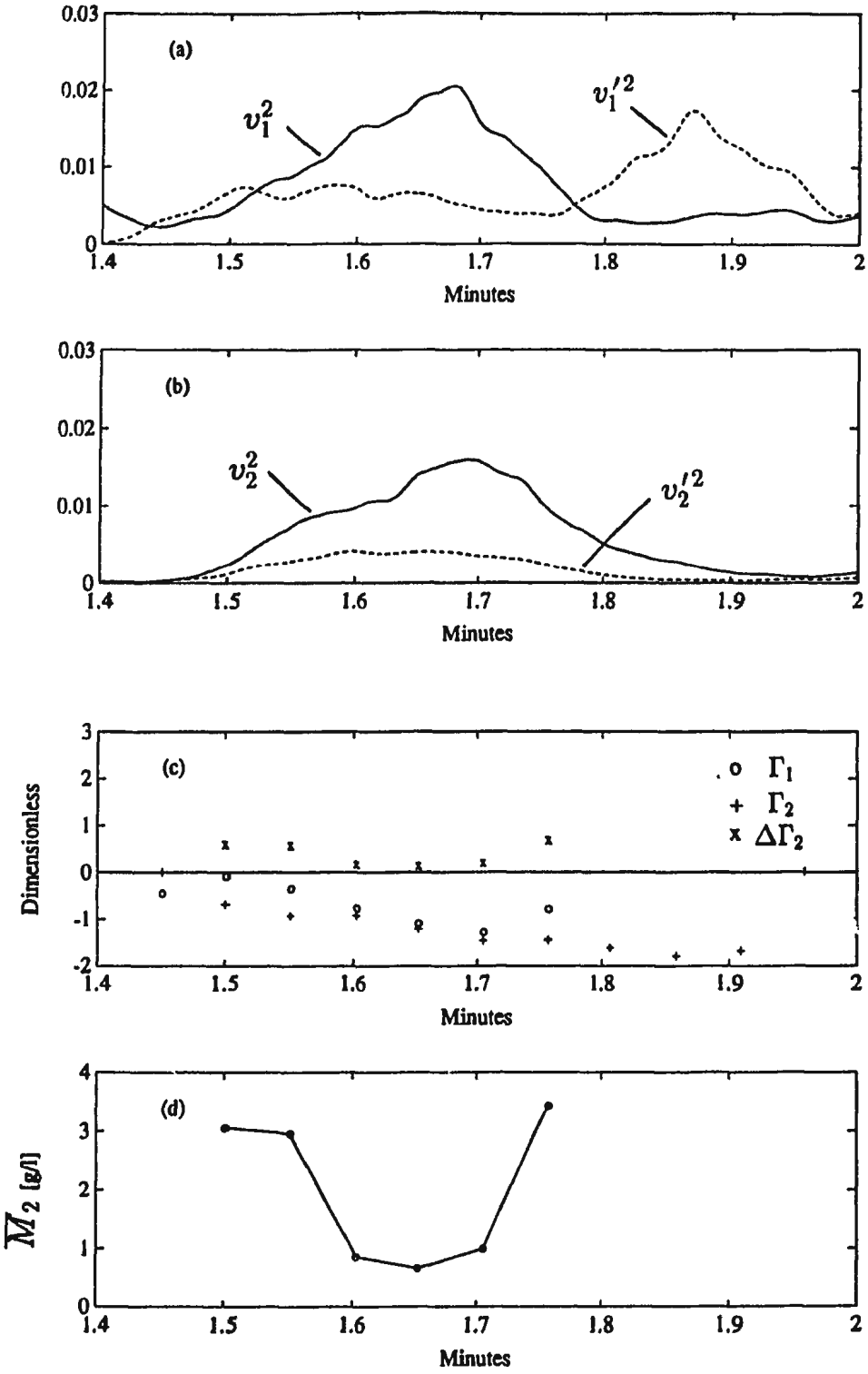

Figure 5.17: Failure of the reflection method during the second event for run 307.025. Illustrated are: (a) v_1^2 and $v_1'^2$, (b) v_2^2 and $v_2'^2$, (c) Γ_1 (o), Γ_2 (+), $\Delta\Gamma_2$ (x), and (d) $\overline{M}_2$.

Chapter 6

The Bottom Reflection Coefficient

This chapter discusses the treatment of the acoustic bottom reflection coefficient, R, and the effects of sand ripples on the acoustic measurements. In Section 6.1 the effects of sand ripples on the measurement geometry are discussed. In Section 6.3 an estimate of the possible range of values for R is calculated based on sediment properties for Stanhope Lane Beach. Finally, Section 6.4 presents estimated values of R based on acoustic data from Stanhope Lane.

In Chapter 3 it was shown that the reflection coefficient does not enter directly into the inversion scheme. However, the reflection coefficient and the degree to which the bottom relief plays a role in the reflection deserves discussion. There is a great volume of reference material on bottom interacting acoustics. Notable monographs on this subject include those by Hampton [1974, ed.], Kuperman and Jensen [1980], Pace [1983], and Akal and Berkson [1986]. The monograph by Beckmann and Spizzichino

[1987] covers most aspects of scattering from rough surfaces. Most recently, a book by Ogilvy [1991] reviews scattering from random rough surfaces. Standard acoustics texts such as Clay and Medwin [1977], and Tolstoy and Clay [1987], cover the general aspects of reflection and rough surface scattering.

6.1 Effects of Sand Ripples

The wavelength of the incident acoustic signal serves as a convenient measure by which to separate the small and large scale features of the bottom. For RASTRAN operating at 2.25 and 5 MHz, the wavelength in seawater is of order 0.7 mm and 0.3 mm, respectively, so characteristics with length scales much greater than 1 mm are considered large scale features for this discussion, and small scale otherwise. Figure 6.1 shows schematically a fluid-sediment interface including both small and large scale features. The large scale features at Stanhope Lane Beach are of interest here.

The bedforms at Stanhope Lane beach are of the vortex-ripple type [Sleath, 1984, p124]. For this type of bedform the generally accepted value of the mean ripple-height to ripple-spacing ratio, h_r/λ_r, lies between 0.1 and 0.25, implying mean surface slopes $< 15°$. The maximum steepness angle is of order 30°, and is related to the maximum angle of repose [Sleath, 1984, p118]. For the Stanhope site h_r and λ_r are, on average, roughly 3 and 12 cm respectively.

A narrow acoustic beam of halfwidth 2° placed 1 m above such a bedform will cover

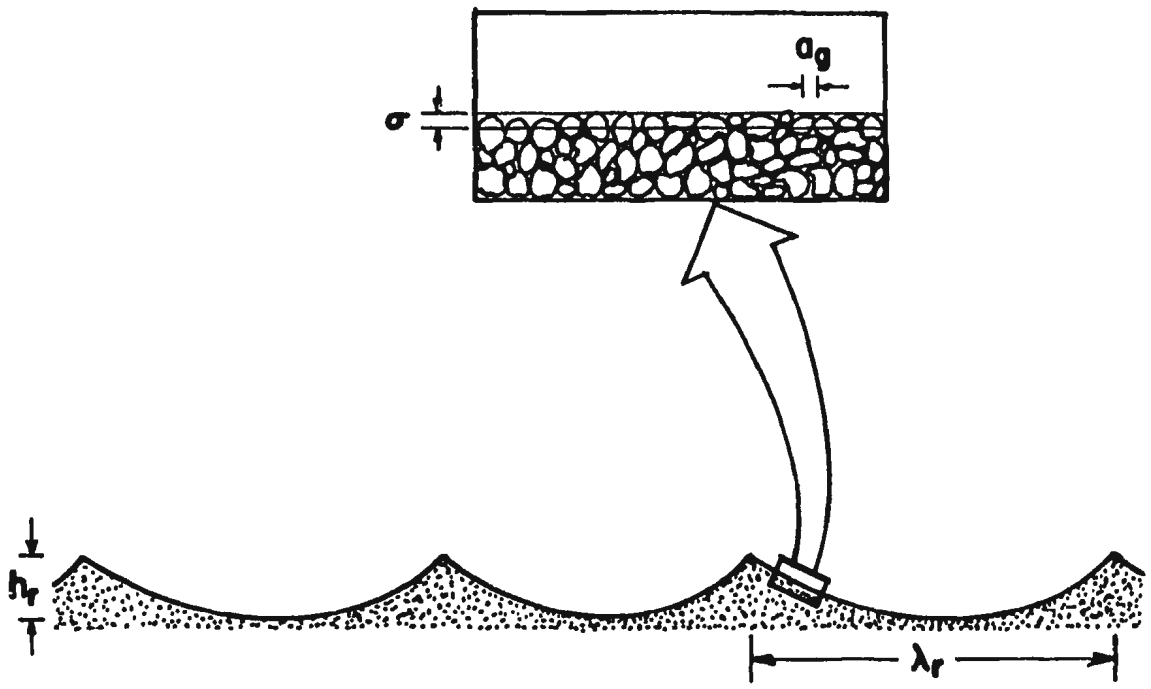

Figure 6.1: Beach fluid-sediment interface, showing both the large and small scale characteristics.

an area of roughly 7 cm in diameter, a length comparable to the ripple spacing. Thus on the large scale there will not appear to be any random, or irregular, variation in bottom topography across the width of the beam. Therefore the beam will be sensitive to whether it lies over a ripple crest or trough [Stanton, 1984]. To further complicate the matter, ripples migrate through the beam over time [Hay and Bowen, 1993]. The rates of migration appear to be rather slow (of order several cm/hr.), however, although this number is not well known. It is assumed here that the ripples are stationary during a 6.5 minute run.

For any point on a ripple, the surface slope has the effect of rotating the surface normal into a non-vertical orientation, and thus acoustic waves previously considered as normally incident now slightly graze the surface. The Rayleigh Criterion (Equation 2.23) shows that the reflected wave will be more specular when the incident wave approaches the surface at grazing angles.

Illustrated in Figure 6.2 are two possible geometries for bottom reflection when the ripple wavelength and the main lobe (denoted by dotted lines) dimensions near the bottom are of similar scale. For simplicity only the specular rays are considered, although as before non-specular components do exist. Figure 6.2(a) shows the case for a particle inside the main lobe. The wave scattered from this particle after the bottom reflection is able to contribute to the mirror signal in two ways: the usual re-reflection of the backscattered wave (solid lines), and the wave scattered by the particle in the direction of the transducer without re-reflection from the bottom (dashed

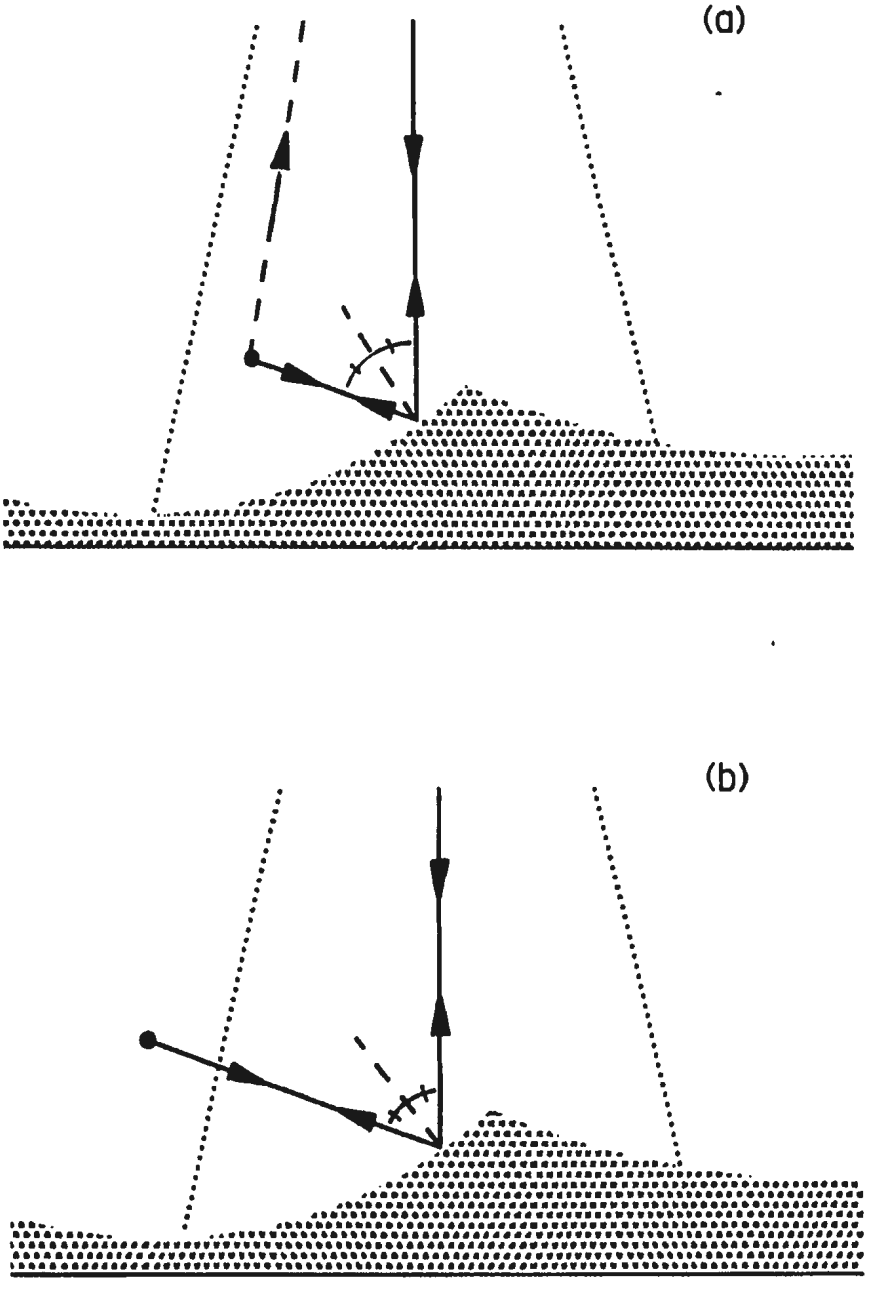

Figure 6.3: The effects of ripples on the measurement geometry. (a) Case of particle inside the beam's main lobe, and (b) case of particle outside the beam's main lobe.

line). The bottom reflected specular ray now propagates closer to the bottom, so concentration estimates for height z_0 above the bottom are contaminated by higher concentrations nearer the bottom. This may help explain the higher estimates of scattering attenuation, hence concentration, based on the reflection method compared to the multifrequency backscatter and OBS methods.

Figure 6.2(b) shows the case for a particle outside the main lobe. In this case the wave scattered by the particle can only contribute to the mirror signal via the incident path. Again, this particle lies closer to the bottom where the concentrations, hence scattering attenuation, are generally much higher. This too, then, may account for the high scattering attenuations computed for the 2.25 MHz case in Chapter 6.

6.2 Bottom Penetration

The penetration of sound past the fluid-sediment interface into the bottom is discussed. McCann and McCann [1985] have used a modified Biot theory [Biot, 1956] using a distribution of pore sizes, to predict compressional wave attenuation in non-cohesive sediments.

Grain sizes in the logarithmic phi-scale are expressed as, $\phi = -\log_2$(grain diameter in mm). For quartz beach sand of mean size $\phi = 2.5$, McCann and McCann obtain a predicted attenuation at 5 MHz of 1678 db/m. Using 1 neper = 8.686 db, the corresponding attenuation is 193 nepers/m. Hence the e-folding scale at 5 MHz, δ_5,

is of order 5 mm. The wavelength at 5 MHz in the sediment is of order 0.35 mm, which gives an attenuation e-folding scale of approximately 15 wavelengths below the fluid-sediment interface. A similar calculation for 2.25 MHz yields $\delta_{2.25} = 11.7$ mm, or 15 wavelengths below the fluid-sediment interface.

For Stanhope Lane the mean grain size is $\phi = 2.66$, so these results are believed to be of the same order, and therefore it is expected that sound which has penetrated the fluid-sediment interface will be effectively attenuated before re-emerging. This also means that bottom penetrating echoes cannot contribute to the mirror echo at distances more than 1 cm from below the seabed (i.e. only v_1' affected, if at all).

6.3 Estimated Value for R based on Sediment Properties

In this section an estimate of the plane wave reflection coefficient, R, is calculated on the basis of bulk sediment properties. These estimates ignore the irregular character of the surface on the small scale.

The plane wave reflection coefficient is written for normal incidence rays as [Clay and Medwin, 1977, p63],

$$R = \frac{\rho_s c_s - \rho_o c}{\rho_o c + \rho_s c_s} \tag{6.1}$$

where ρ_o and ρ_s are the mean bulk densities of seawater and sediment, respectively, c_s is the compressional soundspeed in the sediment, and c is the soundspeed in seawater.

Values of c and ρ_o are readily available, only reasonable values of ρ_s and c_s are required to estimate R.

Hamilton and Bachman [1982] have provided a set of regression equations interrelating sediment properties. Specifically, they provide equations to obtain porosity, bulk sediment density, and sound velocity from mean grain size, for three marine environments: shelf and slope, abyssal hill, and abyssal plain. Their values of compressional wave velocity were measured in the laboratory by a pulse technique, operating near 200 kHz. For Stanhope Beach, mean particle size in phi units is $\phi = 2.66$, and Hamilton's results yield a porosity, $\eta = (44 \pm 7)\%$. From the porosity the bulk sediment density and soundspeed are estimated to be 1.97 ± 0.11 g/cm^3 and 1747 ± 5 m/s respectively. Using typical field values for water temperature and salinity of 8°C and 29 ppt gives $c = 1477$ m/s. Equation 6.1 then yields an estimate of,

$$R_{Hamilton} \simeq 0.40. \tag{6.2}$$

An earlier paper by Faas [1969] relates sediment porosity directly to the reflection coefficient. The data used by Faas was obtained for the most part near 100 kHz. Assuming Hamilton's equations provide a reasonable estimate of the porosity, Faas' work indicates that we should expect,

$$R_{Faas} = 0.35 \pm 0.06 \tag{6.3}$$

in accord with Hamilton's result.

6.4 Estimated Value for R based on Acoustic Data

It is of interest to estimate the range of values for the reflection coefficient based solely on the acoustic data. One possible way to estimate such a range of values is to utilise Equation 3.8 of Chapter 3, namely,

$$\langle \ln \left(\frac{v'_N}{v_N} \right)^2 \rangle = \ln R^4 - 8 \int_0^{z_N} \langle \alpha_s \rangle \, dz'. \tag{6.4}$$

Considering the case for $N = 3$, and rewriting the integral as a sum, one finds,

$$\langle \ln \left(\frac{v'_3}{v_3} \right)^2 \rangle = 4 \ln R - 8\Delta z \left(\frac{1}{2}\overline{\langle \alpha_s \rangle}_1 + \overline{\langle \alpha_s \rangle}_2 + \overline{\langle \alpha_s \rangle}_3 \right), \tag{6.5}$$

Solving Equation 6.5 for the reflection coefficient, R,

$$R = \exp \left\{ \frac{1}{4}\Gamma_3 + 2\Delta z \left(\frac{1}{2}\overline{\langle \alpha_s \rangle}_1 + \overline{\langle \alpha_s \rangle}_2 + \overline{\langle \alpha_s \rangle}_3 \right) \right\} \tag{6.6}$$

where the definition for Γ_N from Equation 3.10 has been used. To obtain absolute minimum estimates of R from the data, the attenuation terms in Equation 6.6 are set to zero, and thus for any N,

$$R_{minN} = e^{\Gamma_N/4}. \tag{6.7}$$

For the first suspension event of run 300.030 Figure 6.3(a) shows time series of R_{min2}, R_{min3}, and R_{min4} at 2.25 MHz, and Figure 6.3(b) shows time series of R_{min2} and R_{min3} at 5 MHz. The noticeable feature of these results is that these minimum values fall in the range 0.4 to 0.7, generally higher than the estimated values based on bulk sediment properties of 0.35 and 0.4, but nonetheless of the right order. (Note that

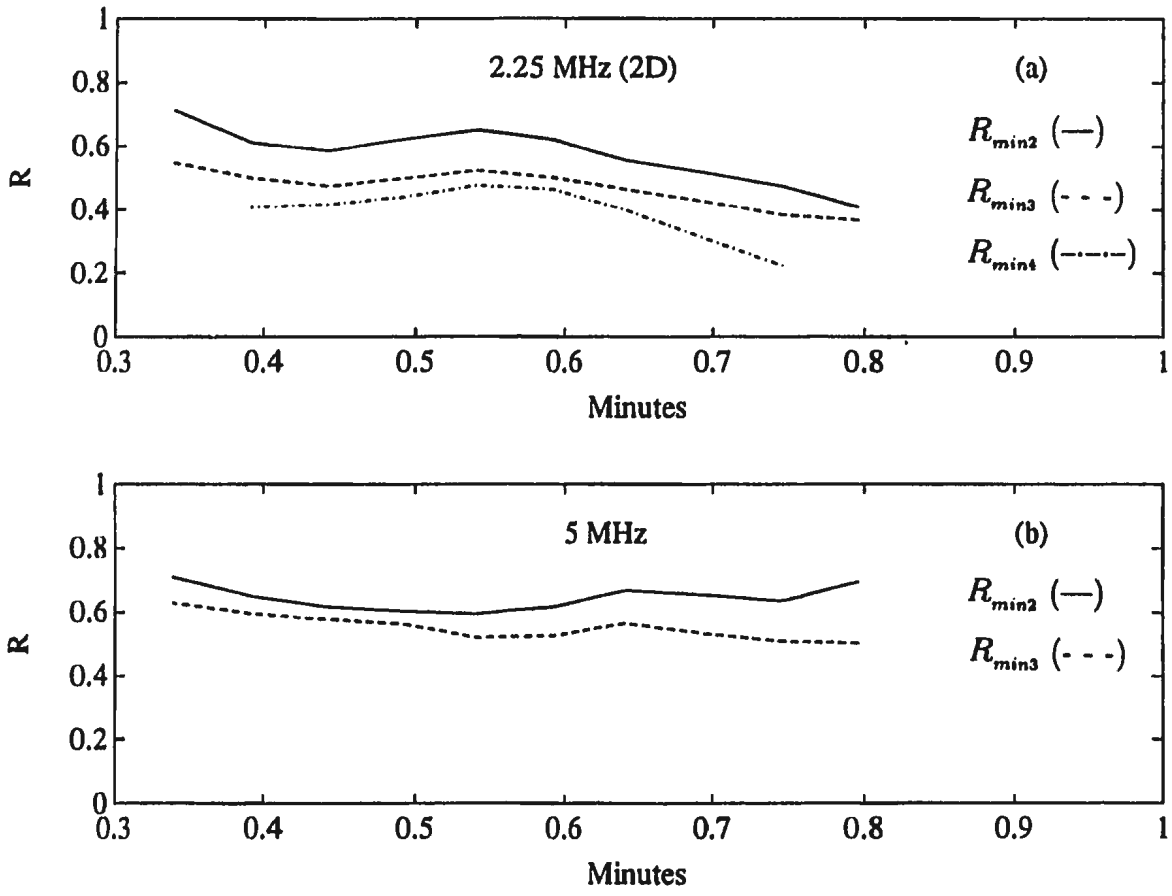

Figure 6.4: Time series of the reflection coefficient minimum values for run 300.030 based on acoustic data. (a) R_{min2} (—), R_{min3} (- - -), and R_{min4} (-·-·-) at 2.25 MHz; (b) R_{min2} (—), and R_{min3} (- - -) at 5 MHz.

Pace *et al.* estimated reflection coefficients of 0.63 and 0.57 for their cobble surface based on the measured coherent intensity and the first term of Equation 2.26, and by extrapolating data from Hamilton [1970] based on particle size, respectively).

Using the definition of Γ_N, and ignoring the time average, Equation 6.7 may be expressed in terms of the recorded voltages as,

$$R_{minN} = e^{1/2} \left(\frac{v'_N}{v_N} \right). \tag{6.8}$$

Assuming that $N > 1$ so neither voltage is contaminated by the bottom echo, then high values of R_{minN} are likely due to values of v'_N larger than expected using purely specular reflection arguments. If the non-specular component of the surface reflection is allowed to contribute to the mirror signals, then this may explain higher estimates of R_{minN}.

Chapter 7

Conclusions

The goal of this research was to explain observations in field data of mirroring of the acoustic backscatter signal from suspended sediment. Assuming that the mechanism for generating the mirror signal was the result of a specularly reflected bottom echo scattering from suspended sediment, and subsequently re-reflecting off the bottom, an inversion algorithm to obtain suspended sediment concentration was devised to quantify the validity of the approach. The approach is considered valid if concentrations obtained using this method are in accord with concentrations obtained via multifrequency acoustic backscatter and optical backscatter techniques.

Concentrations obtained using the reflection method at 5 MHz are generally higher than those obtained with a multifrequency inversion and *in-situ* OBS measurements, but are within accepted limits. Linear regression analysis shows moderate correlation of the reflection method with the other techniques, but also indicates that the method

may have difficulty detecting lower concentrations. It has been shown at 5 MHz that the uncertainty in concentration is primarily due to variations in signal, rather than errors in particle size. Uncertainties due to the amount of background signal subtracted are less than 20%.

Inverted concentrations obtained with the reflection method at 2.25 MHz less than the upper limit of the theory (30 g/ℓ), are found mostly during the peak of a suspension event. Near the start and end of suspension events, where the reflection method becomes less likely to perform well, concentrations are generally much higher than the theory physically permits. Because the assumption of specular, coherent bottom reflection should be better at 2.25 MHz than at 5 MHz, these results suggest a problem with the method. One possibility is that the beam is sensing the bottom topography (ripples), which are not accounted for in the theory (See discussion of Figure 6.1). It is also possible that the incoherent contribution to the reflected wave needs to be included (see discussion in Section 2.3).

Results at 2.25 MHz indicate that the High-pass model for scattering attenuation is sensitive at this frequency to the range of particle sizes at Stanhope Beach, much more so than at 5 MHz. This accounts for a large part of the discrepancy at 2.25 MHz when comparing with other methods. The accuracy of the High-pass model itself has been questioned, especially near $x \simeq 1$. A more accurate model of the scattering attenuation may improve the results for the 2.25 MHz case.

Estimates of the relative contributions to the reflected field (Chapter 2) and anal-

ysis of the data have shown that assuming the bottom reflection to be mostly specular is significant, and probably incorrect. It is suggested that measurements be carried out in future on surfaces at close range for which $g \sim 1$ and $T \sim \overline{a}$ are common properties of the experimental arrangement to quantify the assumption that has been made and to aid in further development of the theory. It is also suggested that experiments be carried out in a controlled environment, such as in wave flumes. Regardless, it seems likely that to first order at least, the mirror image is produced by the bottom reflected wave scattering from suspended sediment near the seabed and subsequently re-reflecting from the seabed — in effect the seabed acting as an acoustic mirror.

References

Abramowitz, M., and Irene A. Stegun (Eds.), *Handbook of Mathematical Functions*, Dover, New York, 1046 pp., 1965.

Akal, Tuncay, and Jonathan M. Berkson (Eds.), *Ocean-Seismo Acoustics, Low-Frequency Underwater Acoustics*, Nato Conference Series IV, Marine Sciences, Vol 16, Plenum Press, New York, 1986.

Beckmann, P., and A. Spizzichino, *Scattering of Electromagnetic Waves from Rough Surfaces*, Artech House, Inc., Norwood, MA, USA, 1987.

Biot, M. A., Theory of propagation of elastic waves in a fluid- saturated porous solid. I. Low frequency range, *J. Acoust. Soc. Am.*, **28** 168–178, 1956.

Biot, M. A., Theory of propagation of elastic waves in a fluid- saturated porous solid. II. Higher frequency range, *J. Acoust. Soc. Am.*, **28** 179–191, 1956.

Chow, V. T., The log-probability law and its engineering applications. *Am. Soc. Civil Engineering Proc., Separate no. 536*, 25, 1954.

Chýlek, Petr, G. W. Grams and R. G. Pinnick, Light Scattering by Irregular Randomly Oriented Particles, *Science*, Vol. 193, 480–482, August 1976.

Clarke, S. P., *Handbook of Physical Constants*, Geol. Soc. Am. Mem., 97, revised ed., 197–201, 1966.

Clay, C. S. and H. Medwin, *Acoustical Oceanography*, John Wiley, New York, 1977.

Crawford, A. M., and A. E. Hay, Determining suspended sand size and concentration from multifrequency acoustic backscatter, submitted to *J. Acoust. Soc. Am.*, May 1993.

Downing, J. P., R. W. Sternberg, and C. R. B. Lister, New Instrumentation for the investigation of sediment suspension processes in the shallow marine environment, *Mar. Geol.*, **42**, 19–34, 1981.

Einstein, H. A., The bed-load function for sediment transportation in open channel flows. *U.S. Dept. Agr., Soil Conserv. Serv., Tech. Bull. 1026*, 78 pp., 1950.

Faas, Richard W., Analysis of the relationship between acoustic reflectivity and sediment porosity, *Geophysics* Vol. 34, No. 4, 546–553, 1969.

Fisher, F. H., and V. P. Simmons, Sound absorption in sea water, *J. Acoust. Soc. Am.*, **62** 558–564, 1977.

Flammer, G. H., Ultrasonic Measurement of Suspended Sediment, *United States Geological Survey Bulletin*, No. 1141–A (US GPO, Washington, DC), 1962.

Hamilton, E. L., Sound velocity and related properties of Marine sediments, North Pacific, *J. Geophys. Res.*, **75**, 4423–4446, 1970.

Hamilton, E. L., and R. T. Bachman, Sound velocity and related properties of marine sediments, *J. Acoust. Soc. Am.*, **72** (6), 1891–1904, 1982.

Hampton, L. D. (Ed.), *Physics of Sound in Marine Sediments*, Plenum Press, New York, 1974.

Hanes, D. M., and D. A. Huntley, Continuous measurements of suspended sand concentration in a wave dominated nearshore environment. *Continental Shelf Research*, **6**, 585–596, 1986.

Hanes, D. M., C. E. Vincent, D. A. Huntley, and T. M. Clarke, Acoustic measurements of suspended sand concentration in the C^2S^2 Experiment at Stanhope Lane, Prince Edward Island, *Mar. Geol.*, **81**, 185–196, 1988.

Hatch, T. and S. P. Coate, Statistical description of size properties of non-uniform particulate substances. *Franklin Inst. Jour.*, *207*, 369–387, 1929.

Hay, A. E., L. Huang, E. B. Colbourne, J. Sheng and A. J. Bowen, A High Speed Multi-Channel Data Acquisition System for Remote Acoustic Sediment Transport Studies, in *Oceans '88 Proceedings*, IEEE, Baltimore, Vol. 2, 413–418, 1988.

Hay, A. E. and A. J. Bowen, Acoustic Measurements of Spatially-Correlated Depth Changes in the Nearshore Zone During Autumn Storms, *J. Geophys. Res.*, in press, 1993.

Hay, A. E., Sound scattering from a particle-laden, turbulent jet, *J. Acoust. Soc. Am.*, **90** (4), Pt. 1, 2055–2074, 1991

Hay, A. E. and J. Sheng, Vertical Profiles of suspended sand concentration and size from multifrequency acoustic backscatter, *J. Geophys. Res.*, **97** No. C10, 15,661–15,677, 1992.

Hazen, D. G., D. A. Huntley, and A. J. Bowen, UDATS: A system for measuring nearshore processes. In *Proc. Oceans '87*, 993–997, 1987.

Jansen, R. H., The *in-situ* measurement of sediment transport by means of ultrasound scattering, Report 203, Delft Hydraulic Laboratory, Delft, The Netherlands, 1978.

Jansen, R. H., An ultrasonic doppler scatterometer for measuring suspended sand transport, in *Ultrasonic International 79, Conference Preceedings*, edited by Z. Novak (Graz, Austria, 1979), UI 79, pp. 366-369.

Johnson, R. K., Sound scattering from a fluid sphere revisited, *J. Acoust. Soc. Am.*, **61** 375–377, 1977.

Kuperman, W., and Finn B. Jensen (Eds.), *Bottom Interacting Ocean Acoustics*, Plenum Press, New York, 1980.

Libicki C., K. W. Bedford, and J. F. Lynch, The interpretation and evaluation of a 3 MHz acoustic backscatter device for measuring benthic boundary layer sediment dynamics, *J. Acoust. Soc. Am.*, **85**, 1501–1511, 1989.

Lynch, James F., Thomas F. Gross, Blair H. Brumley and Richard A. Filyo, Sediment concentration profiling in HEBBLE using a 1-MHz acoustic backscatter system, *Mar. Geol.*, **99** 361–385, 1991.

McCann, C., and D. M. McCann, A theory of compressional wave attenuation in noncohesive sediments, *Geophysics* Vol. 50, No. 8, 1311–1317, 1985.

Morse, P. M. and K. U. Ingard, *Theoretical Acoustics*, Princeton University Press, McGraw-Hill, Inc., 1968.

Morse, P. M., *Thermal Physics*, Second Edition, W. A. Benjamin Inc., New York, 1969.

Neubauer, W. G., R. H. Vogt, and L. R. Dragonette, Acoustic reflection from elastic spheres. I. Steady-state signals, *J. Acoust. Soc. Am.*, **55** 1123–1129, 1974.

Ogilvy, J. A., *Theory of Wave Scattering from Random Rough Surfaces*, Adam Hilger, New York, 1991.

Orr, M. H., and F. R. Hess, Remote acoustic monitoring of natural suspensate distributions, active suspensate resuspension, and slope/shelf water intrusions, *J. Geophys. Res.*, **83**(C8), 4062–4068, 1978.

Orr, M. H., and W. D. Grant, Acoustic sensing of particles suspended by wave-bottom interactions, *Mar. Geol.*, **45**, 253–260, 1982.

Pace, Nicholas G. (Ed.), *Acoustics and the Sea-Bed*, Bath University Press, Bath, UK, 1983.

Pace, Nicholas G., Zyad K. S. Al-Hamdani, and Peter D. Thorne, The range dependence of normal incidence acoustic backscatter from a rough surface, *J. Acoust. Soc. Am.*, **77** 101–112, 1985.

Rayleigh, Lord, *The Theory of Sound* (New York: Dover) (first edition 1877, New York: Macmillan), 1945.

Schaafsma, A. S. and W. J. G. J. der Kinderen, Ultrasonic instruments for the continuous measurement of suspended sand transport, in *Proceedings of the IAHR Symposium on Measuring Techniques in Hydraulic Research*, edited by A. C. E. Wessels (Balkema, Rotterdam, Delft, The Netherlands, 1986).

Sheng, J. and A. E. Hay, An Examination of the Spherical Scatterer Approximation in Aqueous Suspensions of Sand, *J. Acoust. Soc. Am.*, **83**(2), 598–610, 1988.

Sheng, J., *Remote Determination of Suspended Sediment Size and Concentration by Multi-frequency Acoustic Backscatter*, Ph.D. thesis (Dept. of Physics, Memorial University of Nfld.), 1991.

Shung, KoPing K., Rubens A. Sigelmann, and John M. Reid, Scattering of ultrasound by blood, *IEEE Transactions on Biomedical Engineering*, Vol. BME-23, No. 6, November 1976.

Sigelmann, Rubens A., and John M. Reid, Analysis and measurement of ultrasound backscattering from an ensemble of scatterers excited by sine-wave bursts, *J. Acoust. Soc. Am.*, **53**(5), 1973.

Sleath, J. F. A., *Sea Bed Mechanics*, John Wiley and Sons, New York, 335 pp., 1984.

Stanton, T. K., Sonar estimates of seafloor microroughness, *J. Acoust. Soc. Am.*, **75** (3), 809–818, 1984.

Thorne, P. D., and N. G. Pace, Acoustic studies of broadband scattering from a model rough surface, *J. Acoust. Soc. Am.*, **75** (1), 133–144, 1984.

Thorne, P. D., C. E. Vincent, P. J. Hardcastle, S. Rehman, and N. Pearson, Measuring suspended sediment concentrations using acoustic backscatter devices, *Mar. Geol.*, **98**, 7–16, 1990.

Thorne, P. D., C. E. Vincent, P. J. Hardcastle, S. Rehman, and N. Pearson, Measuring suspended sediment concentrations using acoustic backscatter devices, *Mar. Geol.*, **98**, 7–16, 1991.

Tolstoy, I., and C. S. Clay, *Ocean Acoustics, Theory and Experiment in Underwater Sound*, American Institute of Physics, Inc., New York, 1987.

Urick, R. J., The absorption of sound in suspensions of irregular particles, *J. Acoust. Soc. Am.*, **20**, 283–289, 1948.

van Hardenberg, B., A. E. Hay, J. Sheng, and A. J. Bowen, Field measurements of the vertical structure of suspended sediment, in *Coastal Sediments '91*, proceedings of a Speciality Conference on Quantitative Approaches to Coastal Sediment Processes, Seattle, Washington, June 25–27, 1991. American Society of Civil Engineers, New York, N. Y., 1991

Varadan, V. K., V. N. Bringi, V. V. Varadan, and Y. Ma, Coherent attenuation of acoustic waves by pair-correlated random distributions of scatters with uniform and Gaussian size distributions, *J. Acoust. Soc. Am.*, **73**, 1941–1947, 1983.

Vincent, C. E., R. A. Young, and D. J. P. Swift, On the relationship between bedload and suspended load transport on the inner shelf, Long Island, New York, *J. Geophys. Res.*, **87**, 4163–4170, 1982.

Vincent, C. E., and M. O. Green, Field measurements of the suspended sand concentration profiles and fluxes, and of the resuspension coefficient γ_0 over a rippled bed. *J. Geophys. Res.*, **95**, 11591-11601, 1990.

Vincent, C. E., D. M. Hanes, and A. J. Bowen, Acoustic measurements of suspended sand on the shoreface and the control of concentration by bed roughness, *Mar. Geol.*, **96**, 1-18, 1991.

Young, Robert A., Merrill, John T., Clarke, Thomas L., and John R. Proni, Acoustic profiling of of suspended sediments in the marine bottom boundary layer, *Geophysical Research Letters*, Vol. 9, No. 3, 175-178, 1982.